学位論文

Kinematics of dense cores and surrounding materials in Taurus and Lupus star-forming regions

（おうし座とおおかみ座星形成領域における高密度コアの運動）

平成２７年１２月博士（理学）申請

東京大学大学院理学系研究科

天文学専攻

清兼 和紘

Abstract

In early phase of star formation, angular momentum distribution of a natal core is crucial to determine the evolution of the core. Since there is a large gap of the specific angular momentum between a dense core and a star/disk system, the excessive angular momentum must be converted to orbital angular momentum of a binary or must be removed by a jet/outflow. Rotation yields a velocity gradient, and then one method searching for rotation is a least square fitting of the velocity gradient assuming a rigid rotation, called to a velocity gradient fitting, and it is known that the specific angular momenta of dense cores, $j(= J/M)$, have a relation of $\propto R^{1.6}$ $\mathrm{km\,s^{-1}\,pc}$ where R is core size. Recently, high sensitivity mappings of nearby molecular clouds in far-infrared and submillimeter bands with Hershel and AzTEC/ASTE show ubiquitous existence of the filamentary structures with 0.1-pc uniform width. It is important to investigate dense core formation from large scale structure via fragmentation.

I present an observational study of dense cores in Taurus and Lupus Molecular Clouds using the NRO 45 m and the Mopra 22 m telescopes with the ^{13}CO(J=1–0), C^{18}O(J=1–0), $\mathrm{N_2H^+}$(J=1–0), and $\mathrm{HC_3N}$(J=10–9) emission lines. These lines have different critical densities of 10^3 to 10^5 $\mathrm{cm^{-3}}$, and then these lines can probe kinematics of the molecular gas with different densities.

There are four $\mathrm{N_2H^+}$ dense cores in Taurus and six $\mathrm{N_2H^+}$ dense cores in Lupus whose sizes, masses, and velocity widths are in the range of 0.02 - 0.05 pc, 0.27 - 0.44 km s^{-1}, and 0.9 - 1.9 $\mathrm{M_\odot}$, respectively. Each $\mathrm{N_2H^+}$ core mass is comparable to the virial mass and thus these cores are physical, not transient objects. The dense cores exhibit a velocity gradient. From the fitting, the velocity gradients were derived to be 0.9 - 4.7 $\mathrm{km\,s^{-1}\,pc^{-1}}$, which have the centrifugal radii of a few au to a few handred corresponding to a known size of protoplanetary disks. Since a outflow axis of protostellar sources in most cases is perpendicular to the velocity gradient, the gradient presumably represents the rotation motion of the dense cores. The rotational axis determined by the velocity gradient of each dense core is randomly directed compared with locally elongated direction of the filaments. It is suggested that the rotational axis of the dense cores in Lupus will be determined by local physical conditions such as turbulence.

I found that different density tracers show different velocity gradients at least in a case of Lup1 C3 and C4. The relatively lower density tracer of C^{18}O shows the large-scale motion in the filament and the higher density tracer of $\mathrm{HC_3N}$ or $\mathrm{N_2H^+}$ shows the rotational motion in the cores. The ratios of the non-thermal velocity dispersion σ_{nth} to the sound velocity c_{s} were obtained as $\sigma_{\mathrm{nth}}/c_{\mathrm{s}} \sim$ 1-2 in

$C^{18}O$ and $\sigma_{\rm nth}/c_{\rm s} \sim 0.7$ in N_2H^+, suggesting that $C^{18}O$ traces supersonic turbulent motions around the dense cores while N_2H^+ and HC_3N trace subsonic turbulent motions within dense cores. As one of kinematics in a filament in present studies, it is suggested to experience a fragment motion along the filaments, which will cause oscillation of densities and centroid velocities with a λ/4 phase shift. No such feature is identified in my samples and fragment motion along filament elongation is not seen universally in low-mass star forming regions. Then, I suggest that there are bimodal evolutional paths with various degree of turbulence. One is that there is an intermediate stage as velocity coherent filaments of multi-fibers from a supersonic turbulent filament to dense cores. The other is that a supersonic turbulent filament would form directly coherent dense cores.

In addition to the velocity gradient fitting, I invented a method to derive the two dimensional specific angular momentum distributions, which can provide the angular momentum and the direction as a function of radius. Interestingly, the directions of the specific angular momentum in L1527 are changing from inner core ($0.01\,{\rm pc} < {\rm r} < 0.02\,{\rm pc}$, ${\rm P.A.} = +90^\circ$) to outer core ($0.02\,{\rm pc} < {\rm r} < 0.07\,{\rm pc}$, ${\rm P.A.} = -150^\circ$), while the direction in B335 is almost constant within the core. The rotation axis in the inner core is roughly perpendicular to the outflow axis in both cases. I suggest that the rotational axis of L1527 change at $r \sim 0.02$ pc, which may explain a deflected molecular outflow observed in several cases.

I searched for dense cores with high resolution of molecular line observations covering 0.01 to 0.1 pc , leading to the following star formation scenario. Filaments are one of the evolutional stages from molecular clouds to to stars through dense cores. In filaments, the surrounding gas traced by $C^{18}O$(J=1–0) has the supersonic velocity dispersion in a case, and the dense cores traced by N_2H^+(J=1–0) or HC_3N(J=10–9) are located on a state of velocity-coherent within the supersonic turbulent surrounding gas, suggesting that the turbulence will decay during the formation of dense cores. The rotational axes of the dense cores determined by the velocity gradients are not correlated with the directions of filament elongation. Within a core, the rotational axis could change under some situations, but the rotational axis will connect to the inner disk and the outflow direction. Comprehensively, those will be related to evolutions from molecular clouds to stars via filaments and dense cores.

Contents

List of Figures

List of Tables

Chapter 1

Introduction

1.1 Low-mass Star Formation

In general, stars are formed in dense cores in molecular clouds through gravitational collapse, and then circumstellar materials fall into a central star (Shu et al., 1987). Figure 1.1 show a schematic view of the evolution process of low-mass star forming objects. A molecular cloud sometimes fragments to dense cores or it goes through a filamentary structure in the fragmentation process to dense cores (Larson, 1985). The dense core gravitationally collapses and a protostar is born. The protostar is associated with a molecular outflow and a protoplanetary disk, the latter of which is the planet forming site.

For young stellar objects (YSOs) prior to the main sequence stars, the evolutional stages are classified by the index of the spectral energy distribution,

$$a = \frac{\mathrm{d}\log(\lambda F_\lambda)}{\mathrm{d}\log(\lambda)} \tag{1.1}$$

where λ is the wavelength and F_λ is the flux density at the wavelength λ. The evolutional stages are determined from the index a at between 1 and 20 μm (Lada, 1987), and are classified to "Class I", "Class II", and "Class III". Class I objects have an index of $a \geq 0$ with its thick envelope accreting on to the disk/star system. Class II objects have an index of $-2 < a < 0$, with the circumstellar disk still accreting to the star. Class III objects have an index of $a \leq -2$, which is nearly identical to the blackbody with little infrared excess emission, and these objects have almost dissipated most of the circumstellar disk. Andre et al. (1993) have introduced an additional class of "Class 0". The Class

0 objects have much stronger submillimeter emission than the Class I objects, meaning the youngest stellar objects of all.

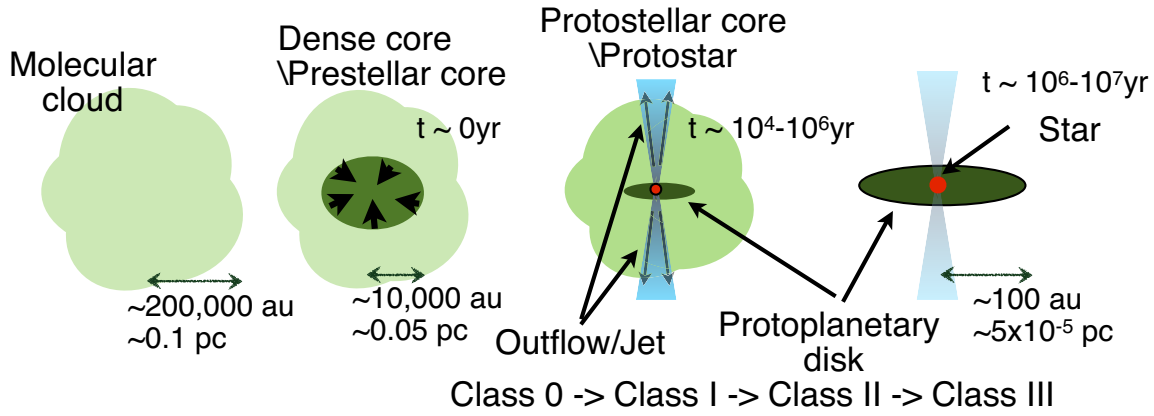

Figure 1.1: Schematic view of the evolution process of low-mass young stellar objects.

1.1.1 Angular momentum during star formation

In star formation at the early phase, angular momentum distribution of a natal core is crucial to determine the evolution of the core. Since there is a large gap of the specific angular momentum between a dense core and a star/disk system, the excessive angular momentum must be converted to orbital angular momentum of a binary or must be removed by a jet/outflow. Protostellar cores are important to study the angular momentum distribution because such cores still preserve the initial condition in the outer part on a scale of 0.1 pc.

Several studies of the angular momentum in dense cores have been conducted so far. A pioneer work by Goodman et al. (1993) showed that the specific angular momentum of dense cores, $j\,(=J/M)$, has a relation of $\propto R^{1.6}\,\mathrm{km\,s^{-1}\,pc}$ from their NH_3 survey, where R is the diameter of the core. Caselli et al. (2002a) also performed a dense core survey in N_2H^+, and found that the typical velocity gradient of a dense core is $2\,\mathrm{km\,s^{-1}\,pc^{-1}}$. Since those studies are based on a least squares fitting of a velocity gradient assuming a rigid-rotation, the radial distribution of the specific angular momentum cannot be derived. Rotational structures have been also studied using a Position-Velocity diagram cut perpendicular to the outflow direction. For example, Belloche et al. (2002) have demonstrated a differential rotation within a N_2H^+ core from their high angular resolution observations. This feature indicates an infalling envelope and spinning-up rotational velocities toward the core center. The

angular momentum in the more inner part has been investigated using interferometric observations (Ohashi et al., 1997b,a; Yen et al., 2013; Kurono et al., 2013) but the analysis method is the same as above and assuming a single rotational axis in the core.

The past studies tried to reveal the distribution of specific angular momentum with different scales (see Figure 8 in Belloche, 2013, and its references). On a large scale of $> 0.03\,\mathrm{pc}$, the regime has a correlation between the specific angular momentum of a dense core and the radius, as $j \propto R^{1.6}$. This indicates the loss of angular momentum due to magnetic braking, gravitational torque, or tracing interstellar turbulence. On a middle scale between a few hundred au and 0.03 pc, the specific angular momentum is roughly constant, which indicates dynamically collapsing with preserving angular momentum. In the most inner part less than a few hundred au, there frequently appears a disk where the structure is rotationally supported. All these analyses assume a single rotational axis regardless of the scale. Tobin et al. (2011), however, compared the velocity gradients of dense cores on the small scale with interferometric data and those on the large scale with single dish data. They found that the directions of velocity gradients on different scales mostly agree within 45° while the different directions are seen in a few sources.

1.1.2 Motions in a filament

Recently, high sensitivity mapping observations of nearby molecular clouds in far-infrared and submillimeter bands with Hershel and AzTEC/ASTE show ubiquitous existence of the filamentary structures with 0.1-pc uniform width in low-mass star forming regions (André et al., 2010). Since a dense core in a filament is a site of star formation, it is important to investigate dense core formation from large scale structures via fragmentation. Kinematics in a filament are investigated from molecular line observations. Hacar & Tafalla (2011) suggested that a supersonic turbulent filament consists of many subsonic filaments, called as multi-fiber. They proposed that the subsonic filaments are "velocity coherent filaments" by analogy of velocity coherent cores found by Barranco & Goodman (1998) and Goodman et al. (1998). Hacar & Tafalla (2011) indicated that there are intermediate structures as velocity coherent filaments in the a formation of dense cores from supersonic turbulent filaments. They also found the oscillation in centroid velocity in parallel to the direction of filament elongation, and the pattern of the centroid velocity and the column density has shifted by a $\lambda/4$, where λ is the separation of local peak of column density, i.e. located on dense cores. Those feature are interrupted as motions of fragmentation from a filament to dense cores. Filaments often have subfilaments, which

are located on perpendicular to the main filament. In the subfilaments, the accreting motions toward the main filament are suggested (e.g. Kirk et al., 2013; Palmeirim et al., 2013).

1.2 Motivation of this thesis

It is widely shared that filaments are considered to be a main star-forming site from molecular clouds. Some observational studies have demonstrated velocity fields in a filament, such as accreting motions toward the center of filament through sub-filament and fragmenting motions of filaments to dense cores. Such detailed study of gas kinematics in a filament is not sufficient and therefore the relation between those motions in filaments and the kinematics of dense cores have not been well known. In this study, I will address three important issues related to the low-mass star formation process at sufficient angular resolution in dense gas tracers. First, where is a dense core in a filament forming? Do velocity coherent filaments or multi-fibers exist ubiquitously? Second, are there any trend of a rotating axis with elongation of filaments? Is a rotational axis of dense core correlated with a motion in large-scale? Third, how is an angular momentum distribution within a core? Is a large scale rotation smoothly connected to the inner rotation manifesting a rotating disk or an outflow? I, therefore, observe low-mass dense cores in a filament in nearby star forming regions with the 45 m Telescope at Nobeyama Radio Observatory (NRO 45 m telescope) in various molecular lines. The typical angular resolution is $20''$corresponding to 0.015 — 0.02 pc sufficient to spatially resolve a dense core.

1.3 The Observational Approach

1.3.1 Targets: Low-mass star forming regions of Taurus and Lupus Molecular Clouds

Taurus Molecular Clouds

Taurus Molecular Clouds are one of the closest low-mass star forming regions at a distance of $\sim$ 140 pc (Elias, 1978; Loinard et al., 2007). The recent Herschel results show ubiquitous existence of the filamentary structures in low-mass star forming regions as well as in Taurus (André et al., 2014). Figure 1.2a shows a Herschel 500 μm continuum emission image superposed on the large-scale of ^{12}CO(J=1–0) and ^{13}CO(J=1–0) emission maps by Goldsmith et al. (2008) and Narayanan et al. (2008) with the Five Colleges Radio Astronomy Observatory (FCRAO) telescope. Goldsmith

et al. (2008) derived the mass of the Taurus molecular complex to be $2.4 \times 10^4 M_\odot$ and the column density to be below $2.1 \times 10^{21} \mathrm{cm}^{-2}$ over the regions of the half mass of the cloud. They also found that the large-scale filamentary structures in the view of the CO emission are perpendicular to the large-scale of magnetic field directions. Panopoulou et al. (2014) identified dozens of filament structures using the ^{13}CO map and the Herschel image. Onishi et al. (1996) shows a large-scale dense gas distribution in $C^{18}O$(J=1–0) using the 4 m Telescope at Nagoya University (the $C^{18}O$ velocity-integrated intensity map was shown in Figure 1.2b). Hacar et al. (2013) studied the 10-pc long filament L1495/B213 in Taurus in $C^{18}O$(J=1–0), N_2H^+(J=1–0) and SO(J_N=3_2–6_1) and they found that the filament L1495/B213 is comprised of multiple velocity-coherent substructures, called multi-fibers. Palmeirim et al. (2013) identified striations perpendicular to the L1495/B213 filament in dust continuum emission and ^{13}CO, suggesting that materials will accrete to the main filament through the striations. Some surveys of dense cores have been conducted so far: Mizuno et al. (1994) identified 15 dense cores in $H^{13}CO^+$(J=1–0) with the NRO 45 m telescope. Onishi et al. (1996, 1998, 2002) have reported survey results with $C^{18}O$(J=1–0) and $H^{13}CO^+$(J=1–0) using the 4 m Telescope at Nagoya University and the NRO 45 m telescope, respectively, and detected about 40 dense cores in Taurus, half of which are associated with YSOs. Tatematsu et al. (2004) observed some dense cores in N_2H^+(J=1–0) using NRO 45 m and they suggested that dense cores in Taurus are close to thermally supported during their evolution.

Lupus Molecular Clouds

The Lupus molecular cloud complex is nearby (140 - 200 pc Hughes et al., 1993; Comerón, 2008) low-mass star forming sites which have several filamentary cloud structures identified 9 regions called Lupus 1 to Lupus 9 (Hara et al., 1999). From the polarization of background stars, the projected directions of magnetic field were derived to be perpendicular to the filament (Matthews et al., 2014). Figure 1.3 shows Herschel 500 μm continuum emission images of Lupus 1 and Lupus 3. There are a few protostellar objects, and dozens of prestellar cores (Tachihara et al., 1996; Hara et al., 1999; Rygl et al., 2012) in the Lupus clouds. The global velocity gradient along the filamentary structure was seen in ^{12}CO(1-0) and ^{13}CO(1-0) maps of the NANTEN telescope (Tachihara et al., 2001), but reanalyzing the $C^{18}O$ data reveals finer velocity structures (Hara et al., 1999). The Lupus 1 is suggested to be located close to nearby members of the Sco OB association as indicated by relatively large velocity dispersion of $C^{18}O$ compared to Lupus 3, and Lupus 3 is suggested to be more evolved

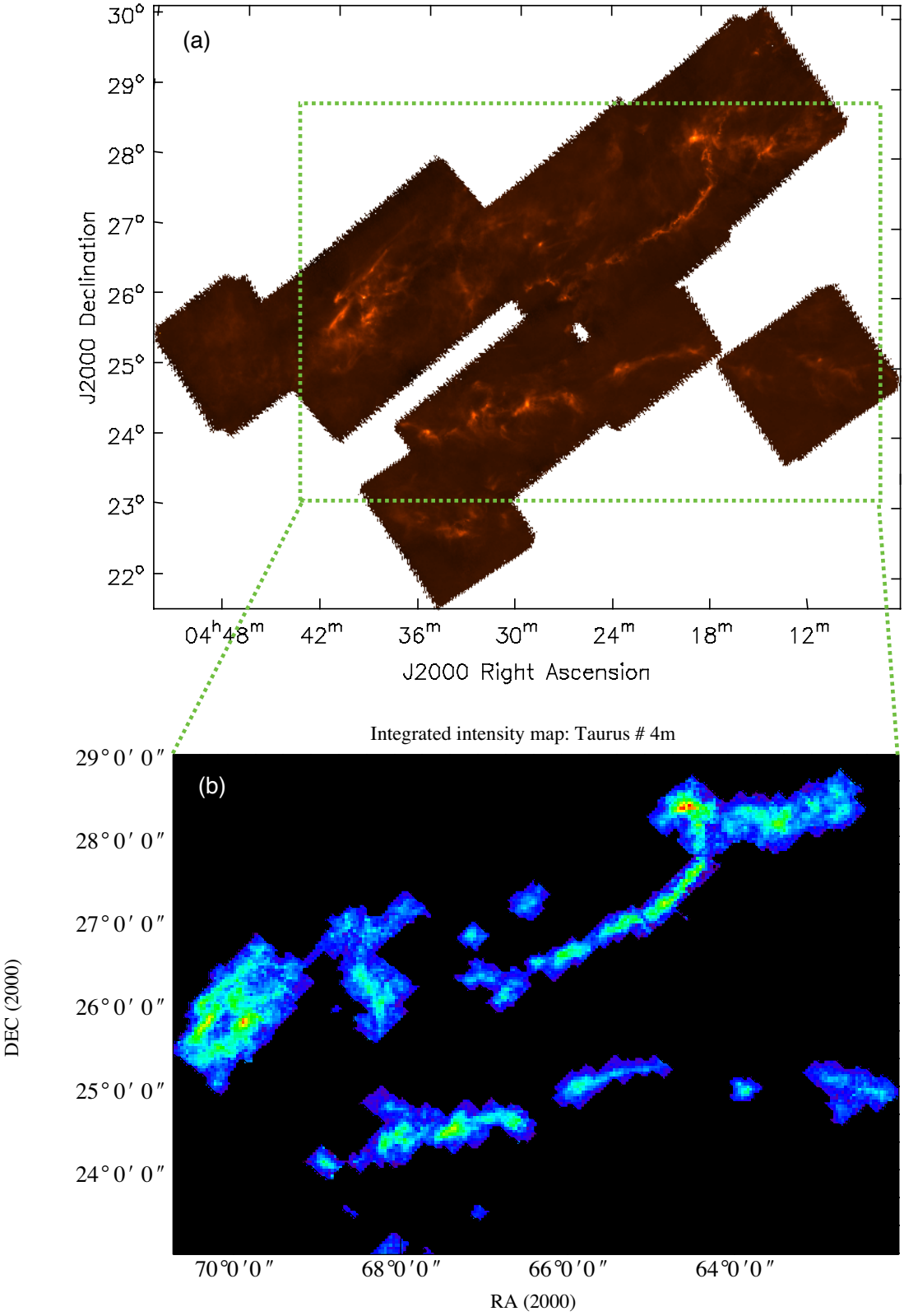

Figure 1.2: (a) Hershel 500 μm continuum emission image of Taurus Molecular Clouds. (b) $C^{18}O(J=1–0)$ velocity-integrated intensity map by Onishi et al. (1996) using the 4 m radio telescope at Nagoya University.

associated with many T Tauri and Herbig Ae stars than Lupus 1 and the Taurus molecular cloud (Rygl et al., 2012). It is reported that at least 4 dense condensations in Lupus 1 and 3 dense condensations in Lupus 3 are embedded in the $C^{18}O$ cores by SEST $H^{13}CO^{+}$ observations (Tachihara et al., 2007). Benedettini et al. (2012) identified eight dense cores for Lupus 1 and five dense cores for Lupus 3 in molecular line tracers.

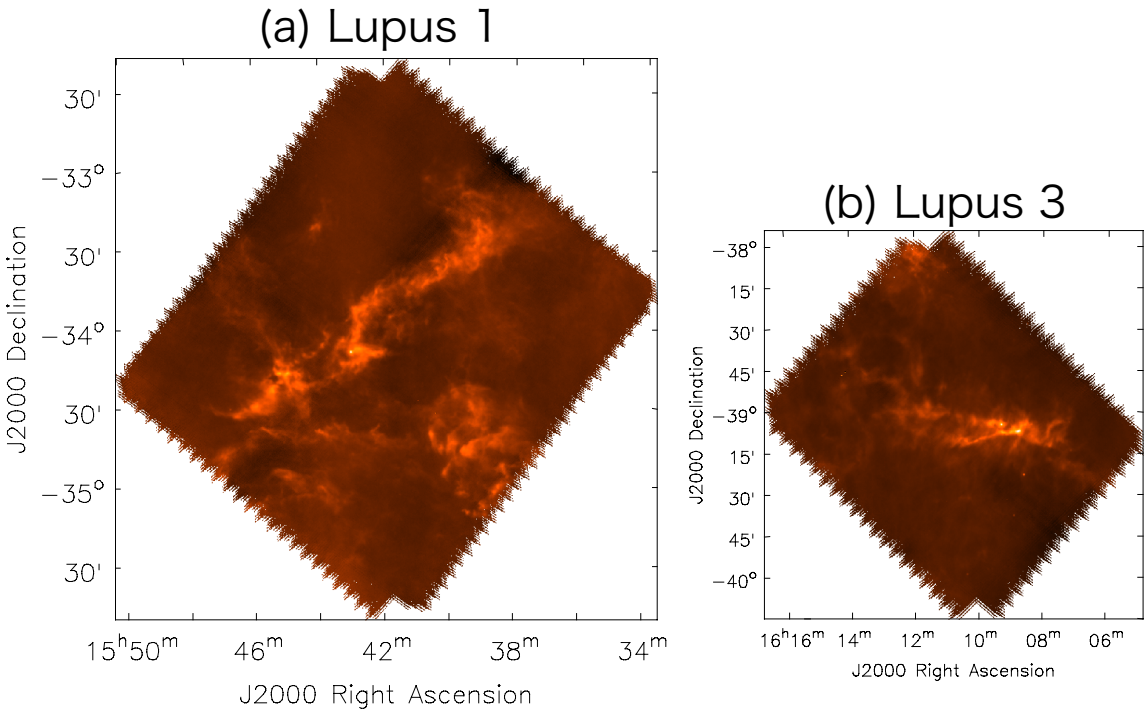

Figure 1.3: Hershel 500 μm continuum emission image of (a) Lupus 1 and (b) Lupus 3

1.3.2 Molecular Line Probes

One of the classical approach searching for dense cores is to detect continuum emission from dust in the millimeter range (e.g. Shirley et al., 2000). Observations of continuum emission have a disadvantage that those have no velocity information and sometimes contain components physically separated by significant distances along the line of sight. Alternatively, the molecular spectroscopy has velocity information and reveals separate the light-of-sight velocity components. It is known that interstellar clouds contain many molecule, which emit during transitions between rotational states that correspond to millimeter wavelength regime. The populations in the rotational energy levels are determined by the physical conditions such as the densities and temperatures.

Carbon monoxide ^{12}CO is the strongest molecular emission line toward infrared dark clouds because it has relatively larger fractional abundance respect to hydrogen molecule than other molecule and has a large dipole moment. This molecular line emission is usually used to identify molecular clouds in a large scale, but easily becomes optically thick in denser regions. Then, it is not suitable to investigate dense cores. To avoid this, one choice is to use rarer isotopologues of CO such as ^{13}CO and C^{18}O. Another choice is to use other molecular lines, which have a higher critical density such as N_2H^+. Further, the molecular abundance respect to hydrogen molecule is expected to change in star formation process, due to chemical reactions in the evolutional stage. The C-bearing molecules, e.g. CO, are known to be depleted from gas phase in cold and dense regime, especially at the very center of starless cores (e.g. Ford & Shirley, 2011). On the other hand, the N-bearing molecules, e.g. N_2H^+, are known to be a good tracer of cold and dense gas, which do not show strong evidence of depletion except at the very center of the cores (e.g. Belloche & André, 2004). In the view of chemical evolution, HC_3N is an interesting molecule, which is formed at very early stage in starless cores and it is depleted quickly at presteller phase, and consequently HC_3N provides us with information of the evolutional stage comparing with the ratio of N_2H^+ and HC_3N. Because it has the higher critical density than carbon monoxide, HC_3N can probe higher density regime instead of CO.

Taking those into account, I selected the molecular transitions of ^{13}CO(J=1–0), C^{18}O(J=1–0), N_2H^+(J=1–0), and HC_3N(J=10–9) in this thesis (Table 1.1), which have the critical densities of 2×10^3, 2×10^3, 1×10^5, and 6×10^5 cm^{-3}, respectively. Using those molecular lines, I can investigate diffuse regime in ^{13}CO(J=1–0) and C^{18}O(J=1–0) and cold dense regime in N_2H^+(J=1–0) and HC_3N(J=10–9) around dense cores.

1.4 Contents in this thesis

In chapter 2, I present an observational study of four dense cores in Taurus Molecular Clouds using the NRO 45 m telescope in ^{13}CO(J=1–0), C^{18}O(J=1–0), N_2H^+(J=1–0), and HC_3N(J=10–9). I found the velocity gradient of each core. One of the targets is L1527 harboring a low-mass Class 0/I source. In L1527, it is known that the velocity gradient on a scale of 0.1 pc is different from that on a small scale of a few au. Then, I invented a new analytical method to derive two dimensional angular momentum distribution and apply to the method to the C^{18}O, N_2H^+, and HC_3N data with the NRO 45 m toward L1527. In chapter 3, I show an observational study of the kinematics of dense cores

Table 1.1: List of Observed Molecules

Molecule	Transition (GHz)	Frequency	Relative strength	$E_{\rm u}$ (K)	$n_{\rm crit}$ ($\rm cm^{-3}$)
N_2H^+	J=1–0, F_1=1–1, F=0–1	93.1716086	0.037	4.47	1×10^5
	J=1–0, F_1=1–1, F=2–2	93.1719054	0.185	4.47	
	J=1–0, F_1=1–1, F=1–0	93.1720403	0.111	4.47	
	J=1–0, F_1=2–1, F=2–1	93.1734675	0.185	4.47	
	J=1–0, F_1=2–1, F=3–2	93.1737643	0.259	4.47	
	J=1–0, F_1=2–1, F=1–1	93.1739546	0.111	4.47	
	J=1–0, F_1=0–1, F=1–2	93.1762527	0.111	4.47	
HC_3N	J=10–9	90.978989		24.01	6×10^5
$C^{18}O$	J=1–0	109.782176		5.27	2×10^3
^{13}CO	J=1–0	110.201354		5.27	2×10^3

in filamentary clouds of Lupus 1 and Lupus 3 using the Mopra 22 m telescope in molecular lines of $C^{18}O$(1–0), N_2H^+(J=1–0), and HC_3N(J=10–9). Those lines have different critical densities of 10^3 - 10^5 $\rm cm^{-3}$, and hence they can probe kinematics with different densities. I derive the velocity gradients and velocity dispersions of those dense cores. In chapter 4, I discuss the outcome of chapter 2 and chapter 3 to make a low-mass star forming scenario. In chapter 5, I summarize this thesis.

Chapter 2

Angular Momentum Distribution within Cores

A case of dense cores in Taurus Molecular Clouds

In this chapter, I present an observational study of dense cores in Taurus Molecular Clouds with the ^{13}CO(J=1–0), C^{18}O(J=1–0), N_2H^+(J=1–0) and HC_3N(J=10–9) emission lines using the NRO 45 m telescope. The aim of the observations is to investigate kinematics around dense cores. These observations identified those cores with masses of 0.7 - 1.9 $M_\odot$ and radii of 0.029 - 0.045 pc in N_2H^+. The velocity gradients of those cores have 1.8 - 4.7 $\mathrm{km\ s^{-1}\ pc^{-1}}$. In the case of L1527, the direction of the velocity gradient is inconsistent with the direction of the known inner disk. Then, I applied a new analytic method to derive the two-demential angular momentum distribution within L1527 using the C^{18}O data. I found that the direction of the angular momentum vector is changing from inner core (0.01 pc $< r <$ 0.02 pc, P.A. $= +90^\circ$) to the outer core (0.02 pc $< r <$ 0.07 pc, P.A. $= -150^\circ$). The rotation axis in the inner core is consistent with the inner disk but it is different from that in the outer core.

2.1 Source Description

Several surveys of dense cores in Taurus molecular clouds (Figure 1.2) have been conducted so far (Mizuno et al., 1994; Onishi et al., 1996, 1998, 2002; Tatematsu et al., 2004). I selected three dense cores of Miz 1, Miz 2 and Miz 7 in the filament L1495/B213 which have strong $H^{13}CO^+$ emission,

and the core name with the prefix of Miz refers to the core number in Mizuno et al. (1994), and also selected L1527, which is a relatively isolated core and is well studied, in order to compare with cores in a filament and isolated cores. The observed targets and their properties are listed in Table 2.1 and the observed regions of Herschel 500 μm continuum emission maps are shown in Figure 2.1. Two dense cores among the four targets have protostars and are relatively well-studied, and then I described about the two dense cores Miz 7 and L1527 with protostars in the following.

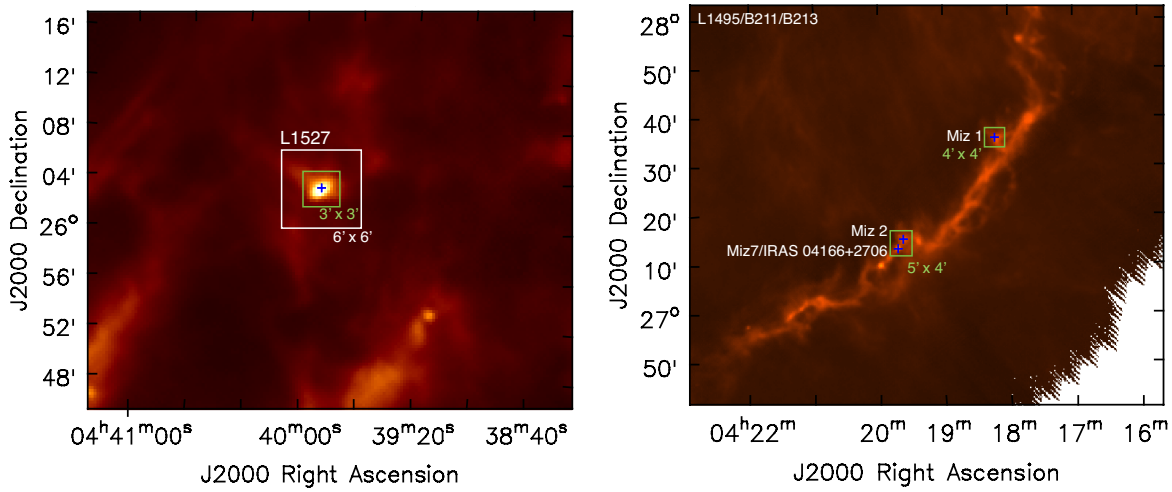

Figure 2.1: Hershel 500 μm continuum emission maps of L1527 and L1495. Boxes indicate observed areas; white box for ^{13}CO(J=1–0) and C^{18}O(J=1–0) observations, and green boxes for N_2H^+(J=1–0) and HC_3N(J=10–9) observations.

Miz 7 (IRAS 04166+2706)

Miz 7 is located in the parent cloud of L1495/B213 in Taurus which is a 10-pc long filamentary cloud (Figure 2.1). Miz 7 contains an IRAS source (IRAS 04166+2706) at the center which is classified as Class 0 object (Chen et al., 2007). The center position is at R.A.=$04^{\rm h}19^{\rm m}42^{\rm s}.5$, Decl.=$+27^\circ13'36''$, which coincides the continuum peak determined by Santiago-García et al. (2009). It has a molecular bipolar outflow (e.g. Bontemps et al., 1996; Narayanan et al., 2012) and the outflow is highly collimated with high velocity emission ranging $V_{\rm LSR} = -50$ to $50\,{\rm km\,s^{-1}}$ (Tafalla et al., 2004). Santiago-García et al. (2009) revealed two components in the outflow, a low-velocity conical shell surrounding a high-velocity jet.

L1527 (IRAS 04368+2557)

L1527 is a relatively isolated dense core in the Taurus molecular cloud. It harbors an IRAS source (IRAS 04368+2557) located at the center, which is considered to be a borderline $\mathrm{Class\,0/Class\,I}$ object (André et al., 2000). A $\mathrm{NH_3}$ core is associated with L1527 with a core size of $0.09 \times 0.07\,\mathrm{pc}$ of a position angle (P.A.) of 8°, a core mass of $2.4\,\mathrm{M_\odot}$, and a velocity gradient of the core is $3.3\,\mathrm{km\,s^{-1}\,pc^{-1}}$ with P.A. of -177° by (Goodman et al., 1993). A molecular bipolar outflow, whose axis is nearly on the plane of the sky ($i\sim 90^\circ$) with the direction of the east and the west, is also associated with L1527 (Bontemps et al., 1996; Tamura et al., 1996; Oya et al., 2015). Its dynamical time scale is estimated to be 2-3 $\times 10^4\,\mathrm{yr}$ (e.g. Hogerheijde et al., 1998; Narayanan et al., 2012). Ohashi et al. (1997a) reported a $\mathrm{C^{18}O}$(J=1–0) flattened envelope on a few thousand au scale using the Nobeyama millimater array. They suggested that L1527 has an infalling envelope with rotation in the scale of $2000\,\mathrm{au}$, whose infall and rotational velocities are estimated to be $\sim 0.3\,\mathrm{km\,s^{-1}}$ and $\sim 0.05\,\mathrm{km\,s^{-1}}$, respectively. The outflow cavity, which is consistent with the direction of the molecular bipolar outflow, is clearly seen in a near infrared image of Spitzer telescope (e.g. Tobin et al., 2008). The opening angle of the outer outflow cavity and the inclination are derived to be 20° and 85°, respectively. Yen et al. (2013) measured the rotational velocity, $V_{\rm rot}$, in L1527 as a function of radius on scales of 100 to 1000 au, and found $V_{\rm rot} \propto r^{-1}$, suggesting that the angular momentum is conserved ($j = constant$) in this scale. Tobin et al. (2012) and Ohashi et al. (2014) have revealed kinematics of the curcumstellar disk in the small scale less than a few hundred au and the central stellar mass is estimated to be 0.2-$0.3\,\mathrm{M_\odot}$ based on the dynamics of the disk. Those observational studies provide the properties and the kinematic structures in the envelope gas around L1527. In the inner part less than $2000\,\mathrm{au}$ scale, the rotational axis is perpendicular to the outflow direction. The outer part, however, has the different direction of velocity gradient (Tobin et al., 2011).

2.2 Observations

Observations were carried out using the NRO 45 m telescope. The sideband-separating (2SB) receivers for 100 GHz band of T100 and TZ were used to detect $\mathrm{C^{18}O}$(J=1–0) and $\mathrm{^{13}CO}$(J=1–0), $\mathrm{N_2H^+}$(J=1–0) and $\mathrm{HC_3N}$(J=10–9) emission lines, respectively. The TZ receiver has been newly installed to the NRO 45 m in 2012. So, the recent observations were carried out using the TZ receiver instead of the T100 receiver.

Table 2.1: Coordinates and Classes of the Observed Sources

Source Name	IRAS Source	R.A. (J2000)	Decl. (J2000)	Parent Cloud Name	Class
L1527	04368+2557	$04^{\rm h}39^{\rm m}53^{\rm s}.9^a$	$+26^\circ03'10''^a$	L1527	0/I
Miz 7	04166+2706	$04^{\rm h}19^{\rm m}42^{\rm s}.5^b$	$+27^\circ13'36''^b$	L1495/B211	0
Miz 2	...	$04^{\rm h}19^{\rm m}37^{\rm s}.0^c$	$+27^\circ15'35''^c$	L1495/B213	Starless
Miz 1	...	$04^{\rm h}18^{\rm m}10^{\rm s}.3^c$	$+27^\circ36'03''^c$	L1495/B213	Starless

References; (a): Peak position of submillimeter continuum emission (Ohashi et al., 2014). (b): Peak position of submillimeter continuum emission (Santiago-García et al., 2009). (c): Peak position of N_2H^+(J=1–0) emission (Tatematsu et al., 2004).

2.2.1 $C^{18}O$(J=1–0) and ^{13}CO(J=1–0) Mapping Observations with the NRO 45 m / T100 H&V

The mapping observations of the $C^{18}O$(J=1–0, 109.782176 GHz) and ^{13}CO(J=1–0, 110.201354 GHz) emission lines toward the L1527 region were carried out with the NRO 45 m telescope during 2012 March—May. I used the sideband-separating (2SB) receiver T100H and T100V, which can detect different linear polarizations (Nakajima et al., 2008). The half-power beam width and main-beam efficiency ($\eta_{\rm MB}$) were $16.8 \pm 0.3''$ and 0.38 ± 0.02 at 110 GHz, respectively. I used the SAM45 spectrometers with 4096 channels for each line and two linear polarizations, with a frequency channel width of $15.26\,{\rm kHz}$, corresponding to a velocity channel width of $0.04\,{\rm km\,s^{-1}}$ at 110 GHz. The observations were made in the On-The-Fly (OTF) mode (Sawada et al., 2008). The mapping center was placed at the IRAS source 04368+2557 in L1527, at ${\rm R.A.} = 04^{\rm h}39^{\rm m}53^{\rm s}.9$, ${\rm Decl.} = +26^\circ03'10''$ (J2000) and the mapping region was $\simeq 6 \times 6\,{\rm arcmin^2}$. I took the off position at $\Delta\alpha = 30'$, $\Delta\delta = 30'$. The system noise temperatures were typically $250\,{\rm K}$ during observations. I obtained ten OTF-scan data over the region in the R.A. and Decl. directions.

The standard chopper wheel method was used to convert the receiver output into $T_{\rm A}^*$ intensity scale. The antenna temperature ($T_{\rm A}^*$) was converted to the main-beam brightness temperature ($T_{\rm MB}$) by $T_{\rm MB} = T_{\rm A}^*/\eta_{\rm MB}$. The relative intensity fluctuation of $C^{18}O$ and ^{13}CO in each polarization from day to day was within $\pm 10\%$, as evaluated from the intensity of the map center (which was made by NOSTER described in section 2.2.3) with each detector of T100H and T100V, separately. The intensity scale of two polarizations was different by 25%, which may be caused by different side

band ratios or some level scaling in the backend. The scaling factor was derived from the cube maps of each polarization and the intensity of map cube with T100V are scaled to that with T100H to be consistent with the past observations within $10\,\%$ by Hayashi et al. (1994) and Fuller & Ladd (2002). The telescope pointing was checked once an hour by five-point observations of the SiO maser from NML-tau in 43 GHz using the HEMT receiver (H40). The pointing accuracies were within $5''$.

2.2.2 N_2H^+(J=1–0) and HC_3N(J=10–9) Mapping Observations with the NRO 45 m / TZ H&V

The mapping observations of the N_2H^+(J=1–0, $93.17\,\mathrm{GHz}$) and HC_3N(J=10–9, $90.978989\,\mathrm{GHz}$) emission lines toward the L1527, IRAS 04166+2706 and Miz 1 regions were carried out with the NRO 45 m during 2014 March—May. I used the sideband-separating (2SB) receiver TZ(H) and TZ(V), which can detect different linear polarizations. The half-power beam width and main-beam efficiency (η_{MB}) were $17.3 \pm 0.3''$ and 0.50 at 90 GHz, respectively. I used the SAM45 spectrometers with 4096 channels for each line and two linear polarizations, with a frequency channel width of $15.26\,\mathrm{kHz}$, corresponding to a velocity channel width of $0.05\,\mathrm{km\,s^{-1}}$ at 90 GHz. The observations were made in the On-The-Fly (OTF) mode (Sawada et al., 2008). The mapping centers were placed at each reference position as follows (Figure 2.1): For L1527, the mapping center postion was set to IRAS source 04368+2557 position of $\mathrm{R.A.} = 04^{\mathrm{h}}39^{\mathrm{m}}53^{\mathrm{s}}.9$, $\mathrm{Decl.} = +26^\circ03'10''$ (J2000) and the mapping size was $\simeq 3 \times 3\,\mathrm{arcmin}^2$. For Miz 7 (IRAS 04166+2706) and Miz 2, those cores are close with a separation of about $2'$, and then the mapping size was $\simeq 5 \times 4\,\mathrm{arcmin}^2$ to cover those cores and to set the center postion as $\mathrm{R.A.} = 04^{\mathrm{h}}18^{\mathrm{m}}8^{\mathrm{s}}.8$, $\mathrm{Decl.} = +27^\circ35'17''$ (J2000). For Miz 1, the mapping center postion was set as $\mathrm{R.A.} = 04^{\mathrm{h}}18^{\mathrm{m}}10^{\mathrm{s}}.3$, $\mathrm{Decl.} = +27^\circ36'03''$ (J2000) and the mapping size was $\simeq 4 \times 4\,\mathrm{arcmin}^2$. The system noise temperatures were typically $200\,\mathrm{K}$ during observations.

The standard chopper wheel method was used to convert the receiver output into T_{A}^* intensity scale. The antenna temperature (T_{A}^*) was converted to the main-beam brightness temperature (T_{MB}) by $T_{\mathrm{MB}} = T_{\mathrm{A}}^*/\eta_{\mathrm{MB}}$. The relative intensity fluctuation of day to day was evaluated by observing near the Ori-KL position, resulting in within 10%, and compared with previous observations by Tatematsu et al. (2004). Comparing the previous observation by Tatematsu et al. (2004), the peak intensities were consistent within 20%. The telescope pointing was checked once an hour by five-point observations of the SiO maser from NML-tau in 43 GHz using the HEMT receiver (H40). The pointing accuracies

were within $5''$.

2.2.3 Reduction

The obtained OTF-scan data were merged to create a final map cube using IDL[a]-based reduction software, NOSTAR (Nobeyama OTF Software Tools for Analysis and Reduction), for flagging, baseline subtraction, making a map cube, and Basket-weave. I adopt a Bessel-Gaussian function (Sawada et al., 2008) as a convolution function (with the function parameters of $\alpha = 1.55$, $\beta = 2.52$) to calculate the intensity at each grid point of the final cube data and the velocity resolution was smoothed to be $0.1\,\mathrm{km\,s^{-1}}$: For $C^{18}O$(J=1–0) and ^{13}CO(J=1–0) data of L1527, the spatial grid size was $7.5''$, resulting in the final effective resolution of $20.4 \pm 0.2''$. For N_2H^+(J=1–0) and HC_3N(J=10–9) data, the spatial grid size was $10.0''$, resulting in the effective resolution of $21.8 \pm 0.1''$. The data sets taken along R.A and Decl. directions were co-added by the Basket-weave method (Emerson & Graeve, 1988) to remove any effects of scanning noise as much as possible. Additionally, the N_2H^+(J=1–0) and HC_3N(J=10–9) data were smoothed spatially with $40.0''$gaussian function to improbe sensitivity so that the effective spatial resolution of the final maps is $45.6 \pm 0.1''$. Finally, the achieved noise level with a velocity resolution of $0.1\,\mathrm{km\,s^{-1}}$ in each data was summarized in Table 2.2 and Table 2.3.

2.3 Results

Figure 2.2 and Figure 2.3 show the velocity-integrated intensity maps of each emission line toward four dense cores. The channel maps of all data are shown in Appendix C.

2.3.1 ^{13}CO(J=1–0) and C^{18}O(J=1–0) toward L1527

Figure 2.2 shows the ^{13}CO(J=1–0) and $C^{18}O$(J=1–0) velocity-integrated intensity maps of L1527. The integrated velocity range in V_{LSR} is from $4.0\,\mathrm{km\,s^{-1}}$ to $8.0\,\mathrm{km\,s^{-1}}$ for ^{13}CO and from $4.7\,\mathrm{km\,s^{-1}}$ to $7.7\,\mathrm{km\,s^{-1}}$ for $C^{18}O$. The ^{13}CO map has a distribution with an elongation from the east to the west although it has a small dynamic range in the integrated intensity from 10 to $13\,\mathrm{K\,km\,s^{-1}}$. The direction of elongation is consistent with the outflow cavity, which has been identified in a mid-infrared image (e.g. Tobin et al., 2008). The $C^{18}O$ emission is also slightly extended in the east-west

[a]The Interactive Data Language

Table 2.2: Summary of the NRO 45 m telescope observations (OTF mapping mode)

Emission Line	ν^a (GHz)	Receiver	$\theta_{\rm HPBW}{}^b$ ($''$)	$\eta_{\rm MB}{}^c$	$\Delta v_{res}{}^d$ ($\rm km\,s^{-1}$)	Area^e ($'$)	$\sigma_{T_{\rm MB}}{}^f$ (K)
L1527							
^{13}CO(1–0)	110.20	T100H&V	22.4 ± 0.4	0.38	0.10	6×6	0.25
C^{18}O(1–0)	109.78						0.22
L1527/Miz 7/Miz 2/Miz 1							
N_2H^+(1–0)	93.17	TZ H&V	45.6 ± 0.1	0.50	0.10	(Table 2.3)	(Table 2.3)
HC_3N(10–9)	90.98						

Table 2.3: Summary of the achieved sensitivities for N_2H^+(1–0) and HC_3N(10–9)

Emission Line	Source Name	Area^e ($'$)	$\sigma_{T_{\rm MB}}{}^f$ (K)
N_2H^+(1–0)	L1527	3×3	0.15
	Miz 7 & Miz 2	5×4	0.12
	Miz 1	4×4	0.10
HC_3N(10–9)	L1527	3×3	0.15
	Miz 7 & Miz 2	5×4	0.11
	Miz 1	4×4	0.10

Notes.
[a] Rest frequency.
[b] Half-power beam width for a Gaussian beam in the final maps.
[c] Main-beam efficiency.
[d] Velocity resolution in the final maps.
[e] Size of the region for the mapping observations.
[f] Typical rms noise level in $T_{\rm MB}$ with the velocity resolution.

direction. Further, the emission is extended toward the northeast and a condensation is located at southwest. The former is also discerned in the N_2H^+ map, and $500\,\mu$m and $850\,\mu$m continuum emission maps (Tatematsu et al., 2004; Tobin et al., 2010; Shirley et al., 2000, see also Figure 2.3a). The latter seems to be physically separated from L1527. So I will not consider the condensation any further in this thesis. In contrast, the main feature of the $C^{18}O$ emission is physically associated with a protostar of IRAS 04368+2557 because the peak $C^{18}O$ emission coincides with the protoster and the emission is roughly axis-symmetric respect to the protostar.

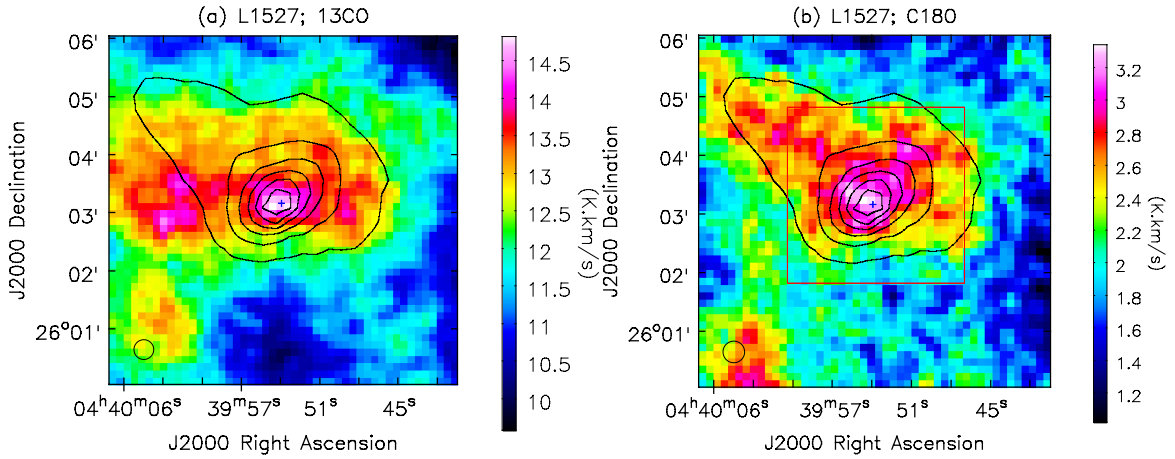

Figure 2.2: Velocity-integrated intensity maps of (a) $^{13}CO(J=1–0)$ and (b) $C^{18}O(J=1–0)$ toward L1527 in T_{MB}(color). Contours show a Herschel 500 μm continuum emission map with 15, 30, 45, 60, 75, 90% levels of the peak of 13.72 Jy/Beam. Cross symbols indicate the center position of IRAS 04368+2557. Red box in $C^{18}O$ map represents the N_2H^+ and HC_3N mapping area.

2.3.2 $N_2H^+(J=1–0)$ and $HC_3N(J=10–9)$ toward L1527/Miz7/Miz2/Miz1

Figure 2.3 shows the $N_2H^+(J=1–0)$ and $HC_3N(J=10–9)$ velocity-integrated intensity maps toward L1527, Miz7, Miz2, and Miz1.

The $N_2H^+(J=1–0)$ maps integrated all seven hyperfine components. The peak intensity toward Miz 7 of $4.5\,\mathrm{K\,km\,s^{-1}}$, is about twice stronger than the other cores, $\sim 2.4\,\mathrm{K\,km\,s^{-1}}$. It was confirmed that the $N_2H^+(J=1–0)$ emission is associated with those cores, reported by Tatematsu et al. (2004). The intensity peak position of L1527 has an offset with $\Delta\alpha = -10''$, $\Delta\delta = 20''$ from IRAS 04368+2557. It is suggested that the N_2H^+ are depleted and destroyed by CO toward IRAS 04368+2557. It is known that N_2H^+ and CO are expected to be anti-correlated. In the early phase, CO is depleted from gas phase to dust under cold and dense environment where N_2H^+ is formed.

In the late phase, a protostar heats up surrounding materials and then CO sublimates from dust and destroys N_2H^+ by chemical reaction.

The HC_3N(J=10–9) emission was detected for all the dense cores. The peak intensity toward L1527 has storg emission of $1.1\,\mathrm{K\,km\,s^{-1}}$, which is 4-5 times stronger than the other cores of $\sim$ 0.20-0.24 $\mathrm{K\,km\,s^{-1}}$. The HC_3N distribution toward L1527 and Miz 1 is very similar to the Herschel 500 μm continuum emission map. Miz 1 has elongated emission in the north direction. The HC_3N emission of Miz 7 and Miz 2 seems to surround the N_2H^+ emission.

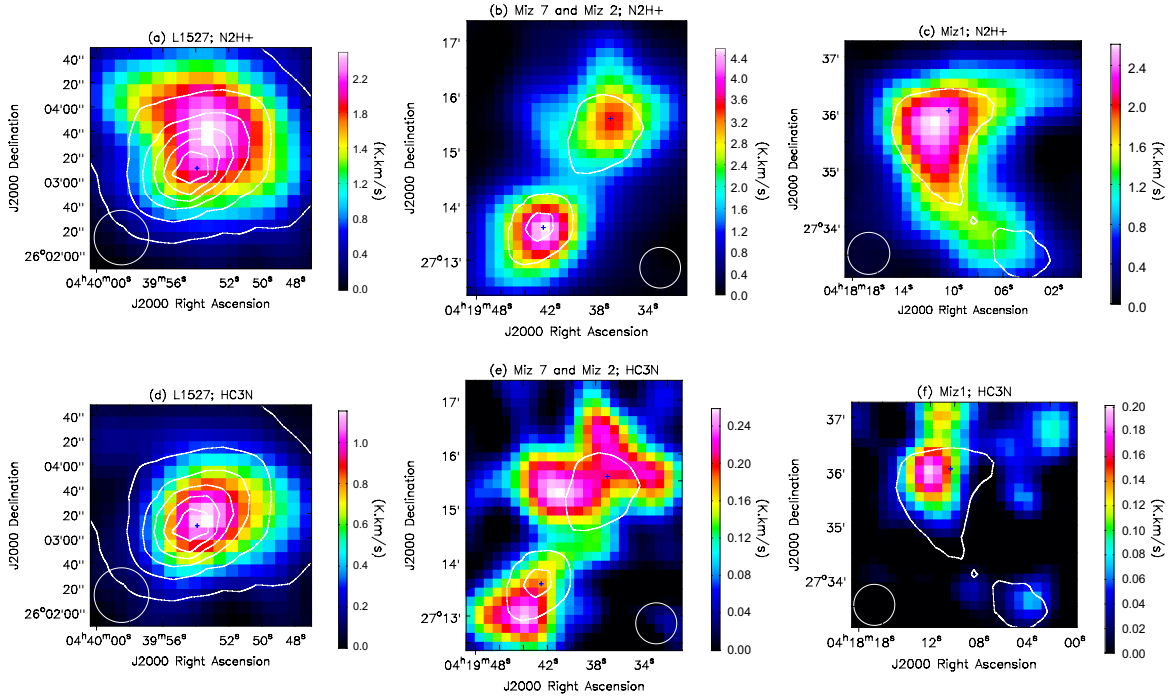

Figure 2.3: Velocity-integrated intensity maps of (a,b,c) N_2H^+(J=1–0) and (d,e,f) HC_3N(J=10–9) toward each core in $T_{\rm MB}$ (color). Contours show Herschel 500 μm continuum emission map with 15, 30, 45, 60, 75, 90% levels of the peak of 13.72 Jy/Beam, same as Figure 2.2. Cross symbols indicate the center position of each core in Table 2.1.

2.4 Analysis

2.4.1 Opacity corrected moment maps for $C^{18}O$(J=1–0)

In order to discuss the kinematics of a core, I conducted opacity correction for the $C^{18}O$(J=1–0) spectra using the brightness temperature ratio of ^{13}CO to $C^{18}O$ (e.g. Myers et al., 1983; Furuya et al., 2014; Dunham et al., 2014). Figure 2.4 shows the line profiles of ^{13}CO and $C^{18}O$ toward the center

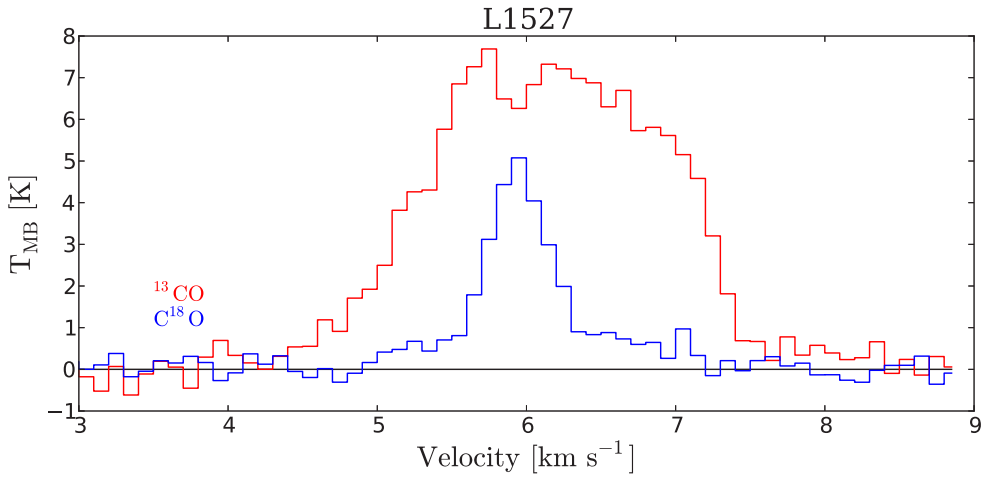

Figure 2.4: Line profiles of ^{13}CO(J=1–0) and C^{18}O(J=1–0) at the center postion of L1527.

position of L1527. The ^{13}CO profile has a self-absorption feature at $V_{\rm LSR} = 5.9\,{\rm km\,s^{-1}}$ where the $T_{\rm MB}[{\rm C^{18}O}]$ is peaked. The ^{13}CO is optically thick with its peak $T_{\rm MB}$ of about 7 K, which implies that the cloud kinematic temperature is close to 10 K considering 2.7 K of the cosmic microwave background temperature ($T_{\rm MB} = T_{\rm K}^{\rm thick} - T_{\rm CMB}$). I assumed a kinematic temperature of 10 K for the analysis presented below. The C^{18}O profile has a single peak. In the optically thin condition, the ratio of the brightness temperature, $T_{\rm MB}[{\rm C^{18}O}]/\,T_{\rm MB}[^{13}{\rm CO}]$, should be close to the molecular abundance ratio of $X[{\rm C^{18}O}]/X[^{13}{\rm CO}]$ as $(5.5)^{-1} = 0.18$ if assuming the same excitation temperature and the abundance ratio as terrestrial elemental abundances. The brightness temperature ratio sometimes is larger than 0.18 in the map whose maximum value is 0.8 in the center at the systemic velocity. These high ratios imply that the C^{18}O emission is partially optically thick. Therefore, I have calculated the opacity of the C^{18}O line (cf. Myers et al., 1983; Furuya et al., 2014; Dunham et al., 2014). Assuming $\tau_{^{13}{\rm CO}} = X[{\rm C^{18}O}]/X[^{13}{\rm CO}] \times \tau_{\rm C^{18}O} = 5.5\,\tau_{\rm C^{18}O}$ and the same excitation temperature, and then the specific intensity ratio is described as follow:

$$\frac{T_{\rm MB}[{\rm C^{18}O}]}{T_{\rm MB}[^{13}{\rm CO}]} = \frac{(1-\exp^{-\tau_{\rm C^{18}O}})}{(1-\exp^{-\tau_{^{13}{\rm CO}}})} = \frac{(1-\exp^{-\tau_{\rm C^{18}O}})}{(1-\exp^{-5.5\,\tau_{\rm C^{18}O}})}. \tag{2.1}$$

I calculated the opacity $\tau_{\rm C^{18}O}$ for each velocity channel where $T_{\rm MB}[{\rm C^{18}O}]$ is over $3\,\sigma$, and I set $\tau_{\rm C^{18}O}$ to be zero where it is less than $3\,\sigma$. As a result, $\tau_{\rm C^{18}O}$ has its maximum of 1.6 at the protostellar

position and its median of 0.12. The most region is optically thin in $C^{18}O$ except around the core center at the systemic velocity. Hereafter, I'll use the opacity corrected data based on the equation of

$$T_{\rm MB}^{\rm corr}[C^{18}O] = \frac{\tau_{C^{18}O}}{(1-\exp^{-\tau_{C^{18}O}})} T_{\rm MB}^{\rm obs}[C^{18}O]. \tag{2.2}$$

Figure 2.5 shows the velocity-integrated intensity map of the $C^{18}O$ after opacity-correction. The integrated velocity range is same as Figure 2.2b, from $4.7\,{\rm km\,s^{-1}}$ to $7.7\,{\rm km\,s^{-1}}$. Comparing the integrated intensity map with and without opacity-correction (see Figures 2.2b and 2.5), the core is more prominent in the opacity corrected map. The first and second moment maps of the opacity-corrected $C^{18}O$ are shown in Figure 2.7a and Figure 2.7b.

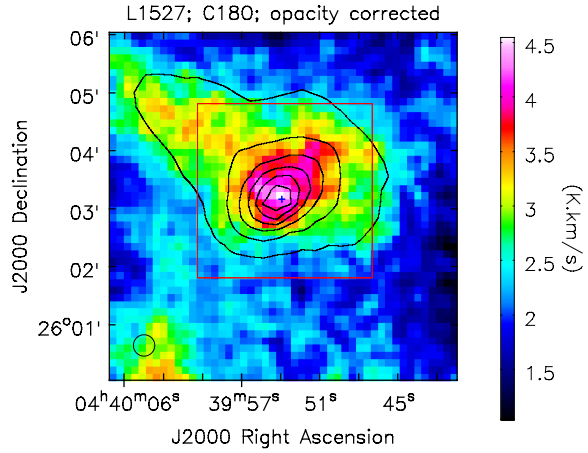

Figure 2.5: Velocity-integrated intensity map of the opacity-corrected $C^{18}O$(J=1–0) toward L1527 in $T_{\rm MB}$ (color). Contours show a Herschel 500 μm continuum emission map with 15, 30, 45, 60, 75, 90% levels of the peak of 13.72 Jy/Beam. Cross symbols indicates the center position of IRAS 04368+2557. Red box represents the N_2H^+(J=1–0) and HC_3N(J=10–9) mapping area.

2.4.2 Hyperfine fitting for N_2H^+(J=1–0)

N_2H^+(J=1–0) line has the hyperfine structures (HFS) with seven components, which provide us with excitation temperature $T_{\rm ex}$ and total optical depth $\tau_{\rm tot}$ which is a sum of optical depths at the centers of the hyperfine components (c.f. Furuya et al., 2006). In the HFS analysis, it is assumed that the velocity shifts of HF components are given (Table 1.1, I used observationally determined values by Tiné et al. (2000)) and the velocity dispersion are same in all HF components and the line profile is a gaussian function. Then, applying the HFS analysis, I derived excitation temperature $T_{\rm ex}$, total

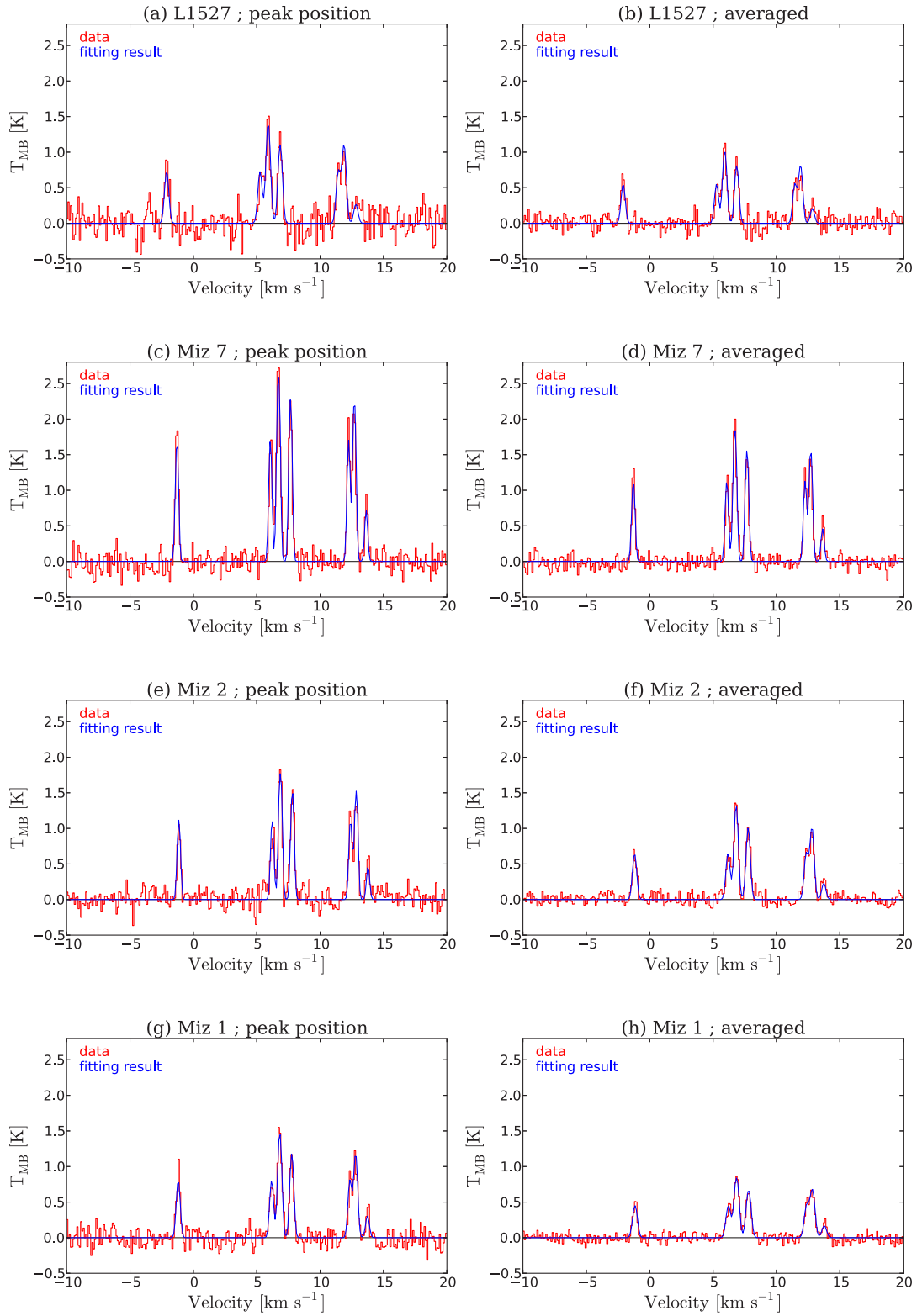

Figure 2.6: Line profiles of N_2H^+(J=1–0). Red lines show the data and bule lines show the results of the HFS analysis. Left column shows the spectrum at peak postion, and right column shows the averaged spectrum within each core area.

optical depth $\tau_{\rm tot}$, center velocity $V_{\rm c}$, and velocity dispersion $\sigma_v = \Delta v/\sqrt{8\ln 2}$ where Δv is velocity width in the full-width at half-maxima. Figure 2.6 and Table 2.4 are the results of the HFS analysis at the center position and the averaged spectrum within the half-maximum contour. Using the results of the HFS analysis, I calculated the column density in the following equation (e.g. Mangum & Shirley, 2015) and the results are also listed in Table 2.4.

$$N_{\rm N_2H^+} = 3.30\times10^{11}\frac{(T_{\rm ex}+0.75)}{1-\exp -4.47/T_{\rm ex}}\left(\frac{\tau_{\rm tot}}{1.0}\right)\left(\frac{\Delta v}{1.0{\rm km\ s^{-1}}}\right)\ [{\rm cm^{-2}}] \tag{2.3}$$

Because the data have low signal to noise ratio and the line intensity ratio between HF components determines the total optical depth τ_{tot}, the obtained total optical depth τ_{tot} has large uncertainties. On the other hand, the center velocity V_c and velocity width Δv are obtained with high accuracy, of which the typical uncertainty is 0.01 $\rm km\ s^{-1}$ and 0.02 $\rm km\ s^{-1}$, respectively. Then, I applied the HPS fitting to all grid points in the maps to obtain center velocity V_c and velocity dispersion σ_v. The $\rm N_2H^+$ center velocity and velocity dispersion maps are shown in Figure 2.7(c,d,e) and Figure 2.7(c,d,e).

Table 2.4: Results of the HFS analysis for $\rm N_2H^+$(J=1–0)

Core	V_c [$\rm km\ s^{-1}$]	Δv [$\rm km\ s^{-1}$]	τ_{tot}	$T_{\rm ex}$ [K]	$N_{\rm tot}$ $\times10^{12}$[$\rm cm^{-2}$]
L1527	5.903 ± 0.009	0.39 ± 0.02	3 ± 3	5.7 ± 0.6	4 ± 5
	5.916 ± 0.007	0.37 ± 0.02	4 ± 2	4.6 ± 0.3	4 ± 2
Miz 7	6.699 ± 0.007	0.27 ± 0.02	5 ± 4	4.8 ± 0.3	4 ± 4
	6.723 ± 0.004	0.29 ± 0.01	6 ± 1	5.4 ± 0.1	6 ± 1
Miz 2	6.865 ± 0.003	0.29 ± 0.01	6 ± 1	5.2 ± 0.1	6 ± 1
	6.819 ± 0.004	0.38 ± 0.01	2 ± 1	6.5 ± 0.5	3 ± 1
Miz 1	6.816 ± 0.007	0.35 ± 0.02	4 ± 2	5.4 ± 0.3	5 ± 3
	6.852 ± 0.006	0.43 ± 0.01	3 ± 1	4.3 ± 0.2	4 ± 1

Notes; The first row refers to the peak spectrum, whereas the second row refers to the averaged spectrum. The uncertainty represents 1 σ fitting error.

2.4.3 Moment maps for $\rm HC_3N$(J=10–9)

The emission line of $\rm HC_3N$(J=10–9) has a sigle profile (Figure 2.9). L1527 has strong $\rm HC_3N$ emission than the other cores, which is also confirmed in the velocity-integrated intensity maps (§2.3.2,

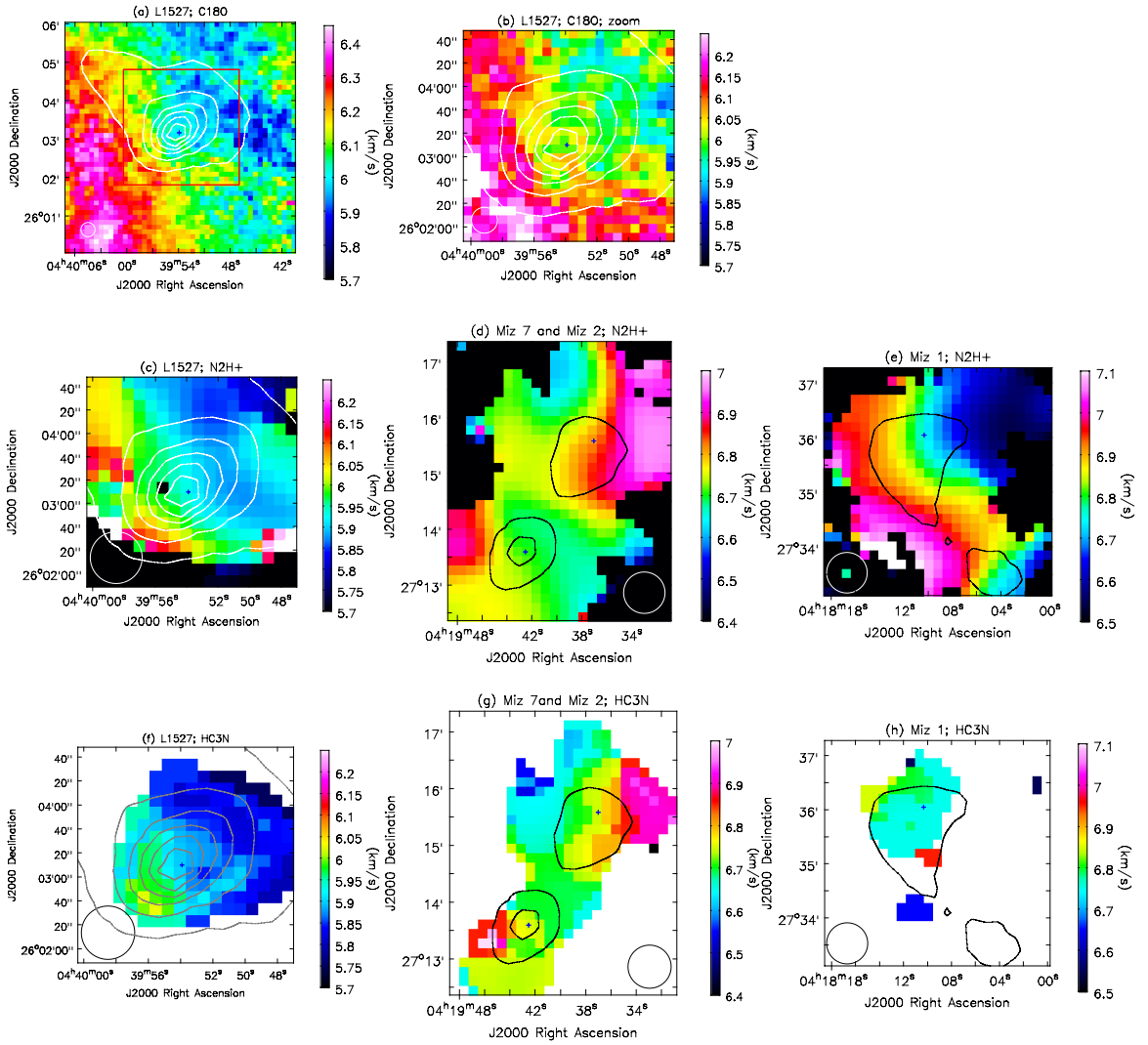

Figure 2.7: Velocity maps of the (a,b) $C^{18}O$(J=1–0), (c,d,e) N_2H^+(J=1–0), and (f,g,h) HC_3N(J=10–9). The velocity maps of $C^{18}O$ and HC_3N were calculated from the first moment of spectra, and that of N_2H^+ shows the result of HFS analysis. Contours show Herschel 500 μm continuum emission map with 15, 30, 45, 60, 75, 90% levels of the peak of 13.72 Jy/Beam, same as Figure 2.2. Cross symbols indicate the center position of each core in Table 2.1.

Figure 2.3d-f). Figure 2.7(f, g, h) and Figure 2.8(f, g, h) show the center velocity and velocity dispersion maps, which were calculated by the first moment, i.e. $v_{1st} = \int T(v) v dv / \int T(v) dv$, and the second moment, i.e. $\sigma_v = \sqrt{\int T(v)(v - v_{1st})^2 dv / \int T(v) dv}$, respectively.

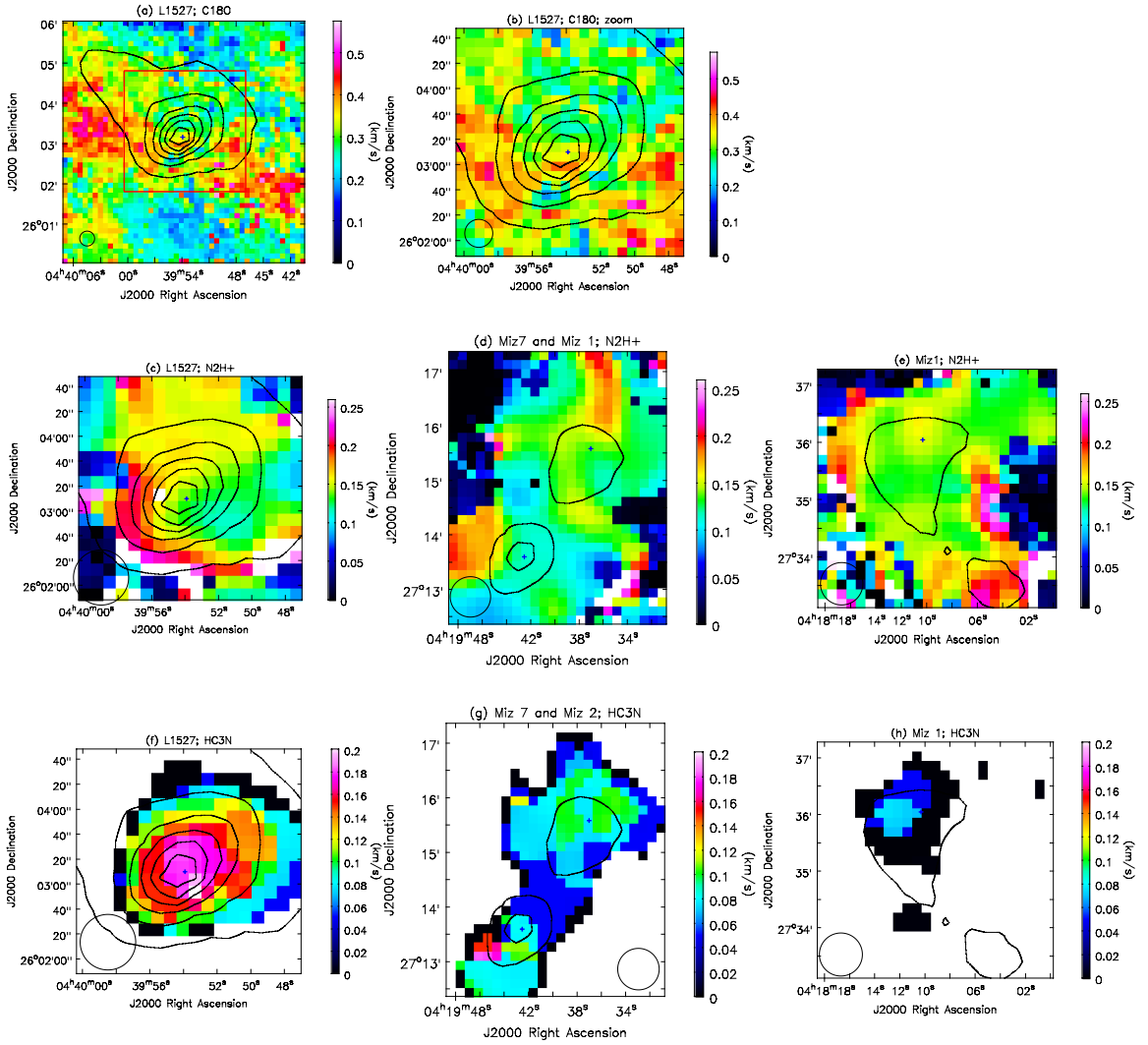

Figure 2.8: Velocity dispersion maps of (a,b) $C^{18}O$(J=1–0), (c,d,e) N_2H^+(J=1–0), and (f,g,h) HC_3N(J=10–9). The velocity dispersion maps of $C^{18}O$ and HC_3N were calculated from the second moment of spectrum, and that of N_2H^+ shows the result of HFS analysis. Contours show Herschel 500 μm continuum emission map with 15, 30, 45, 60, 75, 90% levels of the peak of 13.72 Jy/Beam, same as Figure 2.2. Cross symbols indicate the center position of each core in Table 2.1.

2.4.4 Core properties; Column Density, Core Radius and Mass

Table 2.5 summarizes the physical properties of cores, e.g. the column densities, the core radii and the core sizes.

First, the core radius R is measured as $\sqrt{S/\pi}$ (S is the core area within the half contour). As the results, the radii defined by N_2H^+(J=1–0) and HC_3N(J=10–9) have the range of 0.03 to 0.04

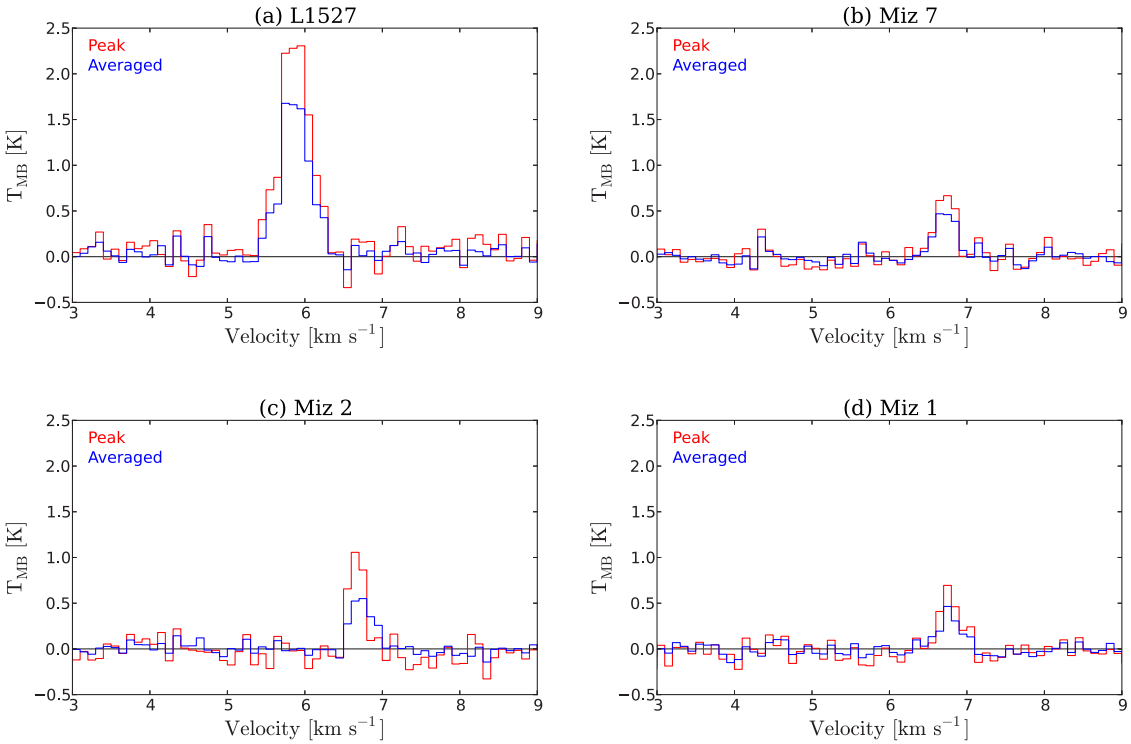

Figure 2.9: Line profiles of HC_3N(J=10–9). Red lines show the spectrum at peak position and blue lines show the averaged spectrum within each core area.

pc and it depends on the cores whether the core radius is larger in N_2H^+ or HC_3N. For example, L1527 and Miz 1 have larger radii in N_2H^+ but Miz 7 and Miz 2 have larger radii in HC_3N. There are no difference in the core radii between starless cores and cores with protoster. The radius defined by $C^{18}O$ toward L1527 have the largest radius as 0.07 pc, among the other molecule lines and the other cores. It suggests that $C^{18}O$ can trace the outer core as well as the inner core probed by N_2H^+ and HC_3N.

Next, to derive the masses of those cores, I calculated the column densities of $C^{18}O$(J=1–0) and HC_3N(J=10–9) as following equations (c.f. Caselli et al., 2002b; Tachihara et al., 2000; Sanhueza et al., 2012):

$$\begin{aligned} N_{\mathrm{C^{18}O}} &= \frac{3k}{8\pi^3\mu^2\nu}\frac{kT_{\mathrm{ex}}}{JhB}\frac{\tau}{1-\exp\left(-\tau\right)}\exp\left(\frac{hBJ(J+1)}{kT_{\mathrm{ex}}}\right)\int T_{\mathrm{mb}}dv \\ &= 5.86\times10^{14}\int T_{\mathrm{mb}}dv[\mathrm{cm}^{-2}] \end{aligned} \tag{2.4}$$

$$
\begin{aligned}
N_{\mathrm{HC_3N}} &= \frac{8\pi\nu^3}{c^3}\frac{Q_{\mathrm{rot}}}{g_{\mathrm{u}}A_{\mathrm{ul}}}\frac{\exp\left(E_{\mathrm{l}}/kT_{\mathrm{ex}}\right)}{1-\exp\left(-h\nu/kT_{\mathrm{ex}}\right)}\int\tau dv \\
&= \frac{8\pi\nu^3}{c^3}\frac{Q_{\mathrm{rot}}}{g_{\mathrm{u}}A_{\mathrm{ul}}}\frac{\exp\left(E_{\mathrm{l}}/kT_{\mathrm{ex}}\right)}{1-\exp\left(-h\nu/kT_{\mathrm{ex}}\right)}\frac{1}{J(T_{\mathrm{ex}})-J(T_{\mathrm{bg}})}\frac{\tau}{1-\exp\left(-\tau\right)}\int T_{\mathrm{mb}}dv \\
&= 7.76\times10^{12}\int T_{\mathrm{mb}}dv[\mathrm{cm}^{-2}] \qquad (2.5)
\end{aligned}
$$

with assumptions of being optically thin $\tau < 1$ and $T_{\mathrm{ex}} = 10$ K and molecule's parameters of $\mathrm{HC_3N}$ taken from Sanhueza et al. (2012). I also set the optically thin condition for the opacity-corrected $\mathrm{C^{18}O}$ data (§2.4.1). The column density of $\mathrm{HC_3N}$ toward L1527 has 4-6 times larger than the other cores but it cannot see the difference between starless cores and cores within protostar. The column densities of $\mathrm{N_2H^+}$(J=1–0) are already derived in §2.4.2 and Table 2.4, and the averaged column densities are re-described in Table 2.5. When deriving the mass of cores, I used the fractional molecular abundance of $X[\mathrm{C^{18}O}] = 1.7\times10^{-7}$ (Frerking et al., 1982) and $X[\mathrm{N_2H^+}] = 3\times10^{-10}$ (Caselli et al., 2002a). It is known that the abundance of $\mathrm{HC_3N}$ quickly varies during the star-forming evolution, and then we cannot obtain the core masses from them. The core mass derived by $\mathrm{C^{18}O}$ toward L1527 is 3.0 $\mathrm{M_\odot}$,and the core masses derived by $\mathrm{N_2H^+}$ are 1.0 to 1.9 $\mathrm{M_\odot}$, which is consistent with previous research by Tatematsu et al. (2004).

Finally, the virial mass of cores has been calculated as

$$
M_{\mathrm{vir}} = \frac{10}{8\ln 2}\frac{R\Delta v_{\mathrm{m}}^2}{\alpha_{\mathrm{vir}}G} \qquad (2.6)
$$

where G is the gravitational constant, R is the core radius. When calculating the virial mass, I use the core radius after correction for the spatial resolution. α_{vir} is defined as $\alpha_{\mathrm{vir}} = (3-p)/(5-2p)$ where p is the power-law index of the density profile. Tatematsu et al. (2004) has been derived the power-law index of the integrated intensity q, and the value of q are in the range of 0.07 to 1.2 of those cores. The power-law index of column density and that of density p are related as $p = q + 1$. Assuming the integrated intensity is proportion to the column density, I set the power-law index of the density profile as $p = 2$ and $\alpha_{\mathrm{vir}} = 1$. The Δv_{m} is the line width of the molecule of mean mass

Table 2.5: Column densities and Masses

Core	Line	R^a [pc]	Δv^b km s^{-1}	$\bar{N}_{\rm line}{}^c$ [cm^{-2}]	$M_{\rm LTE}$ [M$_\odot$]	$M_{\rm vir}$ [M$_\odot$]	$\sigma_{\rm nth}/c_{\rm s}$
L1527	$C^{18}O$	0.070	0.50	1.8×10^{15}	3.0	4.6	1.8
	N_2H^+	0.040	0.35	4×10^{12}	1.5	1.6	0.83
	HC_3N	0.029	0.16	6.3×10^{12}	–	0.7	0.96
Miz 7	N_2H^+	0.029	0.27	6×10^{12}	1.2	0.8	0.52
	HC_3N	0.032	–	1.4×10^{12}	–	–	–
Miz 2	N_2H^+	0.027	0.29	6×10^{12}	1.0	0.7	0.58
	HC_3N	0.046	–	1.5×10^{12}	–	–	–
Miz 1	N_2H^+	0.045	0.35	4×10^{12}	1.9	1.9	0.75
	HC_3N	0.027	–	1.0×10^{12}	–	–	–

Notes;
a: Core radius in the half-width of half maxima.
b: Velocity width in the full-width of half maxima convert from the velocity dispersion maps. For starless core of Miz 2 and Miz 1 it measured at the center position, and for protostellar core of L1527 and Miz 7 it measured at the core edge to minimize the effect of the protostellar collapse and molecular outflow.
c: Averaged column density of each line and the value of the N_2H^+ taken from Table 2.4.
$-$: Very large uncertainty.

($m_{\rm mean} = 2.33$ amu, assuming gas with 90% H_2 and 10% He), and the $\Delta v_{\rm m}$ are calculated as

$$\Delta v_{\rm m}^2 = \Delta v_{\rm obs}^2 - \Delta v_{\rm res,FWHM}^2 + 8 \ln 2 \frac{kT_{\rm ex}}{m_{\rm H}} \left(\frac{1}{m_{\rm mean}} - \frac{1}{m_{\rm obs}} \right) [\rm km\ s^{-1}\ ] \quad (2.7)$$

where $\Delta v_{\rm obs}$ is the observed line width, $\Delta v_{\rm res,FWHM}$ is the velocity resolution of the spectrometer in the full-width of half-maximum (FWHM), and $m_{\rm obs}$ is the mass of the observed molecule in atomic mass units. $\Delta v_{\rm obs}$ are measured at the center position for starless cores and at the near edge of cores for cores with protoster to reduce the effect of the protostellar collapse and molecular outflow. Then, the virial mass are derived as Table 2.5: The virial mass calculated from the N_2H^+ are derived to be 0.7 to 1.9 M$_\odot$, which are comparable to the masses of those cores estimated from the N_2H^+ intensities. Therefore, those N_2H^+ cores are suggested to be gravitational bound. On the other hand, the virial mass derived from $C^{18}O$ toward L1527 has 4.6 M$_\odot$, which is larger than the mass of 3.0

$M_\odot$ estimated from the $C^{18}O$ by a factor of 1.5. This suggests that $C^{18}O$ is affect by the protostellar collapse or molecular outflow, or $C^{18}O$ will trace turbulence motion in the outer core. Here, I check the ratio of the non-thermal velocity dispersions $\sigma_{\rm nth}$ to the sound speed $c_{\rm s}$. The ratio is calculated as

$$\left(\frac{\sigma_{\rm nth}}{c_{\rm s}}\right)^2 = \left(\frac{\Delta v}{c_{\rm s}\sqrt{8\ln 2}}\right)^2 - \left(\frac{\sigma_{\rm th}}{c_{\rm s}}\right)^2 \quad (2.8)$$

where Δv is the observed velocity width, $\sigma_{\rm th}$ is the thermal velocity dispersion given by $kT_{\rm kin}/m_{\rm line}$, and $m_{\rm line}$ denotes the molecular mass of observed molecule. The obtained ratios are shown in Table 2.5. Then, the non-thermal velocity dispersion of $C^{18}O$ has 1.8 times larger than the sound velocity, indicating that $C^{18}O$ traces a supersonic turbulence motion or affected by infall/outflow motions. On the other hand, the non-thermal velocity dispersions of N_2H^+ are less than unity among those dense cores, indicating the thermal motion dominates in the dense gas traced by N_2H^+.

2.5 Discussion

2.5.1 Velocity gradient

The intensity velocity maps are shown in Figure 2.7. Each core has a clear velocity gradient, except for the HC_3N of Miz1 (Figure 2.7h) which has a weak emission and a compact distribution compared with N_2H^+ (Figure 2.3c,f). Following Goodman et al. (1993), I performed a least square fitting of velocity gradient (hereafter velocity gradient fitting, VGF) to the velocity maps of each core defined within the half contour in each molecular line. In the velocity gradient fitting, the uncertainties in the velocity maps were weighted. The uncertainties in the first moment maps were described in Appendix B. For the N_2H^+ velocity maps, the uncertainties were given by the HFS fitting errors. As a result, the obtained velocity gradients are summarized in Table 2.6. The averaged magnitude and position angles (P.A.) of the velocity gradient with different tracers are derived as follows; L1527 has $2.1 \pm 0.9\,{\rm km\,s^{-1}\,pc^{-1}}$ with P.A. of $112 \pm 20°$, Miz 7 has $2.0 \pm 0.9\,{\rm km\,s^{-1}\,pc^{-1}}$ with P.A. of $103 \pm 10°$, Miz 2 has $3.8 \pm 0.4\,{\rm km\,s^{-1}\,pc^{-1}}$ with P.A. of $-113 \pm 4°$, and Miz 2 has $4.7\,{\rm km\,s^{-1}\,pc^{-1}}$ with P.A. of $133 \pm 2°$. The difference in different tracers of each core is almost consistent within 35% in magnitude and 15°in P.A. The velocity gradient in both a N-bearing molecule of N_2H^+ and C-bearing molecules of $C^{18}O$ and HC_3N show the similar features, indicating the effect of a depletion of those molecule does not occur or can be neglected on this scale for the velocity gradient fitting,

Table 2.6: Velocity gradient fitting results

Core	Line	V_{sys} [km s^{-1}]	Velocity gradient [km s^{-1} pc^{-1}]	P. A. [deg]
L1527	$C^{18}O$	6.089 ± 0.003	$2.4^{+0.1}_{-0.1}$	114^{+2}_{-2}
	N_2H^+	5.909 ± 0.002	$1.8^{+0.2}_{-0.2}$	118^{+5}_{-5}
	HC_3N	5.891 ± 0.007	$2.2^{+0.9}_{-0.7}$	105^{+10}_{-19}
Miz 7	N_2H^+	6.714 ± 0.002	$2.0^{+0.2}_{-0.2}$	111^{+5}_{-4}
	HC_3N	6.683 ± 0.017	$2.4^{+0.5}_{-0.5}$	96^{+9}_{-7}
Miz 2	N_2H^+	6.783 ± 0.012	$4.2^{+0.2}_{-0.2}$	-115^{+3}_{-3}
	HC_3N	6.675 ± 0.004	$3.4^{+0.2}_{-0.1}$	-110^{+3}_{-3}
Miz 1	N_2H^+	6.821 ± 0.003	$4.7^{+0.2}_{-0.2}$	133^{+2}_{-2}
	HC_3N	6.765 ± 0.006	$\ldots^a$	$\ldots^a$

Notes;
The uncertainty were estimated by the 1 σ fitting error.
a: Very large uncertainty.

except for HC_3N of Miz 1. Assuming the velocity gradient caused by rigid rotation, we can calculate the centrifugal radius R_c as following equation:

$$R_c \sim 180 \left(\frac{\Omega}{2\,\mathrm{km\,s^{-1}\,pc^{-1}}}\right)^2 \left(\frac{M_*}{0.5\,M_\odot}\right)^3 \left(\frac{c_s}{0.2\,\mathrm{km\,s^{-1}}}\right)^{-8} \quad (2.9)$$

where the Ω is the velocity gradient, c_s is the sound speed, and M_* is the central protostellar mass (Terebey et al., 1984). The obtained velocity gradients of 1.8 - 4.7 km s^{-1} pc^{-1} have the centrifugal radii from a few to a few handred au, which are consistent with a known size of protoplanetry disks.

The velocity gradient of L1527 has been measured in different molecular lines at different scales in past observations. Goodman et al. (1993) derived the velocity gradient to be $3.32 \pm 0.62\,\mathrm{km\,s^{-1}\,pc^{-1}}$ with P.A. of $-177 \pm 13°$ on a scale of 0.045 pc using $NH_3(J,K)$=(1,1) emission, and Tobin et al. (2011) showed the velocity gradient of $2.2 \pm 0.02\,\mathrm{km\,s^{-1}\,pc^{-1}}$ with a $\mathrm{P.A.} = 114 \pm 0.5°$ on a scale of 0.04 pc using N_2H^+(1-0) emission with the single dish telescope. Assuming rigid-rotation and using the above values, the specific angular momentum j is listed in Table 2.7. These results are consistent with Tobin et al. (2011), but it is different by $|\Delta\mathrm{P.A.}| \sim 60°$ between our result and Goodman et al. (1993). It would be due to the lack of the spatial information in the result of Goodman et al. (1993) because they used only 13 spectral points around the center position with a grid separation of $1'$.

2.5.2 Two-dimensional angular momentum distribution of L1527

The directions in P.A. of the velocity gradient in $C^{18}O$, N_2H^+, and HC_3N toward L1527 were derived to be 105 to 118°(Table 2.6). On the contrary, in a scale less than 2000 au (0.01 pc), the rotating infalling envelope and rotationally supported disk are known to have a velocity gradient by rotation at P.A. $\sim 0°$ (Ohashi et al., 1997a; Tobin et al., 2012; Ohashi et al., 2014). Those situations suggest that the direction of a velocity gradient in the core in L1527 may vary at different scales. Therefore, I have performed an analysis of two-dimensional angular momentum applying to $C^{18}O$, N_2H^+, and HC_3N data, which can derive the angular momentum and its direction as a function of radius in a core (hereafter 2-D analysis. The formulation is described in Appendix A). Figure 2.10 shows the result of this 2-D analysis applying to L1527.

First, I focus on the magnitude of the specific angular momentum. The magnitude of the specific angular momentum are corresponding to each tracer of $C^{18}O$, N_2H^+, and HC_3N by a factor of 5 except to the most inner points. The radial dependences of the specific angular momentum j in each tracer are proportional to $j \propto r^{1.5-2}$. The power-law index of 1.6 was obtained from the NH_3 core survey by Goodman et al. (1993) and indicates that the angular momentum are given by turbulence, and the power-law index of 2.0 is in a case of a rigid rotation. The radial dependences of j in

Table 2.7: Specific angular momentum

Reference	Scale[a] (pc)	Scale[a] (au)	Species[b]	j ($\mathrm{km\,s^{-1}\,pc}$)	Direction of j (°)
L1527					
This work with VGF	0.07	14000	$C^{18}O$(1–0)	1.1×10^{-2}	-156
	0.04	8000	N_2H^+(1–0)	2.8×10^{-3}	-152
Tobin et al. (2011)	0.04	8000	N_2H^+(1–0)	3.3×10^{-3}	-156
Ohashi et al. (1997a)	0.01	2000	$C^{18}O$(1–0)	5×10^{-4}	90[c]
Tobin et al. (2012)	5×10^{-4}	100	^{13}CO(2–1)	5×10^{-4}	90[c]
Ohashi et al. (2014)	5×10^{-4}	100	$C^{18}O$(2–1)	5×10^{-4}	90[c]

Notes.
[a] The scale of velocity gradient such as core radius or disk size.
[b] Used molecular line emission.
[c] Measured by P-V diagram along perpendicular to the outflow.
[d] Model fitting based on P-V diagram along perpendicular to the outflow.

$C^{18}O$ and N_2H^+ seem to be approximately proportional to $j \propto r^{1.6}$ while that in HC_3N seems to be proportional to $j \propto r^2$. HC_3N will trace the specific angular momentum in the small scales better than $C^{18}O$ because of their critical densities. N_2H^+ is expected to be affected by depletion in the small scales because the spatial distribution of N_2H^+ is offset from the center position (Figure 2.3a), and then N_2H^+ cannot trace the specific angular momentum in the inner part. In $r < 0.015$ pc, the specific angular momentum j in HC_3N has 3-10 $\times 10^{-4}\,\mathrm{km\,s^{-1}pc}$, which will connect to the rotating infalling envelope identified by an interferometric observation of $C^{18}O$ by Ohashi et al. (1997a). They estimated the rotational velocity as $\sim 0.05\,\mathrm{km\,s^{-1}}$ at $\sim 0.01\,\mathrm{pc}$, which corresponds to a specific angular momentum of $j = 5 \times 10^{-4}\,\mathrm{km\,s^{-1}\,pc}$. Moreover, the magnitude is colse to the specific angular momentum of the inner disk identified by Tobin et al. (2012); Ohashi et al. (2014). Therefore, at about 0.015 pc, there is a transitional regime to conserve the specific angular momentum, $j = constant$.

Next, the directions of the specific angular momentum in the scale between 0.02 pc to 0.07 pc are almost constant with P.A of $-150°$ to $-178°$. The directions are consistent with the results of a least square fitting of velocity gradient. The relation of direction between the specific angular momentum (θ_j) and the rotational velocity gradient (θ_{VGF}) is described as $\theta_j = \theta_{\mathrm{VGF}} + 90°$. Then the directions of the velocity gradient fitting results with $C^{18}O$, N_2H^+, and HC_3N are converted to the directions of j as $-156°$, $-152°$, and $-165°$, respectively. In less than 0.02 pc, the direction of the specific angular momentum traced by $C^{18}O$ and HC_3N are changing from $-150°$ to $90°$ although the errors are relatively high compared to the outer core because of less sampling points. For N_2H^+, the direction of the specific angular momentum in the scale of less than 0.02 pc does not change from the outer scale. N_2H^+ is expected to be affected by depletion, and then N_2H^+ cannot trace the specific angular momentum in the inner part. The inner rotational direction in $C^{18}O$ and HC_3N seems to be connected to the rotation axis of the inner disk (Tobin et al., 2012; Ohashi et al., 2014). Thus, I have confirmed the dense core L1527 cannot be explained by just a single rotation axis. I suggest that the direction changes at a scale less than about 0.02 pc in radius, or at least the direction of rotation in the outer part of the larger scale than 0.02 pc differs from the inner envelope and disk.

The velocity dispersion in $C^{18}O$ increases in the direction of the outflow (Figure 2.7a). The analysis may be influenced by the outflow in the regions of the east and the west. Then I calculated the two dimensional specific angular momentum without an outflow regions with opening angle of $90°$ to avoid those regions. The results is shown as blue points in Figure 2.10, and the angular

momentum with/without the outflow regions have the same feature of the changing direction at a scale less than 0.02 pc.

The dominant error of the 2-D analysis is the accuracy of the center position. One of the other errors is caused by the signal to noise ratio of observations, which is very small compared with the calculated values and can be neglected. Then, to estimate the error effected by the accuracy of the center position, I conducted the 2-D analysis with offset center positions within $\sim 12''$which is the observed beam size in the half-width of the half-maximum. The results are shown in Figure 2.10 as errorbars, which are standard deviations of the calculations with offset center positions.

In the past, there are two approaches to investigate the rotation in cores. One is classical method, which is conducted by the linear or planar fitting of the velocity gradient, such as Goodman et al. (1993), Ohashi et al. (1997a), and Caselli et al. (2002a). The other is analyzing Position Velocity (PV) diagram, which can derive whether rigid-rotation or differential rotation (Belloche et al., 2002). Those methods, however, could not obtain the radial dependence of the rotation axis. Therefore, it is important to analyze the two dimensional specific angular momentum distributions and our newly proposed method is useful when the rotational axis changes as a function of the radius.

2.5.3 Impact to a star formation by the changing specific angular momentum direction

I successfully demonstrated the change of the direction of the specific angular momentum from the inner to outer core of L1527. There are two possible scenarios about the cause to change the direction of the specific angular momentum. One is that the initial condition determines the distribution of the specific angular momentum. The $C^{18}O$ core initially could have the random specific angular momentum if turbulence is dominant in the core. The other is that interaction with a magnetic field changes the direction of the specific angular momentum with the evolution. In theory, the rotational axis changes in the evolution depending on the initial angular momentum and the magnetic field strength (Matsumoto & Tomisaka, 2004).

When the specific angular momentum changes with radius, materials with a different direction of the specific angular momentum will accrete to the inner disk in their evolution and it will cause change in the rotational direction of the inner disk. In such a case, the change in direction of the rotational axis naturally explains existence of YSOs whose outflow axis changes (e.g. Teixeira et al.,

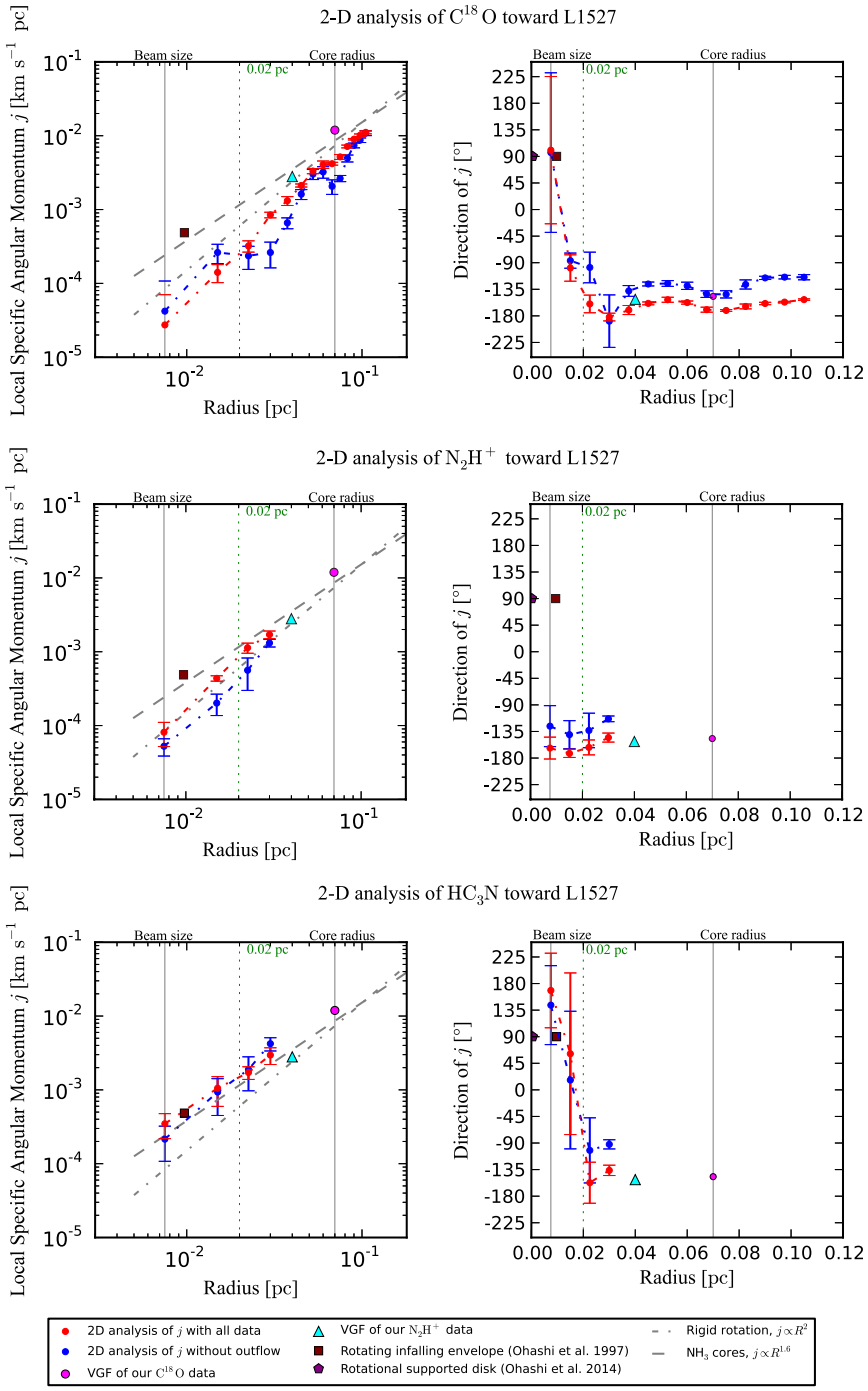

Figure 2.10: Two-dimensional specific angular momentum of (top) $C^{18}O$(J=1–0), (midle) N_2H^+(J=1–0), and (bottom) HC_3N(J=10–9) toward L1527; (left) the magnitude of the specific angular momentum, j [km s^{-1} pc], (right) the direction of the specific angular momentum in degrees. Red and blue points show the results with and without outflow regions, respectively. Other points denote the velocity gradient fitting result of our $C^{18}O$ and N_2H^+ data and past observations. Gray dash-dotted lines show the rigid rotation case of $j \propto R^2$ and gray dashed lines show the relation of $j \propto R^{1.6}$ from NH_3 core survey by Goodman et al. (1993). Gray vertical lines show the half spatial resolution at 0.0075 pc and the $C^{18}O$ core radius of 0.07 pc. Green vertical dotted lines indicate the radius of 0.02 pc, where the direction of the angular momentum changes.

2008). Previously such objects can be explained in terms of precession, but there will be certain cases that the outflow axis changes by accreting material from the outer core with a different rotation axis from the inner one.

2.5.4 Outflowing dense gas around L1527

Figure 2.11 shows the velocity dispersion map of the opacity-corrected $C^{18}O$ with 40″gaussian smoothing. The outside of the $C^{18}O$ core of L1527 is found to have large velocity dispersion. Its extent is at least 0.2 pc from the northeast to the southwest. The velocity dispersion of these regions is approximately 0.40 $\mathrm{km\,s^{-1}}$, 50% largar than that of 0.26 $\mathrm{km\,s^{-1}}$ at the north or south part of the core. Figure 2.12 shows the averaged spectra within the large velocity dispersion regions in Figure 2.11. The $C^{18}O$ spectra of these regions clearly show a shoulder component in the redshifted emission with an offset of $\sim 1\ \mathrm{km\,s^{-1}}$ from V_{LSR}. This offset velocity velocity is larger than the escaping velocity from the core suggesting that the emission is not gravitationally bound. These regions are located on the molecular outflow cavity seen in the scattered light image (Tobin et al., 2008). Furthermore, ^{13}CO interferometric observations revealed V-shaped components in the east and the west that are distributed symmetrically with respect to the central star and resemble the edges of a biconical structure (Ohashi et al., 1997a). Similar features are also found in $H^{13}CO^{+}$ (Saito et al., 2001). Considering these characteristics, the $C^{18}O$ emission with large velocity dispersion seems associated with the walls of the outflow cavity although there is a chance just to trace foreground or background ambient gas emission.

Here, I estimate the outflow momentum from the redshifted component at the west side with the velocity range from 6.5 - 7.2 $\mathrm{km\ s^{-1}}$ (Figure 2.11 and 2.12). The west side is known as location of red lobe of the outflow from other observation (e.g. Narayanan et al., 2012). The east side component has also redshifted component, which would contain the outflow component because the outflow of L1527 has line-of-sight inclination angle of 85°and opening angle of 20°(Tobin et al., 2008) and thus the cavity wall could have red shifted velocity component even in the blue lobe. Since there is relatively a higher contamination with a part of L1527 core due to rotation and the other southeast component. I estimate the outflow momentum only for the west side $C^{18}O$ component. The mass and intensity-weighted averaged velocity of the redshifted component at west side are 0.11 $\mathrm{M_\odot}$ and 0.84 $\mathrm{km\ s^{-1}}$, respectively. Consequently, the momentum is derived to be 0.09 $\mathrm{M_\odot\ km\ s^{-1}}$ (This value would be overestimated by contamination with the L1527 core component). In the past ^{12}CO

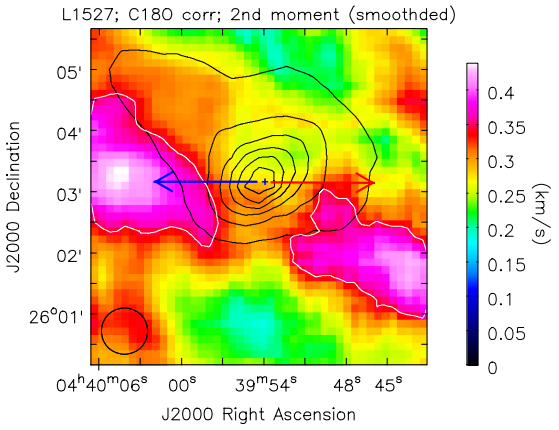

Figure 2.11: Velocity dispersion map of the opacity-corrected $C^{18}O(J$=1–0) smoothed with 40″gaussian function. The original spatial resolution map is shown in Figure 2.8a. White contours show the large velocity dispersion areas. Black contours show a Hershel 500 μm map with 15, 30, 45, 60, 75, 90% levels of the peak of 13.72 Jy/Beam. Cross symbol indicates the position of IRAS 04368+2557 in Table 2.1.

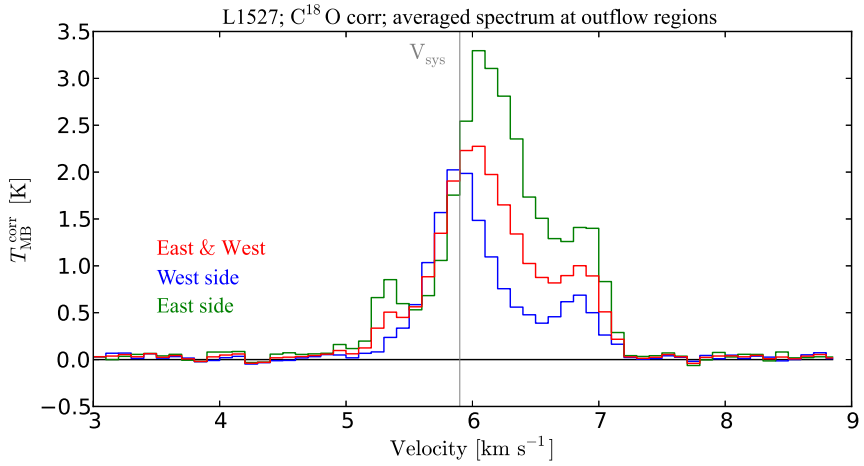

Figure 2.12: Averaged spectra of the opacity-corrected $C^{18}O(J$=1–0) over the large velocity dispersion regions of L1527 shown in Figure 2.11. Green line shows the averaged spectrum of the east side, blue line shows that of the west side, and red line shows that of both sides. Gray vertical line shows the systemic velocity of 5.9 km s^{-1} .

and ^{13}CO observations by Narayanan et al. (2012), the momentum of the red lobe was derived to be 0.03 $M_\odot$ km s^{-1} with its mass of 0.006 $M_\odot$ and mean velocity offset of 4.7 km s^{-1} . Their values are the lower limit by a factor of 2, as they have pointed out, because it is estimated from only high velocity component (relative velocity $>$ 2 km s^{-1}). Therefore, the outflow momentum of dense

gas traced by $C^{18}O$ is comparable to that of defuse gas traced by ^{12}CO and ^{13}CO. Then, the large velocity dispersion of $C^{18}O$ in the outflow direction would be interpreted as the bulk motion of dense gas driven by the outflow. In a low mass star forming senario/evolutional stages, the surrounding materials should be dissipated with some mechanism because the central star is made of only the part of the parent dense core, which is known by comparing with a core mass function and an initial mass function, and the mass accretion rate toward the central star decreases in the evolutional stage in a transition from Class 0 and I to Class II. One such exception is that the material flow toward the outer of the system of outflow/jet destroys its parent core (Nakano et al., 1995). These features may be related to the mechanism of dispersion and dissipation of a natal core causing termination of bulk accretion. The outflowing dense gas is discovered for the first time in low mass star forming region and is related to the mechanism of losing the initial molecular cloud core.

2.6 Summary of this chapter

I have investigated the kinematics around dense cores in Taurus of L1527, Miz 7, Miz2, and Miz 1. The observations were carried out using the NRO 45 m telescope with N_2H^+(J=1–0) and HC_3N(J=10–9) emission lines toward those cores and in addition with ^{13}CO(J=1–0) and $C^{18}O$(J=1–0) toward L1527.

The main results are summarized as follows;

1. N_2H^+ and HC_3N are associated with those dense cores, with the masses of 0.7 - 1.9 $M_\odot$ and the radii of 0.029 - 0.045 pc estimated by N_2H^+. Since the virial masses are smaller than or comparable to the masses derived from N_2H^+, those cores are gravitational bound. The clear velocity gradients were found in the range of 1.8 - 4.7 $\mathrm{km\,s^{-1}\,pc^{-1}}$, and consistent with both lines.

2. I derived the properties of the $C^{18}O$ core in L1527 after opacity correction using the intensity ratio of $C^{18}O$/^{13}CO. The core radius is $0.07\,\mathrm{pc}$, and the mass is $3.0\,M_\odot$. The virial mass is $4.6\,M_\odot$ with a velocity width of $0.50\,\mathrm{km\,s^{-1}}$. The velocity gradient is $2.4 \pm 0.1\,\mathrm{km\,s^{-1}\,pc^{-1}}$ with P.A. of $114 \pm 2^\circ$. Although the virial mass is larger than the mass, the velocity gradient of the $C^{18}O$ is consistent with that of the N_2H^+ and HC_3N. Assuming rigid-rotation, the specific angular momentum is $j = 1.1 \times 10^{-2}\,\mathrm{km\,s^{-1}\,pc}$.

3. The velocity gradient found in L1527 have an inconsistent direction compared with the inner disk or the outflow direction. Then, I have performed an analysis of two-dimensional angular momentum which can derive the angular momentum and its direction as a function of radius within a core. I apply to the $C^{18}O$, N_2H^+, and HC_3N data toward L1527. The radial dependences of the specific angular momentum j in each tracer are derived to be proportional to $j \propto r^{1.5-2}$. The analysis successfully revealed the changing direction of the specific angular momentum from the inner to outer core of L1527. The directions are changing from inner core ($0.01\,\mathrm{pc} < \mathrm{r} < 0.02\,\mathrm{pc}$, P.A. $= +90°$) to outer core ($0.02\,\mathrm{pc} < \mathrm{r} < 0.07\,\mathrm{pc}$, P.A. $= -150°$), Thus, I suggest that the rotating motion in L1527 cannot be explained by just a single rotation axis.

4. The velocity dispersion of L1527 in $C^{18}O$ increases in the northeast and the southwest regions from the center with a 0.2 pc extent which is larger than the size of the $C^{18}O$ core. The mass, averaged velocity, and momentum of the west side of the outflow is derived to be 0.11 $M_\odot$, 0.84 $\mathrm{km\ s^{-1}}$, and 0.09 $M_\odot\ \mathrm{km\ s^{-1}}$, respectively. The outflow momentum in $C^{18}O$ is comparable to the outflow momentum derived from ^{12}CO and ^{13}CO by Narayanan et al. (2012). The increase of velocity dispersion in the outflow direction would indicate the bulk motion of dense gas driven by the outflow, which eventually disperses surrounding core material with evolution.

Chapter 3

Kinematics around dense cores in filamentary Molecular Clouds of Lupus

In this chapter, I present the observational study of dense cores in Lupus Molecular Clouds using the Mopra 22 m telescope in molecular lines of $C^{18}O(1–0)$, N_2H^+(J=1–0), and HC_3N(J=10–9). The targets of dense cores are located on the Lupus 1 and Lupus 3 clouds and the aim of observations is to investigate the kinematics of the dense cores and the surrounding gas in the filaments. The observed lines have different critical density of 10^3 to 10^5 cm^{-3}, and then those emission lines can probe kinematics with different densities. The masses and radii of those cores were derived to be about 1 $\mathrm{M}_\odot$ and 0.02 - 0.04 pc, respectively. I have conducted the velocity gradient fitting, resulting in velocity gradients of 0.9 - 3.2 $\mathrm{km\ s^{-1}\ pc^{-1}}$. It seems that the determined rotational axis of each dense core seems randomly directed compared with the elongation of the filament. The rotational axis of a core would be determined by local physical condition such as turbulent motions. I found that the different density tracers of $C^{18}O$ ($n_{\mathrm{crit}} \sim 10^3$ cm^{-3}), N_2H^+ and HC_3N ($n_{\mathrm{crit}} \sim 10^5$ cm^{-3}) show different velocity gradients at least in the case of observed regions. It is indicated that the relatively lower density tracer of $C^{18}O$ show the large-scale motion in the filament and that the higher density tracers of N_2H^+ and HC_3N show the rotational motion in the core. I also evaluated the non-thermal velocity dispersions which represent degree of turbulent motions, and then the non-thermal velocity dispersions via the sound speed are obtained to be larger than unity for $C^{18}O$ and less than unity for N_2H^+. Those indicates that those dense cores are quiescent within the turbulent surrounding gas.

3.1 Source Description

3.1.1 Lupus Molecular Clouds

The Lupus molecular cloud complex is nearby (140 - 200 pc) low-mass star forming site which has several filamentary cloud structures identified 9 regions called as Lupus 1 to Lupus 9 (Hara et al., 1999). From the polarization of the background stars, projected directions of the magnetic field were derived to be perpendicular to the filament (Matthews et al., 2014). I selected the Lupus 1 (Hughes et al., 1993, at 140 pc) and the Lupus 3 (at 200 pc Comerón, 2008) as targets having several molecular dense cores. There are a few protostellar objects, and dozens of prestellar cores (Tachihara et al., 1996; Hara et al., 1999; Rygl et al., 2012). The global velocity gradient along the filamentary structure was shown in the ^{12}CO(1-0) and ^{13}CO(1-0) maps of NANTEN (Tachihara et al., 2001), but reanalyzing the C^{18}O data reveals finer velocity structures (Hara et al., 1999). The Lupus 1 is suggested to be located close to nearby members of the Sco OB association as indicated by relatively large velocity dispersion of C^{18}O compared to the Lupus 3, and the Lupus 3 is suggested to be more evolved associated with many T Tauri and Herbig Ae stars than the Lupus 1 and Taurus Molecular Clouds (Rygl et al., 2012). It is reported that at least 4 dense condensations in the Lupus 1 and 3 dense condensations in the Lupus 3 are embedded in the C^{18}O cores by SEST H^{13}CO^{+} observations (Tachihara et al., 2007), but the angular resolution is not adequate to study detail structures. Furthermore, Benedettini et al. (2012) identified eight dense cores in the Lupus 1 and five dense cores in the Lupus 3 in various molecular line tracers, but very little kinematic information has been investigated with lack of adequate signal to noise ratios. I have conducted observations toward those 13 dense cores in the Lupus 1 and Lupus 3. Table 3.1 lists the dense cores and their coordinates and Figure 3.1 shows their locations in the cloud overlaid with the Herschel 500 μm continuum emission images. The herschel 500 μm continuum emission images show the long filamentary structure in each cloud, and there are two streams in the Lupus 3. Hereafter, these features in the Lupus 3 are called as the northern and southern filaments.

3.2 Observations

The mapping observations toward the dense cores in Lupus Molecular Clouds at 3 mm were carried out with the Mopra 22 m telescope during 2013 September - October for the Lupus 1 and 2014

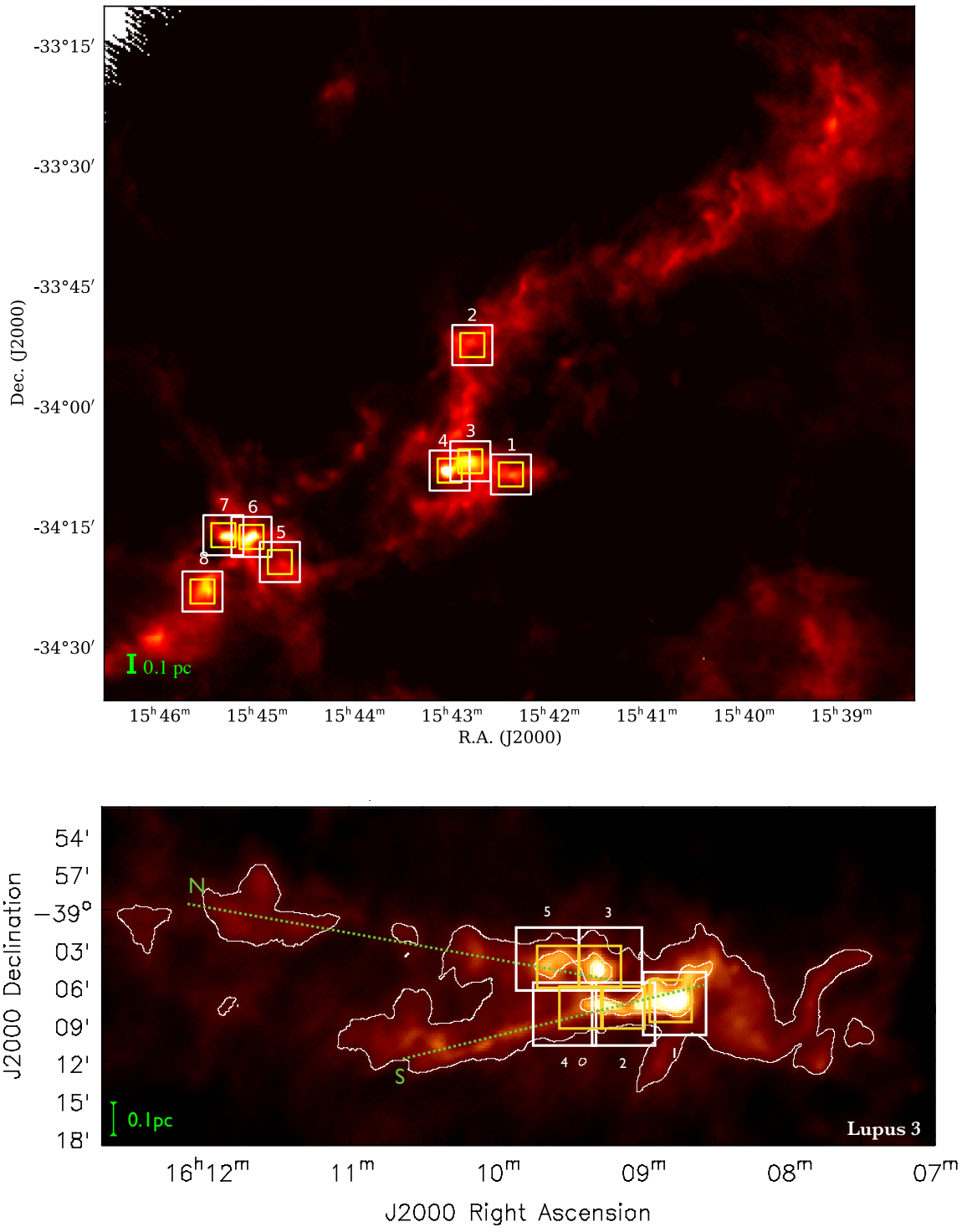

Figure 3.1: Hershel 500 μm continuum emission maps of the Lupus 1 and the Lupus 3. Core identifications are shown. Mapping areas of $C^{18}O$ and N_2H^+ are shown in white and yellow boxes, respectively. In the Lupus 3, there are two streams, called as the northern and southern filaments.

Table 3.1: Dense cores and their coordinates

Core identifier	Right Ascension (J2000)	Declination (J2000)	Starless/Protostar
Lup 1 C1	$15^{\rm h}42^{\rm m}23^{\rm s}.0$	$-34°09'40''.0$	Starless
Lup 1 C2	$15^{\rm h}42^{\rm m}46^{\rm s}.0$	$-33°53'30''.0$	Starless
Lup 1 C3	$15^{\rm h}42^{\rm m}47^{\rm s}.0$	$-34°08'00''.0$	Starless
Lup 1 C4	$15^{\rm h}43^{\rm m}02^{\rm s}.22$	$-34°09'07''.90$	Class 0 source; IRAS 15398-3359
Lup 1 C5	$15^{\rm h}44^{\rm m}43^{\rm s}.0$	$-34°20'25''.0$	Starless
Lup 1 C6	$15^{\rm h}45^{\rm m}00^{\rm s}.0$	$-34°17'15''.0$	Starless
Lup 1 C7	$15^{\rm h}45^{\rm m}17^{\rm s}.0$	$-34°17'00''.0$	Starless
Lup 1 C8	$15^{\rm h}45^{\rm m}30^{\rm s}.0$	$-34°24'00''.0$	Starless
Lup 3 C1	$16^{\rm h}08^{\rm m}49^{\rm s}.7$	$-39°07'20''.0$	Starless
Lup 3 C2	$16^{\rm h}09^{\rm m}16^{\rm s}.5$	$-39°07'13''.0$	Starless
Lup 3 C3	$16^{\rm h}09^{\rm m}19^{\rm s}.0$	$-39°04'44''.0$	Class 0 source; IRAS 16054-3857
Lup 3 C4	$16^{\rm h}09^{\rm m}23^{\rm s}.0$	$-39°06'54''.0$	Starless
Lup 3 C5	$16^{\rm h}09^{\rm m}38^{\rm s}.5$	$-39°05'00''.0$	Starless

Note; the coordinates were taken from Benedettini et al. (2012).

September - October for the Lupus 3. The observations were carried out in the On The Fly (OTF) observing mode with the narrow band mode of the UNSW-Mopra Spectrometer (UNSW-MOPS) digital filterbank backend, and the Monolithic Microwave Integrated Circuit (MMIC) 77-116 GHz receiver. UNSW-MOPS has an 8 GHz bandwidth with four overlapping 2.2 GHz subbands, each subband having four dual-polarization 137.5 MHz wide windows giving a total of 16 dual-polarization windows with 4096 channels. We used two spectral setups in the Zoom Mode of MOPS, at 110 GHz and 90 GHz to probe different density parts. At 110 GHz and 90GHz, the frequency resolution of 33.7 kHz corresponds to a velocity resolution of $\sim 0.09\,{\rm km\,s^{-1}}$ and $\sim 0.11\,{\rm km\,s^{-1}}$, respectively.

In order to cover the core structure, I adopt a scan area as follows: For the 110 GHz setup, a scan area of $5' \times 5'$ for the Lupus 1 and $4.5' \times 4.5'$ for the Lupus 3, corresponds to $\sim 0.20\,{\rm pc} \times 0.20\,{\rm pc}$ at the distance of 140 pc for the Lupus 1 and $\sim 0.26\,{\rm pc} \times 0.26\,{\rm pc}$ at the distance of 200 pc for the Lupus 3, respectively. The 110 GHz setup includes the $C^{18}O(1–0)$ line which has a critical density of $2 \times 10^3\ {\rm cm^{-3}}$. For the 90 GHz setup, a scan area of $3' \times 3'$ corresponds to $\sim\ 0.13{\rm pc} \times 0.13\,{\rm pc}$ for the Lupus 1 and $\sim\ 0.17{\rm pc} \times 0.17\,{\rm pc}$ for the Lupus 3. The 90 GHz setup includes the denser tracers of $N_2H^+(1–0)$ and $HC_3N(10–9)$, both of which have the critical density of about $10^5\ {\rm cm^{-3}}$.

Table 3.2 shows the two spectral settings, the selected molecule lines, and their critical densities. The half-power beam width and main-beam efficiency ($\eta_{\rm MB}$) of the telescope at 3 mm were $32''$ and 0.6, respectively. Each map was scanned at least twice in orthogonal directions in order to minimize artificial stripes and reduce noise level. Data reduction was performed using the ATNF dedicated packages LIVEDATA and GRIDZILLA[a]. LIVEDATA performs a bandpass calibration and baseline fitting while GRIDZILLA regrids and combines the data from multiple scanning directions and maps on to a single data cube. The data were Gaussian smoothed so that the effective spatial resolution of the final maps is $46''$at 3 mm which corresponds to $\sim$ 6400 au (0.03 pc) at 140 pc for the Lupus 1 and $\sim$ 9200 au (0.04 pc) at 200 pc for the Lupus 3.

Table 3.2: Spectral setups

Set-1 (110 GHz)			Set-2 (90 GHz)		
Molecular line	ν [GHz]	$n_{\rm crit}$ [$\rm cm^{-3}$]	Molecular line	ν [GHz]	$n_{\rm crit}$ [$\rm cm^{-3}$]
$\rm C^{18}O(1–0)$	109.782	2×10^3	$\rm HC_3N(10–9)$	90.979	6×10^5
			$\rm N_2H^+(1–0)$	93.173	1×10^5

3.3 Results

3.3.1 Spatial distributions of $\rm C^{18}O$(*J*=1–0), $\rm N_2H^+$(*J*=1–0), and $\rm HC_3N$(*J*=10–9)

Figure 3.2, Figure 3.3, and Figure 3.4 show the velocity-integrated intensity maps of $\rm C^{18}O(1–0)$, $\rm N_2H^+(1–0)$, and $\rm HC_3N(10–9)$, respectively. The channel maps of all data are shown in Appendix C.

The velocity-integrated intensity maps of $\rm C^{18}O$, of which the critical density is $2 \times 10^3 [\rm cm^{-3}]$, are well correlated with the Herschel 500 μm continuum emission images, tracing dust emission. Most cores have $\rm C^{18}O$ emission but Lup 1 C5, C6, C7, and Lup 3 C3 are not prominent. Lup 1 C4, which has the Class 0 protoster IRAS 15398-3359, cannot separate the adjacent core Lup 1 C3. Lup 1 C5, C6, and C7 seem very weak in C18O. Lup 3 C3, which has the protoster IRAS 16054-3857, is associated with relatively weak emission in $\rm C^{18}O$, suggesting depletion. There are two filamentary streams in the Lupus 3 of the Herschel 500 μm map (Figure 3.1). Between these streams, there is velocity difference by 1 $\rm km\,s^{-1}$ in $\rm C^{18}O$ and it was found a double peaked line profile at the intermediate location.

[a]http://www.atnf.csiro.au/computing/software/

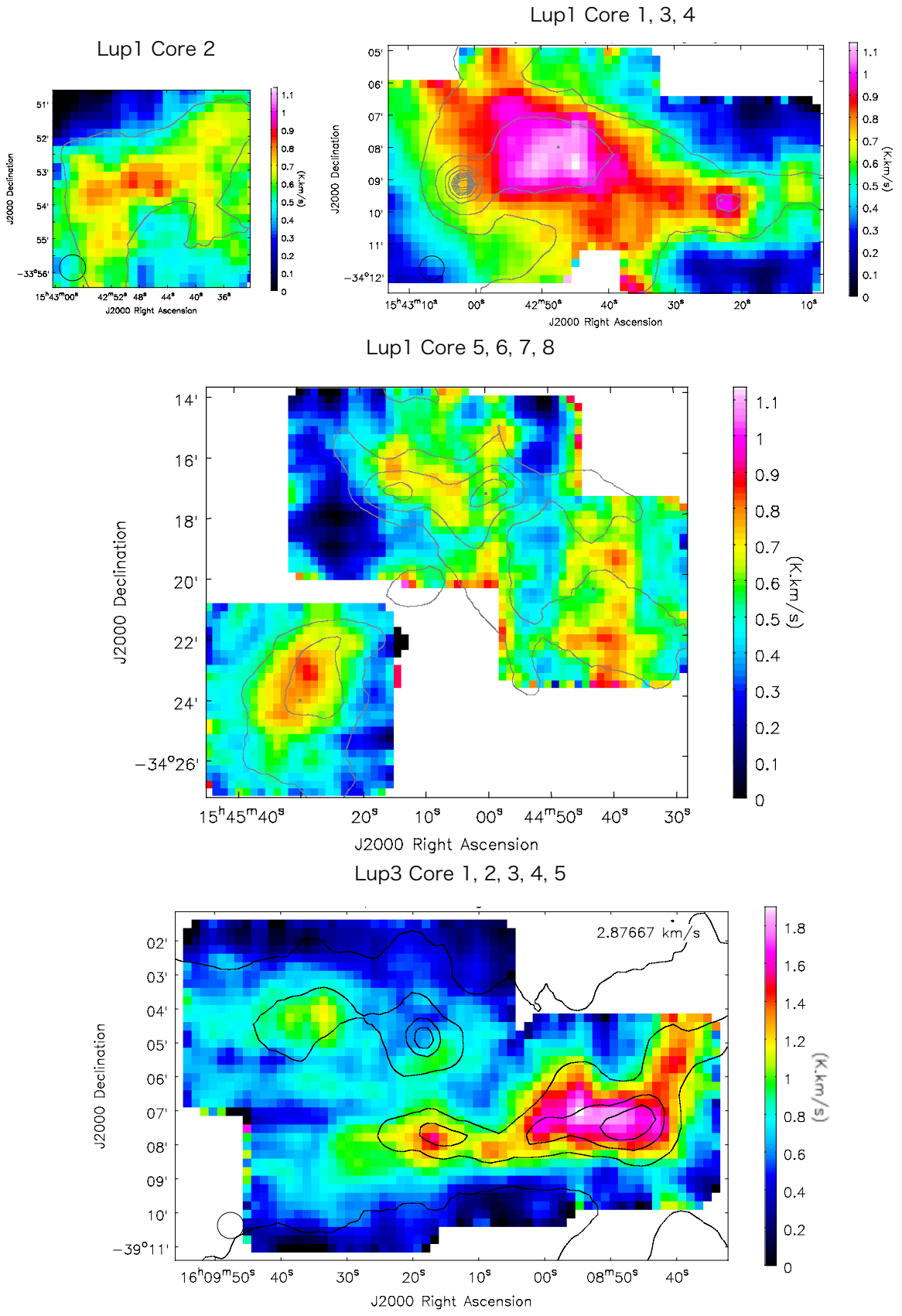

Figure 3.2: Integrated intensity maps of $C^{18}O(J=1–0)$ in T_A^*. Contours show the Herschel 500 μm continuum emission image.

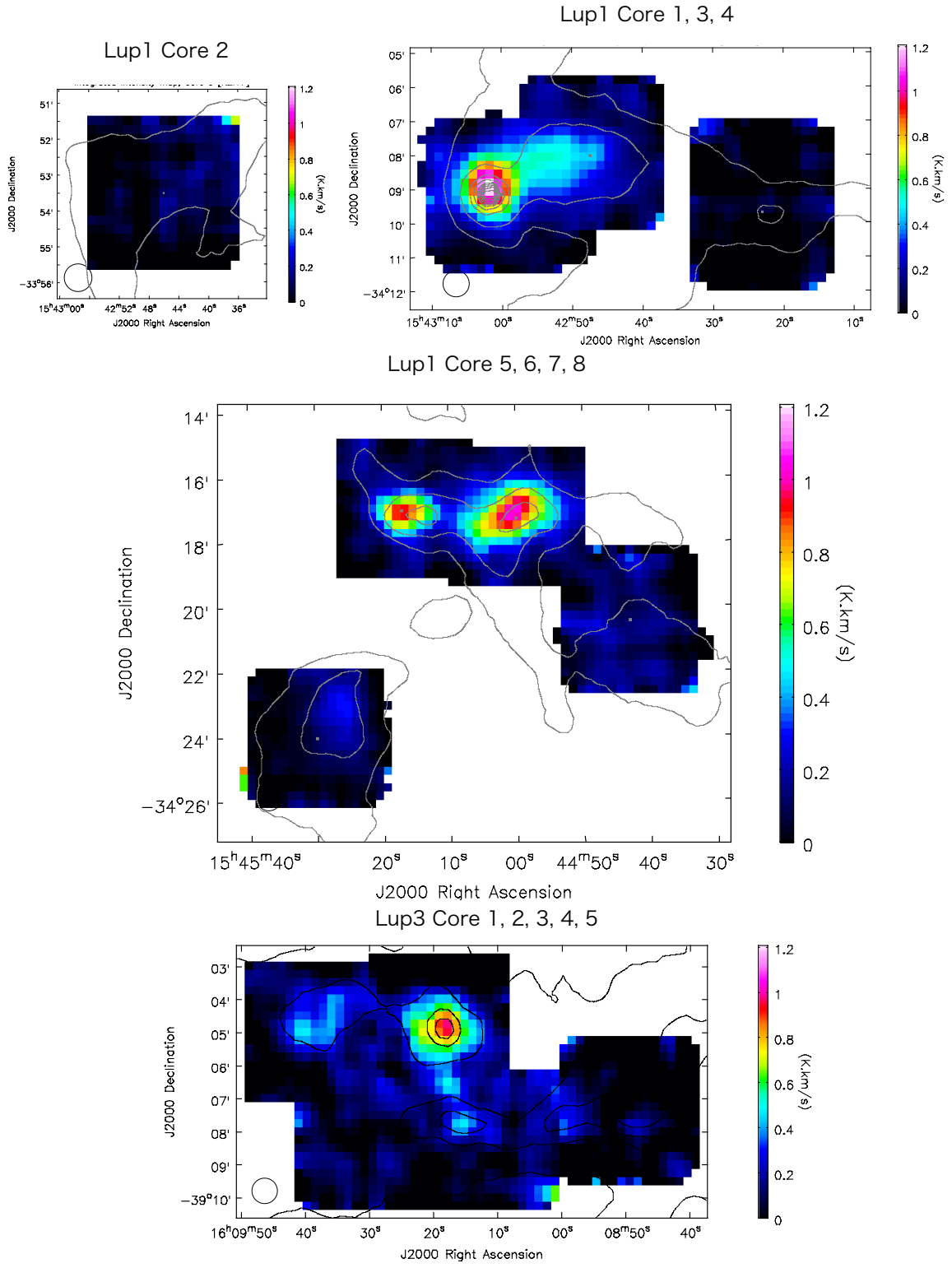

Figure 3.3: Integrated intensity maps of N_2H^+(J=1–0) in T_A^*. All hyperfine components are integrated. Contours show the Herschel 500 μm continuum emission image.

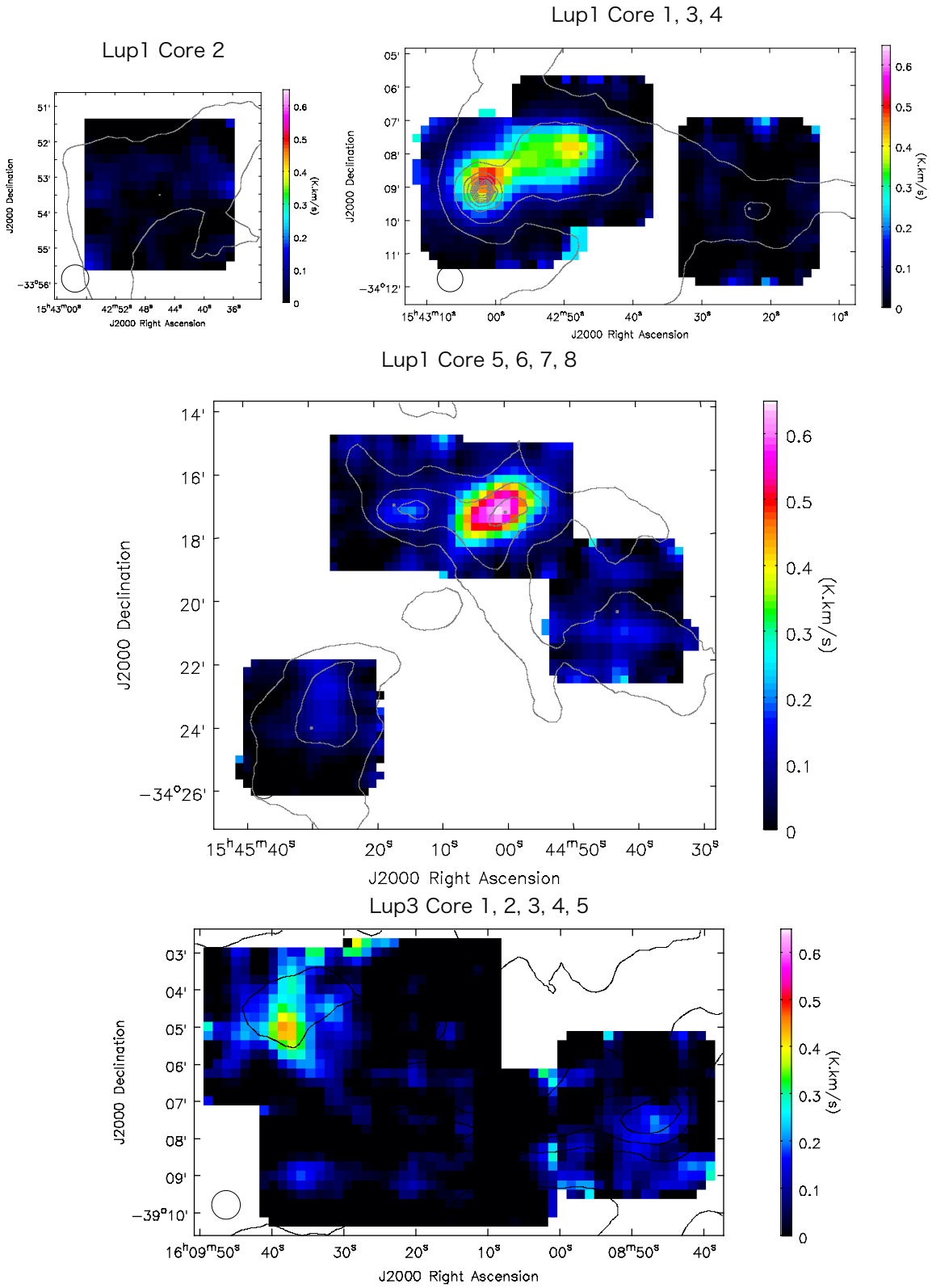

Figure 3.4: Integrated intensity maps of HC_3N(J=10–9) in T_A^*. Contours show the Herschel 500 μm continuum emission image.

Some cores have the denser tracers of N_2H^+ and HC_3N emission with a spherical distribution. There are variations of relative intensity of N_2H^+ and HC_3N among the cores. The Lup 1 C4 and C6 are prominent in both emission. The Lup 1 C7 and Lup 3 C3 are prominent in the N_2H^+ emission while HC_3N are weak. On the other hand, the Lup 1 C3 and Lup 3 C5 are prominent in the HC_3N emission while N_2H^+ are weak. Those features of the N_2H^+ and HC_3N emission are presumably caused by its evolutional stage, and the column densities of those lines are expected to vary with age. Those chemical evolution of these core have already been reported by Benedettini et al. (2012).

In the following discussions, I basically focus on Lup 1 C3, C4, C6, C7, and Lup 3 C3, C5 which have a spherical distribution in N_2H^+ or HC_3N and have enough intensity to probe the velocity structures. The core radii were derived to be 0.02 - 0.04 pc listed in Table 3.3, which was measured as $\sqrt{S/\pi}$ with N_2H^+ (S is the core area within the half contour).

3.3.2 Hyperfine fitting for N_2H^+(J=1–0)

I conducted hyperfine structure (HFS) fitting for N_2H^+(J=1–0) to estimate the masses of the cores. As same as §2.4.2 and using the averaged spectra within the cores, I derived the excitation temperature $T_{\rm ex}$, the total optical depth $\tau_{\rm tot}$, the centroid velocity $V_{\rm c}$, the velocity width Δv, and the total column density $N_{\rm tot}$. Using the results, I derived the masses of the cores and the virial masses. The results are shown in Figure 3.5 and Table 3.3. As a result, the mass have a range of 0.4-1.5 $M_\odot$ and they are larger than its virial masses or comparable to them, suggesting that those cores are gravitational bound.

3.3.3 Velocity fields of $C^{18}O$(J=1–0), N_2H^+(J=1–0), and HC_3N(J=10–9)

Figure 3.6 and Figure 3.7 show the velocity maps of $C^{18}O(1–0)$, $N_2H^+(1–0)$, and $HC_3N(10–9)$. The velocity maps of $C^{18}O$ and HC_3N were produced by the first moment, i.e. $v_{\rm 1st} = \int T(v) v dv / \int T(v) dv$. The N_2H^+ line has seven hyperfine structure transitions. Then, I conducted multi-gaussian fitting toward each grid point to obtain the velocity center and the velocity dispersion, and the results are shown in Figure 3.7 and Figure 3.9, respectively. The latter will be described in §3.3.4.

In the velocity map of $C^{18}O$ around the Lup 1 C3 and C4 shows a velocity gradient from north to south over the region containing the two dense cores, which is consistent with past observation of the NANTEN telescope and $C^{18}O$ will trace motions of the ambient gas on the large-scale in the

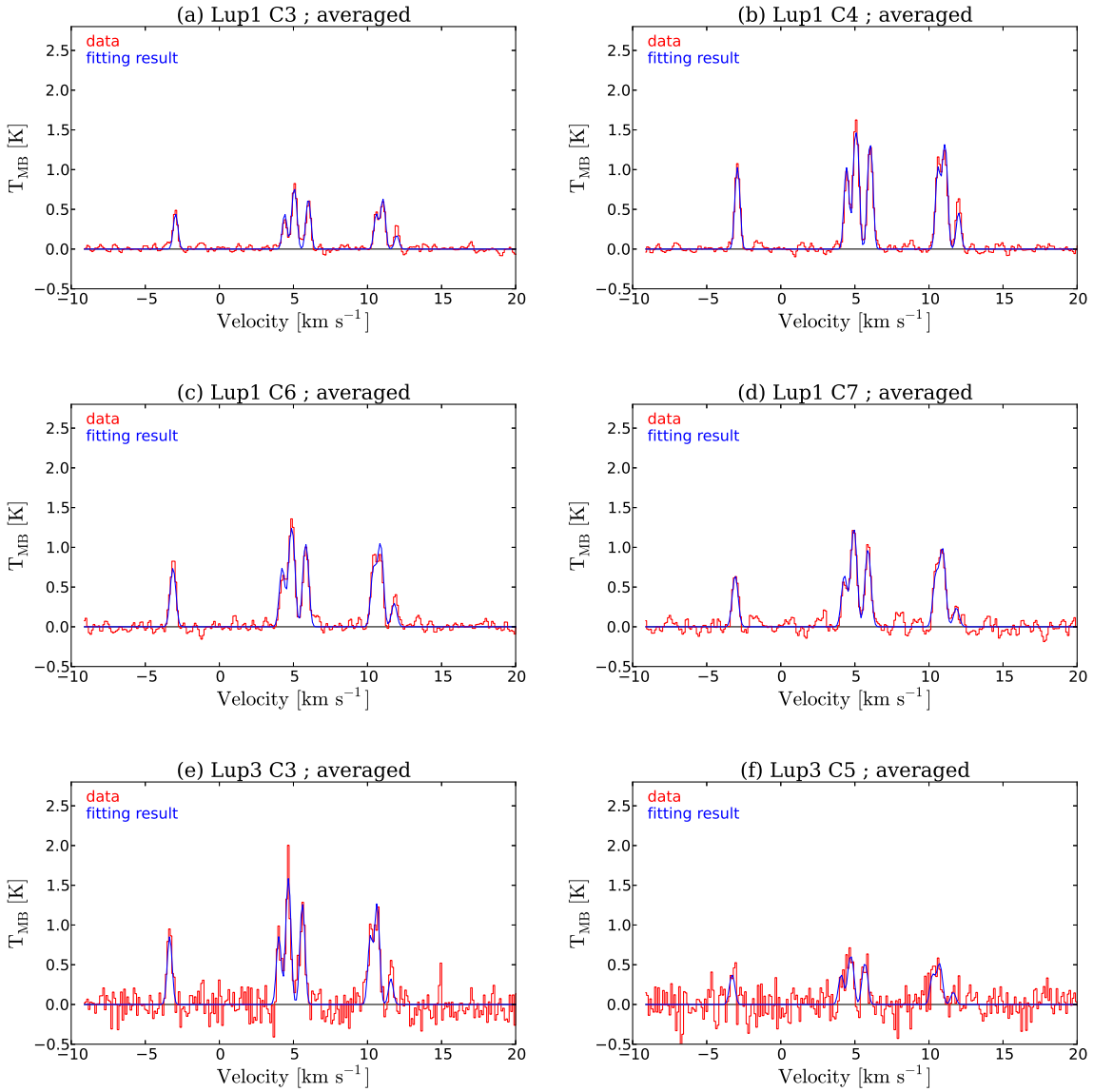

Figure 3.5: Averaged spectra within the cores in N_2H^+(J=1–0). Red lines show the data and bule lines show the results of the HFS analysis.

filaments. In contrast to the $C^{18}O$ results, the velocity fields of N_2H^+ and HC_3N around Lup 1 C3 and C4 show different structures which trace the denser region of about $10^5 cm^{-3}$ than $C^{18}O$ of $10^3 cm^{-3}$. The velocity maps of N_2H^+ and HC_3N show a velocity gradient from the northwest to the southeast around Lup 1 C4 and from the east to the west around Lup 1 C3. They would trace velocities close to the dense cores. Although Lup 1 C6 and C7 do not have clear distributions in the velocity-integrated intensity map due to low sensitivity, there is a velocity gradient from the north to

Table 3.3: N_2H^+(J=1–0) HFS fitting results and core masses

Core	V_c [km s^{-1}]	Δv [km s^{-1}]	τ_{tot}	$T_{\rm ex}$ [K]	$N_{\rm tot}$ $\times 10^{12}$[cm^{-2}]
Lup 1 C3	5.059 ± 0.003	0.34 ± 0.01	4.7 ± 0.5	4.0 ± 0.1	3.7 ± 0.4
Lup 1 C4	5.083 ± 0.002	0.35 ± 0.01	9.0 ± 0.2	4.6 ± 0.1	8.8 ± 0.2
Lup 1 C6	4.883 ± 0.004	0.41 ± 0.01	5.3 ± 0.4	4.6 ± 0.1	6.1 ± 0.6
Lup 1 C7	4.933 ± 0.005	0.44 ± 0.01	2.8 ± 0.6	5.4 ± 0.3	5.2 ± 1.0
Lup 3 C3	4.659 ± 0.006	0.36 ± 0.02	3.5 ± 1.6	5.7 ± 0.4	4.9 ± 2.3
Lup 3 C5	4.726 ± 0.026	0.39 ± 0.06		3.6 ± 0.3	

Notes. The uncertainty represents 1 σ fitting error.

Core	R [pc]	M [M$_\odot$]	$M_{\rm vir}$ [M$_\odot$]
Lup 1 C3	0.033	0.9	0.9
Lup 1 C4	0.021	0.9	0.4
Lup 1 C6	0.025	0.9	0.7
Lup 1 C7	0.018	0.4	0.4
Lup 3 C3	0.032	1.2	0.8
Lup 3 C5	0.042	1.5	1.2

the south. It can also be seen in the velocity maps of N_2H^+ and HC_3N around Lup C6 and C7. Lup 1 C2 and C8, which have condensations with the $C^{18}O$ emission, do not have a clear velocity gradient. The velocity map of $C^{18}O$ for the Lupus 3 shows a clearly velocity difference between the northern and southern filaments, and cloud not find a clear velocity gradient over each core.

3.3.4 Velocity dispersion maps of $C^{18}O$(J=1–0), N_2H^+(J=1–0), and HC_3N(J=10–9)

Figure 3.6 and Figure 3.7 show the velocity dispersion maps of $C^{18}O(1–0)$, $N_2H^+(1–0)$, and $HC_3N(10–9)$. The velocity dispersion maps of $C^{18}O$ and HC_3N were produced by the second moment, i.e. $\sigma_v = \sqrt{\int T(v)(v - v_{\rm 1st})^2 dv / \int T(v) dv}$, and the velocity dispersion maps of N_2H^+ were produced by the HFS fitting.

The dense cores in the Lupus 1 have the velocity dispersions in $C^{18}O$ with a range of 0.2-0.4 km s^{-1} . There are no significant difference between the starless cores (0.2-0.4 km s^{-1}) and the pro-

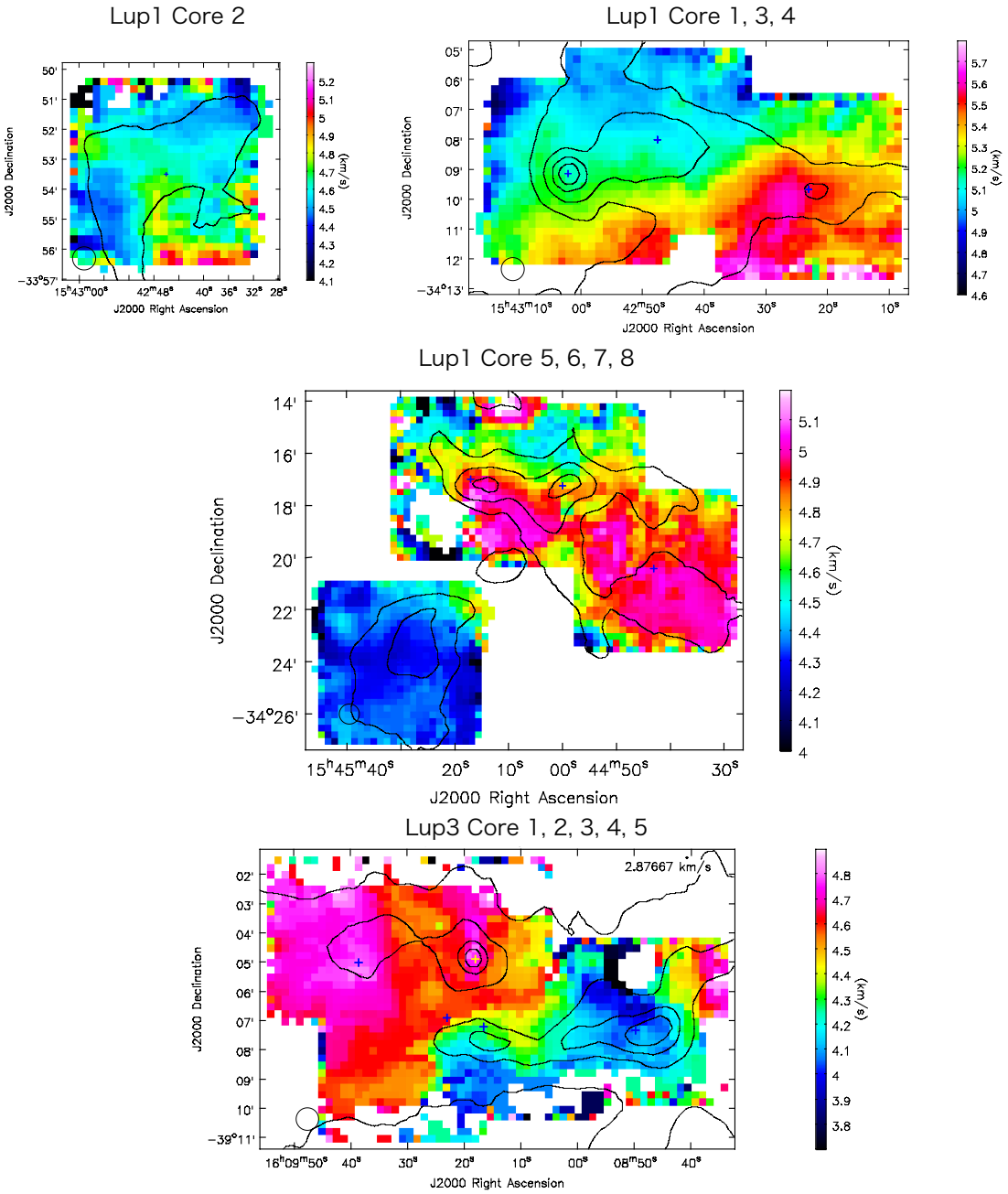

Figure 3.6: Velocity maps of $C^{18}O(J$=1–0) calculated from the first moment. Contours show the Herschel 500 μm continuum emission images.

tostellar core ($\sim$0.25 km s^{-1}). In the Lupus 3, the southern filament has a larger velocity dispersion of 0.2-0.4 km s^{-1} in $C^{18}O$ than those of about 0.15 km s^{-1} in the northern filament. It is suggested that the southern filament is in more turbulent environment than the northern filament.

The velocity dispersions with N_2H^+ and HC_3N emission around dense cores show almost similar values at each core center: 0.14 km s^{-1} in both lines for Lup 1 C3 and C4, 0.18 km s^{-1} in both lines

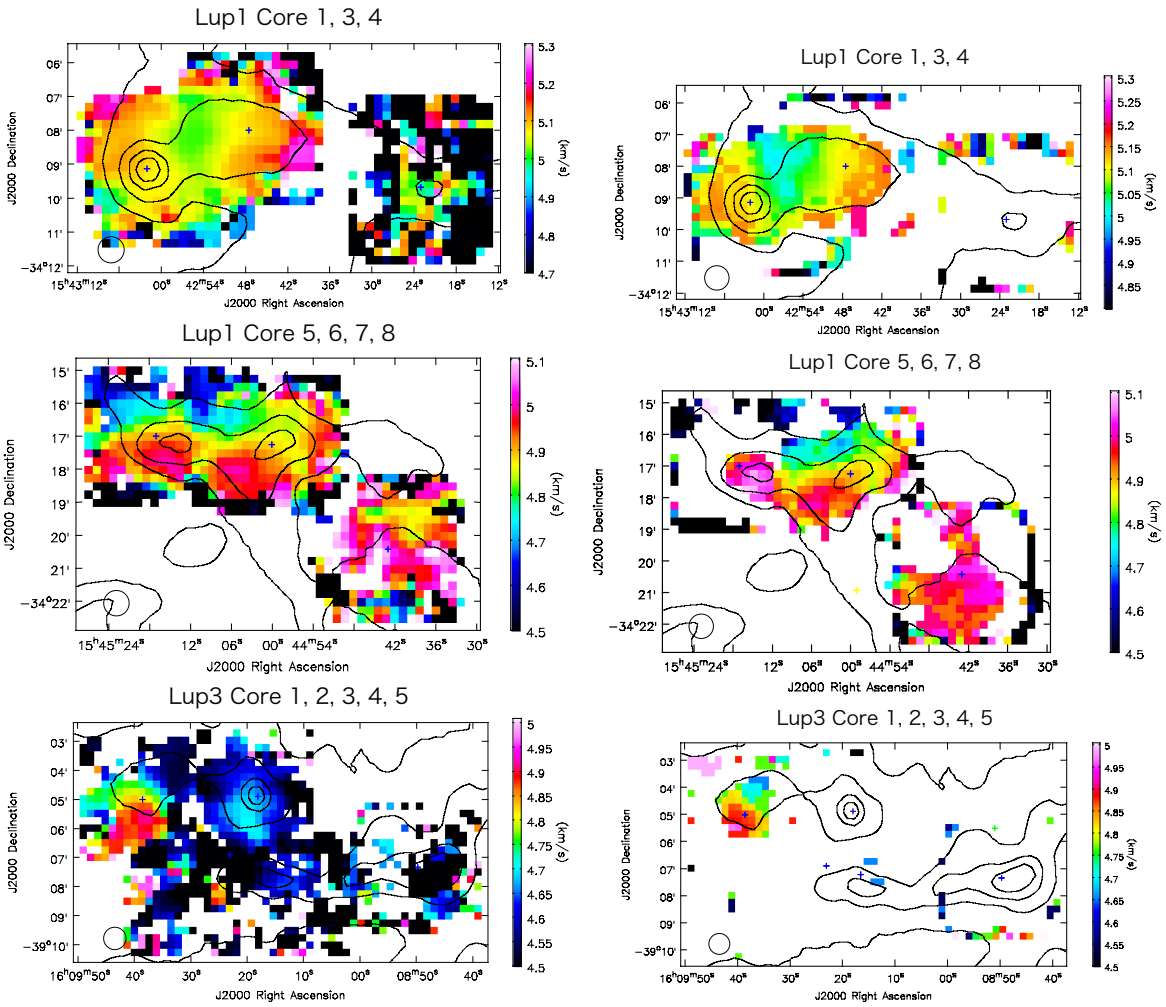

Figure 3.7: (left) Velocity maps of N_2H^+(J=1–0) produced by the HFS fitting. (right) Velocity maps of HC_3N(J=10–9) calculated by the first moment. Contours show the Herschel 500 μm continuum emission images.

for Lup 1 C6, 0.14-0.16 $\mathrm{km\ s^{-1}}$ in N_2H^+ for Lup 1 C7 and Lup 3 C3 which have weak in HC_3N, and 0.10 $\mathrm{km\ s^{-1}}$ in HC_3N for Lup 3 C5 which have weak in N_2H^+. There are no significant difference of velocity dispersions among the starless cores of 0.10-0.16 $\mathrm{km\ s^{-1}}$ and the protostellar cores of about 0.14 $\mathrm{km\ s^{-1}}$.

3.4 Discussion

3.4.1 Velocity gradient

Figure 3.6 and Figure 3.7 show the velocity maps of $C^{18}O$(1–0), N_2H^+(1–0), and HC_3N(10–9) (§3.3.3). Following Goodman et al. (1993), I have conducted a least square fitting of velocity gra-

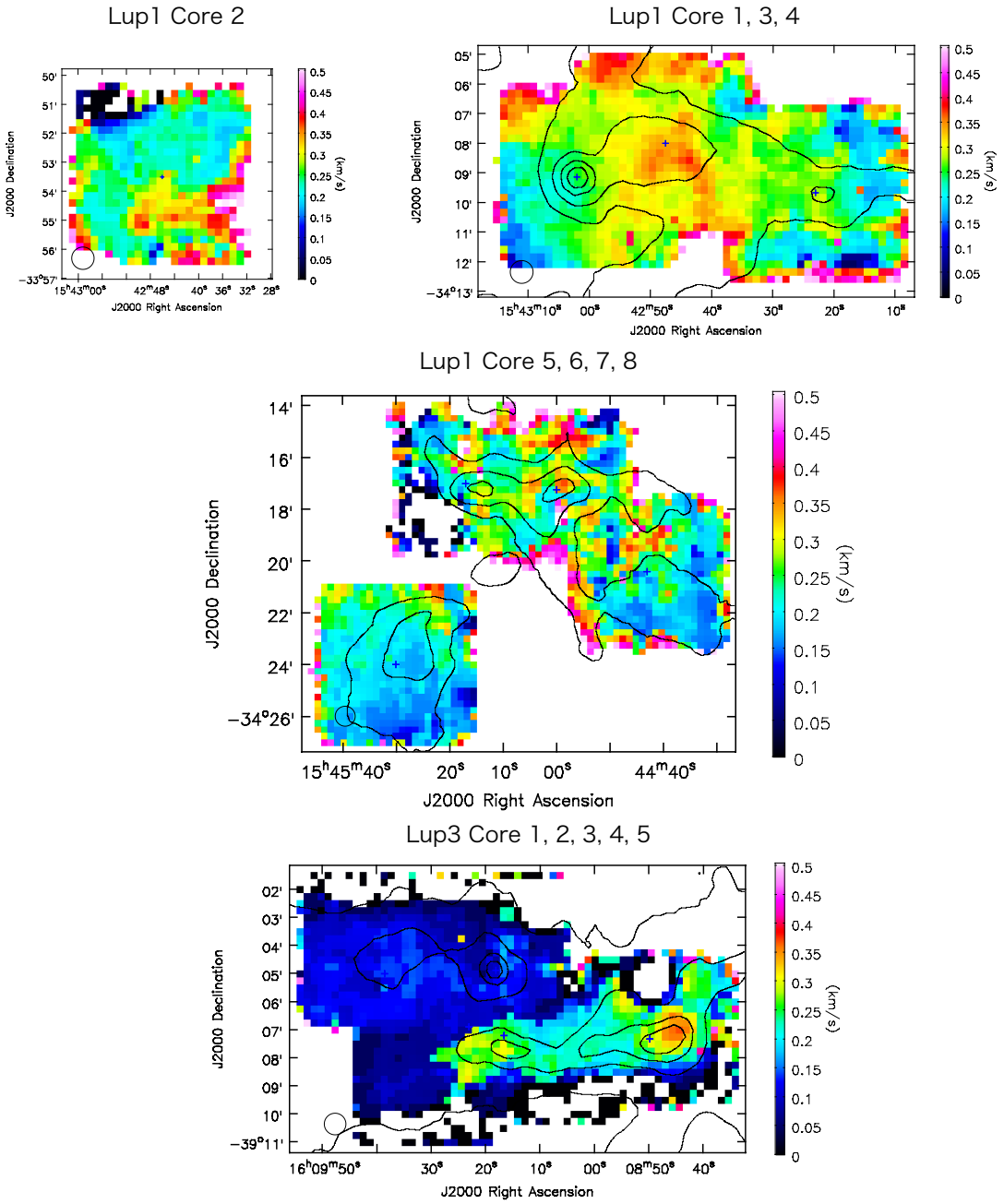

Figure 3.8: Velocity dispersion maps of $C^{18}O$(J=1–0) calculated from the second moment. Contours show the Herschel 500 μm continuum emission images.

dients in the velocity maps. Table 3.4 shows the velocity gradient fitting results. The range of the velocity gradients is 0.6-3.2 $\mathrm{km\,s^{-1}\,pc^{-1}}$. In Lup 1 C3 and C4, the velocity gradient of $C^{18}O$ is 2.5 $\mathrm{km\,s^{-1}\,pc^{-1}}$ with a P.A. of $-175°$, while the denser tracer of HC_3N shows the gradients of 1.2 and

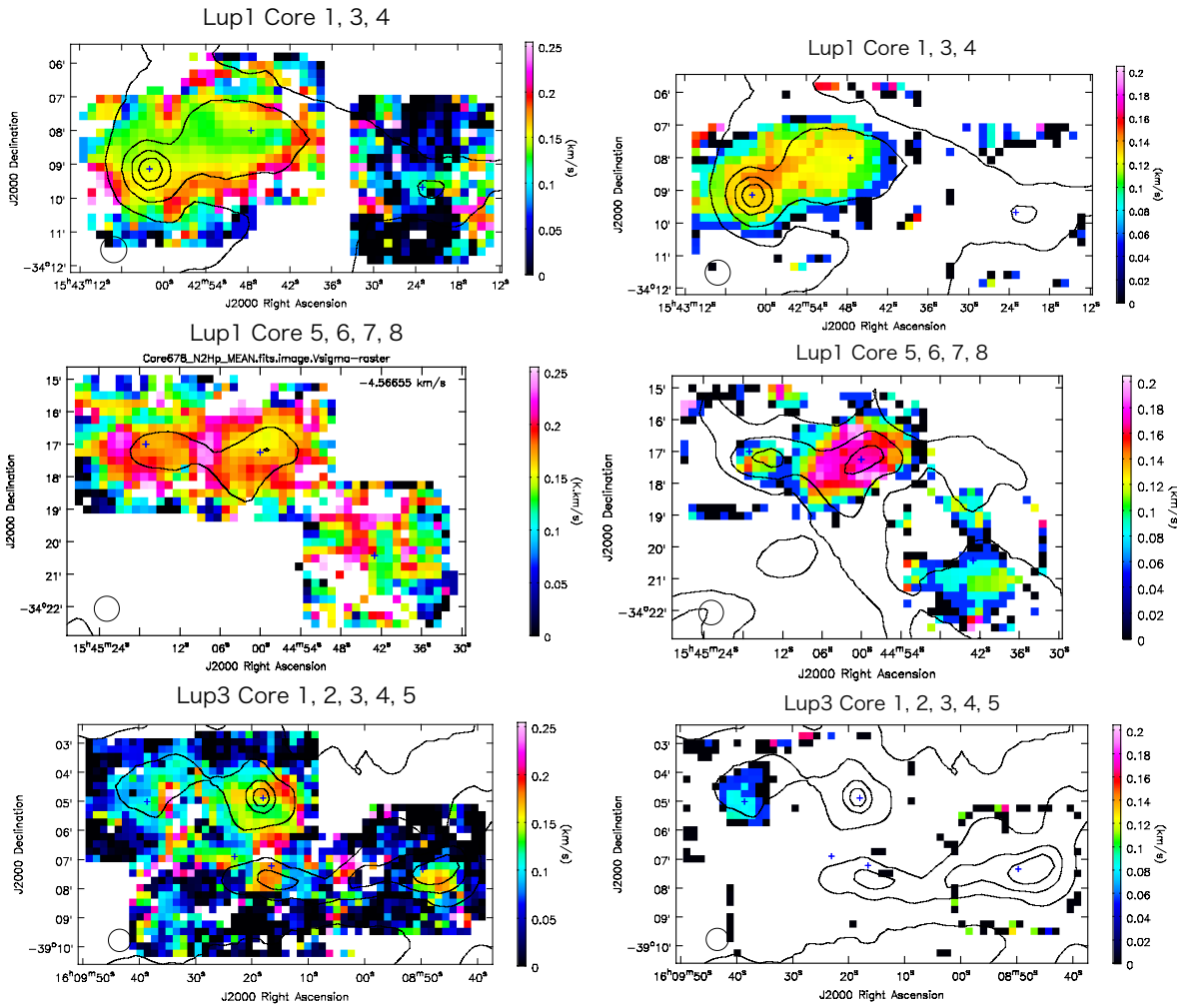

Figure 3.9: (left) Velocity dispersion maps of N_2H^+(J=1–0) produced by the HFS fitting. (right) Velocity dispersion maps of HC_3N(J=10–9) calculated from the second moment. Contours show the Herschel 500 μm continuum emission images.

1.1 $\mathrm{km\,s^{-1}\,pc^{-1}}$ with a P.A. of $-123°$ and $128°$ for Lup 1 C3 and C4, respectively. These features of HC_3N are also discerned in N_2H^+. The $C^{18}O$ emission are weak to probe the velocity field for Lup 1 C6, C7, Lup 3 C3, and C5. The denser tracer shows 2.6 $\mathrm{km\,s^{-1}\,pc^{-1}}$ with a P.A. of $-178°$ in Lup 1 C6 with HC_3N, 3.2 $\mathrm{km\,s^{-1}\,pc^{-1}}$ with a P.A. of $-166°$ in Lup 1 C7 with N_2H^+, and 1.1 $\mathrm{km\,s^{-1}\,pc^{-1}}$ with a P.A. of 139° in Lup 3 C3 with N_2H^+. Lup 3 C5 was detected with N_2H^+ and HC_3N, 3.2 $\mathrm{km\,s^{-1}\,pc^{-1}}$ with a P.A. of 156°, and 2.7 $\mathrm{km\,s^{-1}\,pc^{-1}}$ with a P.A. of 135°. N_2H^+ and HC_3N showed almast similar magnitude of the velocity gradients and the P.A. for the cores detected in both lines.

I found that deferent density tracers of $C^{18}O$ ($n_{\rm crit} \sim 10^3$ $\mathrm{cm^{-3}}$), N_2H^+ and HC_3N ($n_{\rm crit} \sim 10^5$

cm^{-3}) shows different velocity gradient in Lup 1 C3 and C4 cases. The velocity gradient of $\mathrm{C}^{18}\mathrm{O}$ would imply the large-scale motions via filament such as filament formation. Because $\mathrm{N_2H^+}$ and $\mathrm{HC_3N}$ have core-like spatial distributions and those cores are estimated to be gravitational bound by $\mathrm{N_2H^+}$, the velocity gradients are expected to indicate the rotational motions of the cores. If assuming a rigid rotation, the specific angular momentum is to be 1.1-1.2 $\times 10^{-3}\,\mathrm{km\,s^{-1}\,pc}$ at ∼0.02-0.03 pc.

It seems that the determined rotational axis of each dense core has random direction compared with the elongation of the filament. This trend is consistent with past dust continuum observations which show that the elongations of a core are not correlated with the elongation of the filament. Therefore, it is suggested that a rotational axis is independent from the elongation of filament. The rotational axis of the cores would be determined by local physical condition such as turbulence.

Table 3.4: Velocity gradient fitting results

Core	$\mathrm{C}^{18}\mathrm{O}$(1–0)		$\mathrm{N_2H^+}$(1–0)		$\mathrm{HC_3N}$(10–9)	
	$\mathrm{d}V/\mathrm{d}s$	P.A.	$\mathrm{d}V/\mathrm{d}s$	P.A.	$\mathrm{d}V/\mathrm{d}s$	P.A.
	$\mathrm{km\,s^{-1}\,pc^{-1}}$	°	$\mathrm{km\,s^{-1}\,pc^{-1}}$	°	$\mathrm{km\,s^{-1}\,pc^{-1}}$	°
Lup 1 C3	2.3 ± 0.3	-182 ± 7	0.9 ± 0.2	-116 ± 9	1.2 ± 0.2	-123 ± 7
Lup 1 C4	2.6 ± 0.2	-167 ± 4	0.9 ± 0.2	117 ± 11	1.1 ± 0.2	128 ± 9
Lup 1 C6	*	*	*	*	2.6 ± 0.3	-178 ± 6
Lup 1 C7	*	*	3.2 ± 0.23	-166 ± 4	*	*
Lup 3 C3	*	*	1.1 ± 0.2	139 ± 9	*	*
Lup 3 C5	*	*	3.2 ± 0.2	156 ± 3	2.7 ± 0.4	135 ± 8

Notes; The uncertainty represents 1 σ fitting error.
$*$: Very large uncertainty.

3.4.2 Turbulent Motions

I estimate the non-thermal velocity dispersions σ_{nth} compared with the sound speed c_{s} as following equation:

$$\left(\frac{\sigma_{\mathrm{nth}}}{c_{\mathrm{s}}}\right)^2 = \left(\frac{\Delta v}{c_{\mathrm{s}}\sqrt{8\ln 2}}\right)^2 - \left(\frac{\sigma_{\mathrm{th}}}{c_{\mathrm{s}}}\right)^2 \tag{3.1}$$

where Δv is the observed velocity width, σ_{th} is the thermal velocity dispersion given by $kT_{\mathrm{kin}}/m_{\mathrm{line}}$, and m_{line} denotes the molecular mass of observed molecules. The obtained ratios $\sigma_{\mathrm{nth}}/c_{\mathrm{s}}$ are shown

in Table 3.5. A obtained non-thermal velocity dispersion is simply considered to be caused by turbulence. The ratios of the surrounding gas traced by $C^{18}O$ are larger than unity, except for Lup 3 C5, and the ratios of the dense gas traced by N_2H^+ are less than unity. Those indicate that the dense cores are quiescent state located in the turbulent surrounding gas.

The environment in Lupus defer that in L1517, which was observed by Hacar & Tafalla (2011). They derived the ratio of $\sigma_{\rm nth}/c_{\rm s} = 0.54 \pm 0.19$ with $C^{18}O$ and $\sigma_{\rm nth}/c_{\rm s} = 0.39 \pm 0.09$ with N_2H^+ in L1517. In the Lupus 1 and the Lupus 3, the ratios are larger than the case of L1517 even in N_2H^+, indicating that the non-thermal motions of dense gas traced is affected by the turbulent surrounding gas. In contrast to L1517, Lupus 1 and Lupus 3 is suggested to be under more turbulent environment.

Table 3.5: Non-thermal velocity dispersions via the sound speed

Core	Starless/Protostar	Δv [km s^{-1}]	$\sigma_{\rm nth}/c_{\rm s}$
	$C^{18}O(1–0)$		
Lup 1 C3	Starless	0.81	1.9
Lup 1 C4	Protostar	0.60	1.4
Lup 1 C6	Starless	0.82	2.0
Lup 1 C7	Starless	0.49	1.1
Lup 3 C3	Protostar	···	···
Lup 3 C5	Starless	0.33	0.7
	$N_2H^+(1–0)$		
Lup 1 C3	Starless	0.33	0.7
Lup 1 C4	Protostar	0.35	0.8
Lup 1 C6	Starless	0.38	0.8
Lup 1 C7	Starless	0.42	1.0
Lup 3 C3	Protostar	0.42	0.9
Lup 3 C5	Starless	0.24	0.4

3.5 Summary of this chapter

I have investigated the kinematics of the dense cores in the Lupus 1 and Lupus 3 clouds using the Mopra 22 m telescope with the $C^{18}O$(J=1–0), N_2H^+(J=1–0), and $HC_3N(10–9)$ emission lines. The six dense cores of Lup 1 C3, C4, C6, C7, Lup 3 C3, and C5 have prominent spatial distributions with N_2H^+(J=1–0) or $HC_3N(10–9)$. I derived the velocity gradients of those cores. The range of the

velocity gradients is in 0.9-3.2 $\mathrm{km\,s^{-1}\,pc^{-1}}$. It seems that the determined rotational axis of the cores seems randomly directed regardless of the elongation of the filament. This trend is consistent with past dust continuum observation which shows that the elongations of a core are not correlated with the elongation of the filament. Therefore, it is suggested that the rotational axis of the cores is not correlated with the elongation of filament. The rotational axis of the cores would be determined by local physical conditions such as local magnetic directions or turbulent motions. I also found that deferent density tracers of $\mathrm{C^{18}O}$ ($n_{\mathrm{crit}} \sim 10^3$ $\mathrm{cm^{-3}}$), $\mathrm{N_2H^+}$ and $\mathrm{HC_3N}$ ($n_{\mathrm{crit}} \sim 10^5$ $\mathrm{cm^{-3}}$) show different velocity gradients in the case of Lup 1 C3 and C4. The relatively lower density tracer $\mathrm{C^{18}O}$ would show the large-scale motions in the filament and the higher density tracers of $\mathrm{N_2H^+}$ and $\mathrm{HC_3N}$ show the rotating motions within the cores.

Chapter 4

Discussion

How does a filament evolve to dense cores and stars? I raised some questions to study gas kinematics around dense cores and filaments in chapter 1 and I showed the observational results of the dense cores in the different tracers in Taurus and Lupus Molecular Clouds in chapter 2 and chapter 3. In this chapter, I will discuss three things as follows; First, I will investigate kinematics of gas around the dense cores in the different tracers and I will discuss how dense cores evolve from in a filamentary gas (§4.1). Second, I will search for a trend of the rotating axis of the dense cores with elongation of filaments (§4.2). Third, I will derive how angular momentum is distributed within a dense core (§4.3). Those topics will shed light on to the formation and evolution scenario of a low-mass dense core.

4.1 Kinematics of dense cores in a filament

Different molecular lines trace different kinematics of gas in a filament in a case because of different critical densities. Figure 4.1 shows the velocity fields of Lup 1 C3 and C4 in $C^{18}O$(J=1–0), N_2H^+(J=1–0), and HC_3N(J=10–9). The velocity field of $C^{18}O$ has a gradient along North-South, while the velocity fields of N_2H^+, and HC_3N have different gradients from $C^{18}O$; Lup 1 C4 has the velocity gradient with North-West to South-East, and Lup 1 C3 has the velocity gradient with East to West.

Here, I take the ratios between the non-thermal velocity dispersion $\sigma_{\rm nth}$ and the sound velocity $c_{\rm s}$. As a result (see §3.4.2), $\sigma_{\rm nth}/c_{\rm s}$ in $C^{18}O$ is ~ 1.6 and $\sigma_{\rm nth}/c_{\rm s}$ in N_2H^+ is ~ 0.7. Additionally considering the critical densities of $C^{18}O$, N_2H^+, and HC_3N to be 2×10^3, 1×10^5, and 5×10^5

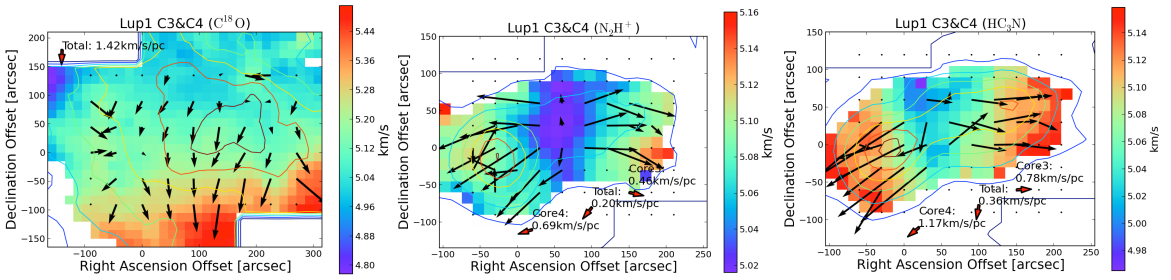

Figure 4.1: Velocity fields of $C^{18}O$(J=1–0), N_2H^+(J=1–0), and HC_3N(J=10–9) toward Lup1 C3 and C4. Notes; Those velocity maps are based on Figure 3.6 and Figure 3.7 in Chapter 3. The contours show the velocity-integrated intensity map with each line. The arrows indicated the local velocity gradient vectors.

cm^{-3}, respectively, those ratios suggest that N_2H^+ and HC_3N trace subsonic turbulent dense cores within a supersonic turbulent filament traced by $C^{18}O$.

Dense cores in filamentary regions, 1517 and L1495/B213 in Taurus are quiescent in $C^{18}O$ whose $\sigma_{\rm nth}/c_{\rm s}$ are $\sim$ 0.68 for L1517 and $\sim$ 1.0 for L1495/B213 studied by Hacar & Tafalla (2011) and Hacar et al. (2013). In these two regions, both $C^{18}O$ and N_2H^+ trace similar velocity fields in contrast to Lup 1 C3 and C4. Hacar & Tafalla (2011) investigated gas motion in a filament of L1517 and found that oscillation of the centroid velocities and densities along the filament axis with its phase difference of $\lambda/4$, where λ is the separation of dense cores. From these pieces of evidence, they proposed a fragment motion along the axis in the filament in L1517.

The velocity structures of Lup 1 C3 and C4 does not agree with the fragment motion scenario because the velocity gradients in these two cores have roughly opposite directions and because the $\lambda/4$ phase difference is not seen in the Position-Velocity diagram (Figure 4.2). One possible scenario is that turbulent motion is still dominant in the filament as seen in the second moment map of $C^{18}O$, and directions of velocity gradients of quiescent dense cores probed by N_2H^+ or HC_3N are determined by a rotating motion than a fragment motion. In that case, the rotation axes would not have any clear correlation with elongation of sub-structures in a filament or of the filament itself.

From the above results, even filaments in low-mass star forming regions show a various degree of non-thermal/turbulent motion toward dense cores traced by $C^{18}O$; turbulent in Lupus, and quiescent in L1517 and L1495/B213. I suggest that this difference produces bimodal evolutional paths (Figure 4.3); In the former case, a supersonic turbulent filament would form directly coherent dense cores, and the direction of rotational axis of dense cores is not correlated with elongation of the filaments.

In the latter case, there is an intermediate stage as velocity coherent filaments of multi-fibers from a supersonic turbulent filament to dense cores. Since the sample number is not sufficient, more dense core samples in filaments are needed to derive a general trend in dense core kinematics in a filament.

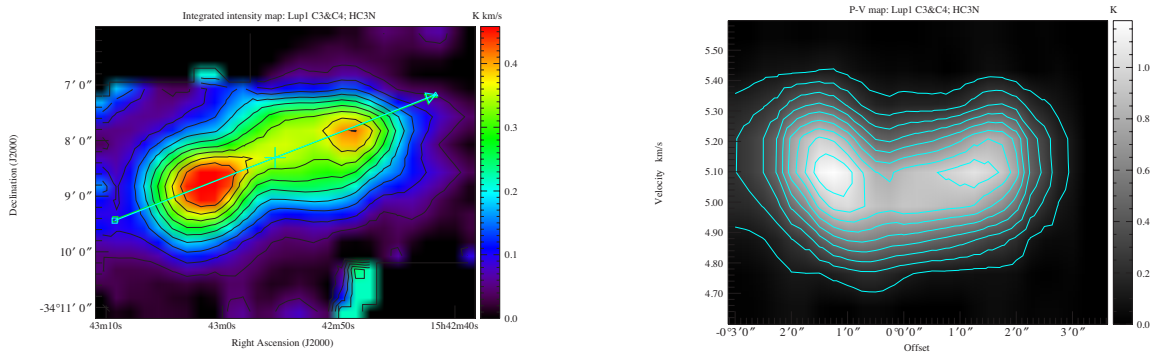

Figure 4.2: (left) The velocity-integrated intensity map of HC_3N(J=10–9) toward Lup1 C3 and C4 with an arrow indicates the cut direction of Position-Velocity diagram. (right) Position-Velocity diagram of HC_3N toward Lup1 C3 and C4.

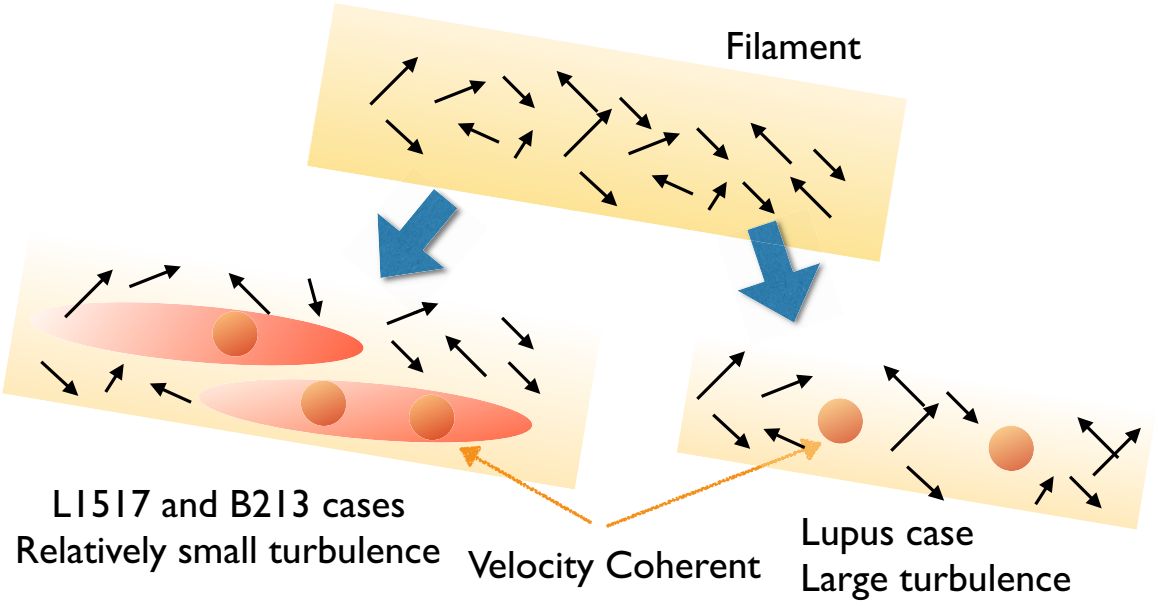

Figure 4.3: Schematic view of bimodal evolutional stages of turbulent filaments.

4.2 Rotation axis and local elongated direction of the filament

In chaper 2 and chapter 3, I derived the velocity gradients of each dense core (see Table 2.6 and Table 3.4). A rotational axis $\theta_{\rm j}$ is described as $\theta_{\rm j} = \theta_{\rm VGF} + 90^{\circ}$ whereas $\theta_{\rm VGF}$ is P.A. of the velocity gradient assuming the velocity gradient caused by rotation. The rotational axes and the locally elongated directions of the filament, which are determined by eyes, are listed in Table 4.1. Figure 4.4 shows the Herschel 500 μm images image overlaid with the rotational axes of the dense cores as arrows and the locally elongated directions as dashed lines. The differences between the rotational axis $\theta_{\rm j}$ and the locally elongated directions of the filament $\theta_{\rm filament}$ are widely ranged. This trend is consistent with past dust continuum observations which show that the elongation of a core is not correlated with the elongation of the filament (Poidevin et al., 2014). A rotational axis and elongation of the filament are expected to be correlated if an angular momentum of a parent

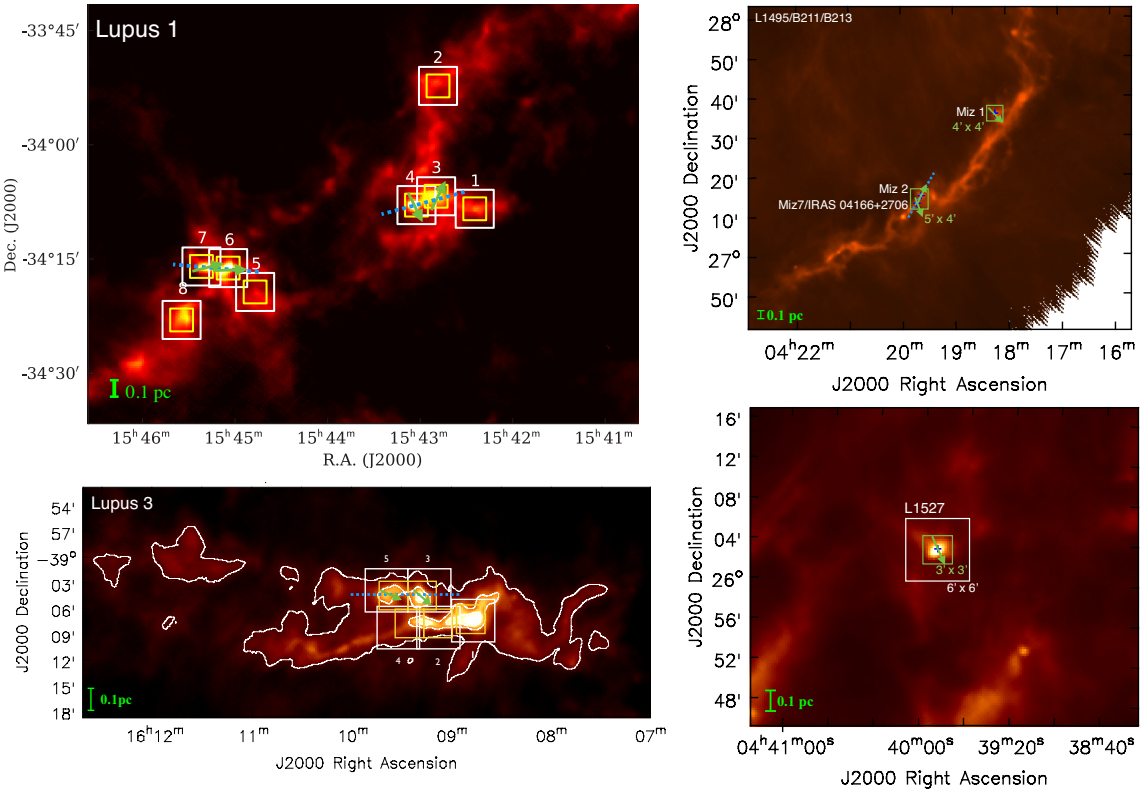

Figure 4.4: Rotational axis of the dense cores. Herschel 500 μm images overlaid with rotational axes denoted by green arrows and locally filament elongation denoted by blue-dashed lines. Boxes indicate mapping areas as same as Figure 2.1 and Figure 3.1. Core identifications are shown in Lupus 1 and Lupus 3.

core originates from a large-scale motion, while a rotational axis is randomly directed when angular momentum is determined by local physical conditions such as turbulent motions. Then, I implied that a rotational axis is not correlated from the elongation of a filament and it would be determined by local physical condition such as turbulence in spite of a small sample (Figure 4.5).

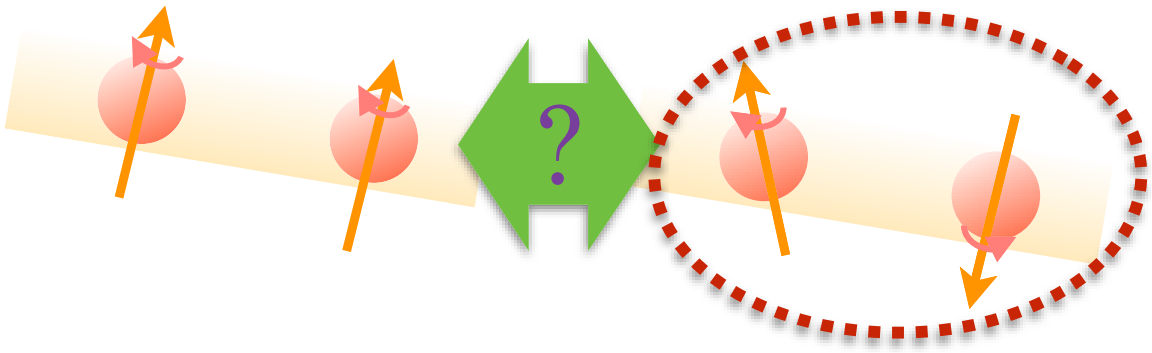

Figure 4.5: Schematic view of a rotational axis of dense cores in a filament. The observations in Lupus support the right case; the rotational axis of the dense cores is not correlated with the elongation of the filament.

4.3 Rotational axis within a core

Velocity gradients of dense cores have been investigated by several groups previously (Goodman et al., 1993; Caselli et al., 2002a; Belloche et al., 2002; Chen et al., 2007; Tobin et al., 2011). Goodman et al. (1993) performed a pioneer work in surveying dense cores in NH_3 and determined the velocity gradients of the dense cores on a scale of 0.06 - 0.6 pc. They derived the velocity gradient to be 2-5 $\mathrm{km\ s^{-1}\ pc^{-1}}$ and found a correlation between dense core size and magnitude of velocity gradients given $\mathrm{d}V/\mathrm{d}s = 10^{0.3\pm0.2} \times R^{-0.4\pm0.2}$ [$\mathrm{km\ s^{-1}\ pc^{-1}}$] (Note; where R denotes the full-width of half-maximum of core). In the present study, the obtained velocity gradient ranges from 1 to 4 $\mathrm{km\ s^{-1}\ pc^{-1}}$ agreeing with their values. These velocity gradients of dense cores are in general interpreted as rotation. First a rigid rotating core with spherical shape shows a linear velocity gradient. Second in case of protostellar cores, the gradient direction is often perpendicular to the outflow axis emanated from a protostar in the core. This is expected when a rotating core collapses yielding an accretion disk in the center where a jet/outflow blows perpendicular to the accretion disk. Observationally, Tobin et al. (2011) found that the velocity gradient and the outflow axis agrees within

Table 4.1: Rotational axes of the dense cores and locally elongated directions of the filament

Name	Rotational axis[a]	Local filament elongation[e]	
	$\theta_{\rm j}$ [°]	$\theta_{\rm filament}$[°]	$\lvert\theta_{\rm j} - \theta_{\rm filament}\rvert$[g][°]
Lupus samples			
Lup1 C3	-26 ± 9[c]	105	49
Lup1 C4	-154 ± 11[c]	105	79
Lup1 C6	-88 ± 6[d]	85	7
Lup1 C7	-76 ± 4[c]	85	19
Lup3 C3	-131 ± 9[c]	90	41
Lup3 C5	-114 ± 3[c]	90	24
Taurus samples			
L1527	-156 ± 2[b]	[f]	[f]
Miz 7	-159 ± 5[c]	150	51
Miz 2	-25 ± 3[c]	150	5
Miz 1	-137 ± 2[c]	[f]	[f]

Note;
(a): Rotational axis $\theta_{\rm j}$ determined by the direction of velocity gradient fitting $\theta_{\rm VGF}$, whose results are listed in Table 2.6 and Table 3.4 and converted to rotational axis as $\theta_{\rm j} = \theta_{\rm VGF} + 90°$. $\theta_{\rm j}$ takes the range from -180°to 180°. (b, c, d): Using the velocity gradient fitting results by the tracers of b :$C^{18}O$(1–0), c :N_2H^+(1–0), or d :HC_3N(10–9), respectively, which is best defined toward each core. (e): Locally elongated directions of the filament are determined by eyes and are shown in Figure 4.4. (f): For L1527 and Miz 1, the locally elongated direction of the filament cannot be determined. (g): The differences between rotational axis and local elongated direction of the filament, taking the range from 0°to 90°.

45 degrees in most of protostellar cores. In case of starless cores, a velocity gradient has a similar magnitude, and therefore, presumably the velocity gradient represents a rotating motion.

In the case of a dense core not in a filament, detailed study has been performed for B335, the isolated Class 0 protostar at a distance of 250 pc to compare with L1527 discussed in §2.5.2. The velocity-integrated map and the intensity-weighted averaged velocity map of B335 in $H^{13}CO^+$(1–0) are shown in Figure 4.6 that does not show a conspicuous velocity gradient. I performed a least square fitting of the velocity gradient to the first moment maps of the $H^{13}CO^+$ core in B335 and obtained the gradient to be $1.18 \pm 0.21\,{\rm km\,s^{-1}\,pc^{-1}}$ with P.A. of $18 \pm 9°$ for B335. Assuming rigid-rotation, the specific angular momentum j in B335 is 1.4 $\times 10^{-3}$ ${\rm km\,s^{-1}\,pc}$ at ${\rm r} = 0.04$ pc, which is much smallar than that in L1527 of 1.1 $\times 10^{-2}$ ${\rm km\,s^{-1}\,pc}$. For B335, Saito et al. (1999) showed

the velocity gradient to be 0.29 $\mathrm{km\,s^{-1}\,pc^{-1}}$ at 0.17 pc with $C^{18}O$ emission with P-V diagram along P.A. of 0° (perpendicular to the outflow). Kurono et al. (2013) conducted model fitting based on P-V diagram along P.A. of 0° with $H^{13}CO^+$ emission, and the results indicate the velocity gradient of 1.0 $\mathrm{km\,s^{-1}\,pc^{-1}}$ in the range of 0.01 pc to 0.1 pc. These results are comparable to the valued obtained in this thesis.

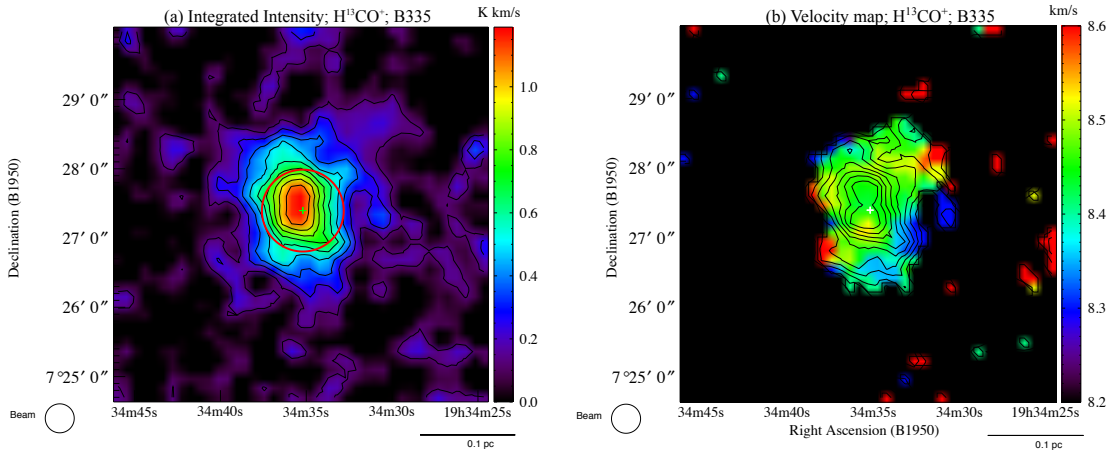

Figure 4.6: (a) The integrated intensity map and (b) the velocity map of $H^{13}CO^+$(J=1–0) in B335. The integrated velocity range of B335 is from $8.0\,\mathrm{km\,s^{-1}}$ to $9.2\,\mathrm{km\,s^{-1}}$. Red circle on the integrated intensity map denotes the core radius at $r = 0.04$ pc for B335. The contours in all figures show the 10% step levels of the integrated intensity map of each core. A cross mark indicates the IRAS source position.

Next, I applied the 2-D analysis to the B335 core (see §2.5.2 and Appendix A) and the results are shown in Figure 4.7. The direction of the rotational axes in B335 is almost constant within the core in parallel to the outflow direction and this agrees with that the dense core of B335 has a single rotational axis with rigid rotation. This result is in contrast to an interesting case found in L1527 where the rotation axis changes its direction with radius from the 2-D analysis presented in the previous section. This was also briefly pointed out by Tobin et al. (2011) in N_2H^+ observations with the IRAM 30 m telescope. The rotating axis determined from the velocity gradient of the dense core within $r = 0.03$ pc in the 2-D analysis agrees with that of the rotating disk (Ohashi et al., 2014) and the molecular outflow axis. On the other hand, the rotation axis with r $>$ 0.03 pc is different from that in the inner core. In that case, the direction of the molecular outflow and the orientation of the accretion disk in L1527 may change in the future when outer material infalls toward the center.

Indeed, there are some cases found that the outflow axis changes in morphology. Comprehensively, there are two types of angular momentum distribution about its direction (Figure 4.8): One is that the direction of rotational axes does not change from the outer to the inner part, like B335 case. The other is that the rotational axes is changing from the outer to the inner part of the core, like L1527 case.

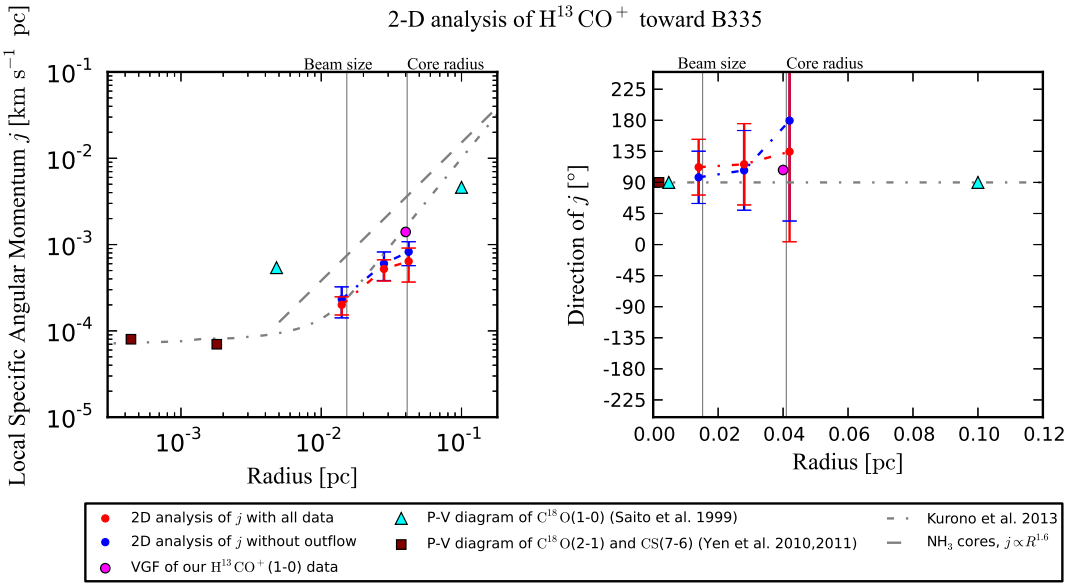

Figure 4.7: Two-dimensional specific angular momentum of the $H^{13}CO^{+}$(J=1–0) core in B335; same as Figure 2.10 for L1527, but a gray dash-dotted line shows the result of modeling by Kurono et al. (2013) and gray vertical lines show the half spatial resolution at 0.015 pc and the $H^{13}CO^{+}$ core radius of 0.041 pc.

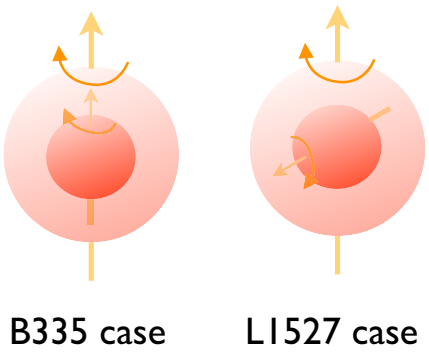

Figure 4.8: Schematic view of rotational axis within a dense core in cases of (left) B335 and (right) L1527.

Chapter 5

Conclusions

I have investigated kinematics around the dense cores in Taurus and Lupus Molecular Clouds using the NRO 45 m and the Mopra 22 m telescope in the ^{13}CO(J=1–0), C^{18}O(J=1–0), N_2H^+(J=1–0) and HC_3N(J=10–9) emission lines (chapter 2 and chapter 3).

There are four N_2H^+ dense cores in Taurus and six N_2H^+ dense cores in Lupus whose sizes, masses, and velocity widths are in the range of 0.02 - 0.05 pc, 0.27 - 0.44 km s^{-1}, and 0.9 - 1.9 $M_\odot$, respectively. Each N_2H^+ core mass is comparable to the virial mass and thus these cores are physical, not transient objects. The dense cores exhibits velocity gradients. From the fitting, I obtained the velocity gradients of these dense cores to be 0.9 - 4.7 $\mathrm{km\ s^{-1}\ pc^{-1}}$, agreeing with the low-mass dense cores in the previous study (e.g. Goodman et al., 1993). The centrifugal radius of a few to a few handred au calculated from the obtained velocity gradients corresponds to a known size of protoplanetary disks. Since a outflow axis of protostellar sources in most cases is perpendicular to the observed velocity gradient, the gradient presumably represents a rotation motion of the dense cores. For starless cores, I suppose that this also will be the case, because the derived velocity gradients are similar in magnitude to those of the protostellar cores and because the protostellar cores in the present study are at the very early phase still preserving the physical properties of starless cores.

The velocity width of C^{18}O is larger than N_2H^+ and the ratios of the non-thermal velocity dispersion $\sigma_{\rm nth}$ to the sound velocity $c_{\rm s}$ are different from region to region. For Lupus 1 and the southern filament in Lupus 3, I obtained $\sigma_{\rm nth}/c_{\rm s} \sim 1-2$ in C^{18}O and $\sigma_{\rm nth}/c_{\rm s} < 1$ in N_2H^+ (§3.4.2), suggesting that C^{18}O traces the supersonic turbulent motion around the dense cores while N_2H^+ and HC_3N trace subsonic turbulent motion within the dense cores (§4.1). On the other hand, the north-

ern filament in Lupus 3 is quiescent similar to the filaments of L1517 and L1495/B213. L1517 was suggested to experience a fragment motion along the filaments because of oscillation of densities and centroid velocities with a $\lambda/4$ phase shift found by Hacar & Tafalla (2011), where λ is the separation of dense cores. No such feature is identified in my samples and fragment motion along the filament elongation is not seen universally in low-mass star forming regions. Therefore, I suggest that there are bimodal evolutional paths with various degree of turbulence. One is that there is an intermediate stage as velocity coherent filaments of multi-fibers from a supersonic turbulent filament to dense cores, like L1517 and L1495/B213 shown by Hacar & Tafalla (2011) and Hacar et al. (2013). The other is that a supersonic turbulent filament would form directly coherent dense cores, like Lupus case in this thesis.

The rotational axis determined by the velocity gradient of each dense core is randomly directed compared with locally elongated direction of the filaments (§4.2). This trend is consistent with past dust continuum observations which show that the elongation of a core is not correlated with the elongation of the filament (Poidevin et al., 2014). A rotational axis and elongation of the filament are expected to be correlated if an angular momentum of a parent core originates from a large-scale motion, while a rotational axis is randomly directed when local physical conditions such as turbulent motions are dominant. Then, it is suggested that a rotational axis of dense cores, at least in Lupus, will be determined by local physical conditions such as turbulence.

I have performed an analysis of two-dimensional angular momentum which can derive the angular momentum magnitude and the directions as a function of radius around a protostellar core, applying to nearby isolated dense cores L1527 and B335 (§2.5.2 and §4.3). Interestingly, the direction of the rotation axis in L1527 is found to vary with scales while that in B335 is roughly constant. In both cases, the rotational axes of the most inner part are consistent with outflow/disk direction. In the case of L1527, the molecular outflow and the orientation of the accretion disk in L1527 may change in the future when the outer material infalls toward the center. Indeed, there are some cases found that the outflow axis changes in morphology, which may be explained by this mechanism. I propose that the previous methods to fit a linear velocity gradient or to use PV diagrams are not sufficient to study such complicated angular momentum structure in two dimensional space.

Appendix A

Analysis of the two-dimensional angular momentum distribution

The angular momentum and the specific angular momentum are defined as $\boldsymbol{J} \equiv \boldsymbol{r} \times \boldsymbol{p} = M\boldsymbol{r} \times \boldsymbol{v}$ and $\boldsymbol{j} \equiv \boldsymbol{J}/\mathrm{M} = \boldsymbol{r} \times \boldsymbol{v}$, respectively. Because the FITS cube data have a spatial two-dimension and a radial velocity information, the observed $\boldsymbol{r}$ and $\boldsymbol{v}$ are expressed as $\boldsymbol{r} = (x, y, 0)$ and $\boldsymbol{v} = (0, 0, V_r)$, respectively. Then, the specific angular momentum obtained by observed data is $\boldsymbol{j} \equiv (j_x, j_y, j_z) = (yV_R, -xV_R, 0) \equiv (\boldsymbol{j}_{obs}, 0)$. Based on these formula, the calculation form from FITS cube data is derived as follow. I calculate the two-dimensional angular momentum in the annular around the protostar masked outflow regions. When the subscripts i, j, k represents RA, Dec., the Velocity axis, respectively, and f_{ijk} represents the pixel value of the cube fits data,

$$\boldsymbol{j}_{obs} = \frac{\boldsymbol{J_{obs}}}{M_{obs}} = \frac{\displaystyle\sum_{i,j \in \mathrm{ring}} \begin{pmatrix} \displaystyle\sum_k f_{ijk} y V_R \\ -\displaystyle\sum_k f_{ijk} x V_R \end{pmatrix}}{\displaystyle\sum_{i,j \in \mathrm{ring}} \sum_k f_{ijk}}. \tag{A.1}$$

Using this formula, I can derive the radial distribution of direction and magnitude of the specific angular momentum vector. I tested to apply this method to the rigid-rotation with a simulation, and then the angular momentum distribution reproduces the model successfully.

Appendix B

Error Estimates for Moment maps

In this section, I present error estimates for moment maps. The formulation of error estimates for moment maps has already been shown by Furuya et al. (2014) in their appendix, but here I re-derive those formulations.

B.1 Error estimation for the integrated intensity map

The integrated intensity map over the velocity axis, called as the zeroth moment map, is defined by $I = \int T(v)dv$ and it is calculated by following equation;

$$I = \sum_{i=1}^{N} T_{\mathrm{mb},i} \Delta v_{\mathrm{ch}}, \tag{B.1}$$

with N channels in the selected velocity range over which the emission is detected. Δv_{ch} is the channel width of velocity. Considering an error propagation, the error of the integrated intensity (ΔI) is written by

$$\Delta I = \sqrt{\sum_{i=1}^{N} \left(\frac{\partial I}{\partial T_{\mathrm{mb},i}} \right)^2 (\Delta T_{\mathrm{mb},i})^2}. \tag{B.2}$$

and it is calculated as

$$\Delta I = \Delta v_{\mathrm{ch}} \sqrt{\sum_{i=1}^{N} (\Delta T_{\mathrm{mb},i})^2}. \tag{B.3}$$

If the main beam temperature ($T_{\mathrm{mb},i}$) are corrected by its opacity with each channel, its error ($\Delta T_{\mathrm{mb},i}$) depends on the velocity. When the error ($\Delta T_{\mathrm{mb},i}$) dosen't depend on the velocity channel, $\Delta T_{\mathrm{mb},i} =$

$\Delta T_{\rm mb}$, the error of the integrated intensity (ΔI) cloud be described as

$$\Delta I = \Delta T_{\rm mb} \Delta v_{\rm ch} \sqrt{N}. \tag{B.4}$$

B.2 Error estimation for the first moment map

The intensity-weighted mean velocity map, called as the first moment map, is defined by $v_{\rm 1st} = \int T(v) v dv / \int T(v) dv$ and is calculated by

$$v_{\rm 1st} = \frac{\sum_{i=1}^{N} v_i T_{{\rm mb},i} \Delta v_{\rm ch}}{\sum_{i=1}^{N} T_{{\rm mb},i} \Delta v_{\rm ch}} = \frac{\sum_{i=1}^{N} v_i T_{{\rm mb},i}}{\sum_{i=1}^{N} T_{{\rm mb},i}}. \tag{B.5}$$

Considering an error propagation, the error of the fitst moment is written by

$$\Delta v_{\rm 1st} = \sqrt{\sum_{i=1}^{N} \left(\frac{\partial v_{\rm 1st}}{\partial v_i} \right)^2 (\Delta v_i)^2 + \sum_{i=1}^{N} \left(\frac{\partial v_{\rm 1st}}{\partial T_{{\rm mb},i}} \right)^2 (\Delta T_{{\rm mb},i})^2}, \tag{B.6}$$

Δv_i is a velocity uncertainty which can be replaced by the velocity resolution ($\Delta v_{\rm res}$). The velocity resolution ($\Delta v_{\rm res}$) is usually described by FWHM ($\Delta v_{\rm res,FWHM} = \sqrt{8 \ln 2} \Delta v_{\rm res}$), and the FWHM is comparable to a channel width ($\Delta v_{\rm res,FWHM} \sim \Delta v_{\rm ch}$) (Strictly speaking, the original velocity resolution is affected by a window function of spectrometer but its effect could be neglect because the original velocity resolution is enough to fine and the final data is binned up under backend and reduction processes). Then, the error of the fitst moment is calculated by

$$\begin{aligned}
\Delta v_{\rm 1st} &= \sqrt{\sum_{i=1}^{N} \left(\frac{T_{{\rm mb},i}}{I} \right)^2 (\Delta v_{\rm res})^2 (\Delta v_{\rm ch})^2 + \sum_{i=1}^{N} \left(\frac{v_i - v_{\rm 1st}}{I} \right)^2 (\Delta T_{{\rm mb},i})^2 (\Delta v_{\rm ch})^2} \\
&= \frac{\Delta v_{\rm ch}}{I} \sqrt{(\Delta v_{\rm res})^2 \sum_{i=1}^{N} (T_{{\rm mb},i})^2 + \sum_{i=1}^{N} (v_i - v_{\rm 1st})^2 (\Delta T_{{\rm mb},i})^2} \\
&= \frac{\Delta v_{\rm ch}}{I} \sqrt{\frac{{\Delta v_{\rm ch}}^2}{8 \ln 2} \sum_{i=1}^{N} (T_{{\rm mb},i})^2 + \sum_{i=1}^{N} (v_i - v_{\rm 1st})^2 (\Delta T_{{\rm mb},i})^2}.
\end{aligned} \tag{B.7}$$

When the error of the main beam temperature ($\Delta T_{\mathrm{mb},i}$) dosen't depend on the velocity channel, $\Delta T_{\mathrm{mb},i} = \Delta T_{\mathrm{mb}}$, the error of the first moment (Δv_{1st}) cloud be described as

$$\begin{aligned} \Delta v_{\mathrm{1st}} &= \frac{\Delta T_{\mathrm{mb}} \Delta v_{\mathrm{ch}}{}^2}{I} \sqrt{\frac{1}{8\ln 2}\sum_{i=1}^{N}\left(\frac{T_{\mathrm{mb},i}}{\Delta T_{\mathrm{mb}}}\right)^2 + \sum_{i=1}^{N}\left(\frac{v_i - v_{\mathrm{1st}}}{\Delta v_{\mathrm{ch}}}\right)^2} \\ &= \frac{\Delta I \Delta v_{\mathrm{ch}}}{I\sqrt{N}} \sqrt{\frac{1}{8\ln 2}\sum_{i=1}^{N}\left(\frac{T_{\mathrm{mb},i}}{\Delta T_{\mathrm{mb}}}\right)^2 + \sum_{i=1}^{N}\left(\frac{v_i - v_{\mathrm{1st}}}{\Delta v_{\mathrm{ch}}}\right)^2}. \end{aligned} \tag{B.8}$$

Equation (2.3) in Belloche 2013 corresponds to a case of only considering the second term in the square root in eq. (B.8). In other words, they neglect the first term in the square root in eq. (B.8). But if based the definition (eq. (B.6)), the first term is needed and Furuya+2014 is also considering the term (eq. B5 adn eq. B6 in their paper). In this thesis, I calculated the error of the first moment based on eq. (B.7) and eq. (B.8).

B.3 Error estimation for the second moment map

The intensity-weighted velocity dispersion, called as the second moment map, is defined by $\sigma = \sqrt{\int T(v)(v - v_{\mathrm{1st}})^2 dv / \int T(v) dv}$ and is calculated by

$$\sigma = \sqrt{\frac{\sum_{i=1}^{N}(v_i - v_{\mathrm{1st}})^2 T_{\mathrm{mb},i}\Delta v}{\sum_{i=1}^{N} T_{\mathrm{mb},i}\Delta v}} = \sqrt{\frac{\sum_{i=1}^{N}(v_i - v_{\mathrm{1st}})^2 T_{\mathrm{mb},i}}{\sum_{i=1}^{N} T_{\mathrm{mb},i}}}. \tag{B.9}$$

Considering an error propagation, the error of the second moment is written by

$$\Delta\sigma = \sqrt{\sum_{i=1}^{N}\left(\frac{\partial\sigma}{\partial v_i}\right)^2 (\Delta v_i)^2 + \sum_{i=1}^{N}\left(\frac{\partial\sigma}{\partial T_{\mathrm{mb},i}}\right)^2 (\Delta T_{\mathrm{mb},i})^2}. \tag{B.10}$$

Here, I set some characters as follow;

$$\sigma = \sqrt{\frac{\sum_{i=1}^{N}(v_i - v_{\mathrm{1st}})^2 T_{\mathrm{mb},i}}{\sum_{i=1}^{N} T_{\mathrm{mb},i}}} = \sqrt{\frac{h}{g}} = \sqrt{f}. \tag{B.11}$$

In the begin with considering the first term in the square root of eq. (B.10), it is described as

$$\begin{aligned}
\frac{\partial \sigma}{\partial v_i} &= \frac{\partial}{\partial v_i}\sqrt{f} = \frac{1}{2}\frac{1}{\sqrt{f}}\frac{\partial f}{\partial v_i} = \frac{1}{2\sigma}\frac{\partial f}{\partial v_i} \\
&= \frac{1}{2\sigma}\frac{\partial}{\partial v_i}\left(\frac{h}{g}\right) = \frac{1}{2\sigma}\left(\frac{1}{g}\frac{\partial h}{\partial v_i} - \frac{h}{g^2}\frac{\partial g}{\partial v_i}\right) = \frac{1}{2\sigma}\left(\frac{1}{g}\frac{\partial h}{\partial v_i} - \frac{\sigma^2}{g}\frac{\partial g}{\partial v_i}\right) \\
&= \frac{1}{2\sigma}\left(\frac{\Delta v_{\mathrm{ch}}}{I}\frac{\partial h}{\partial v_i} - \frac{\sigma^2 \Delta v_{\mathrm{ch}}}{I}\frac{\partial g}{\partial v_i}\right) \\
&= \frac{\Delta v_{\mathrm{ch}}}{2\sigma I}\frac{\partial h}{\partial v_i} - \frac{\sigma \Delta v_{\mathrm{ch}}}{2I}\frac{\partial g}{\partial v_i} \qquad \text{(B.12)}
\end{aligned}$$

Here, $\frac{\partial h}{\partial v_i}$ and $\frac{\partial g}{\partial v_i}$ are written by

$$\begin{aligned}
\frac{\partial h}{\partial v_i} &= \frac{\partial}{\partial v_i}\left(\sum_{j=1}^{N}(v_j - v_{1\mathrm{st}})^2 T_{\mathrm{mb},j}\right) \\
&= 2T_{\mathrm{mb},i}(v_i - v_{1\mathrm{st}}) - 2\left(\frac{\partial v_{1\mathrm{st}}}{\partial v_i}\right)\sum_{j=1}^{N} T_{\mathrm{mb},j}(v_j - v_{1\mathrm{st}}) \\
&= 2T_{\mathrm{mb},i}(v_i - v_{1\mathrm{st}}) \quad [\because \text{eq.(B.15)}] \qquad \text{(B.13)} \\
\frac{\partial g}{\partial v_i} &= \frac{\partial}{\partial v_i}\sum_{j=1}^{N} T_{\mathrm{mb},j} = 0 \qquad \text{(B.14)}
\end{aligned}$$

$$\begin{aligned}
\sum_{j=1}^{N} T_{\mathrm{mb},j}(v_j - v_{1\mathrm{st}}) &= \sum_{j=1}^{N} T_{\mathrm{mb},j} v_j - v_{1\mathrm{st}}\sum_{j=1}^{N} T_{\mathrm{mb},j} \\
&= \sum_{j=1}^{N} T_{\mathrm{mb},j} v_j - \frac{\sum_{k=1}^{N} T_{\mathrm{mb},k} v_k}{\sum_{k=1}^{N} T_{\mathrm{mb},k}}\sum_{j=1}^{N} T_{\mathrm{mb},j} \\
&= \sum_{j=1}^{N} T_{\mathrm{mb},j} v_j - \sum_{k=1}^{N} T_{\mathrm{mb},k} v_k = 0 \qquad \text{(B.15)}
\end{aligned}$$

Then, the first term in the square root of eq. (B.10) is represented as

$$\begin{aligned}\sum_{i=1}^{N}\left(\frac{\partial\sigma}{\partial v_i}\right)^2(\Delta v_i)^2 &= (\Delta v_{\rm res})^2\sum_{i=1}^{N}\left(\frac{\partial\sigma}{\partial v_i}\right)^2 \\ &= (\Delta v_{\rm res})^2\sum_{i=1}^{N}\left(\frac{T_{{\rm mb},i}\Delta v_{\rm ch}}{\sigma I}(v_i-v_{\rm 1st})\right)^2 \\ &= \frac{\Delta v_{\rm res}^2\Delta v_{\rm ch}^2}{\sigma^2 I^2}\sum_{i=1}^{N}(T_{{\rm mb},i}(v_i-v_{\rm 1st}))^2. \end{aligned} \tag{B.16}$$

Next, the second term in the square root of eq. (B.10),

$$\sum_{i=1}^{N}\left(\frac{\partial\sigma}{\partial T_{{\rm mb},i}}\right)^2(\Delta T_{{\rm mb},i})^2,$$

is considered. In the same way of eq. (B.12),

$$\frac{\partial\sigma}{\partial T_{{\rm mb},i}} = \frac{\Delta v_{\rm ch}}{2\sigma I}\frac{\partial h}{\partial T_{{\rm mb},i}} - \frac{\sigma\Delta v_{\rm ch}}{2I}\frac{\partial g}{\partial T_{{\rm mb},i}} \tag{B.17}$$

Here, $\frac{\partial h}{\partial T_{{\rm mb},i}}$ and $\frac{\partial g}{\partial T_{{\rm mb},i}}$ are written by

$$\begin{aligned}\frac{\partial h}{\partial T_{{\rm mb},i}} &= \frac{\partial}{\partial T_{{\rm mb},i}}\left(\sum_{j=1}^{N}(v_j-v_{\rm 1st})^2T_{{\rm mb},j}\right) \\ &= (v_j-v_{\rm 1st})^2 - 2\left(\frac{\partial v_{\rm 1st}}{\partial T_{{\rm mb},i}}\right)\sum_{j=1}^{N}T_{{\rm mb},j}(v_j-v_{\rm 1st}) \\ &= (v_j-v_{\rm 1st})^2 \quad [\because \text{eq.(B.15)}] \end{aligned} \tag{B.18}$$

$$\frac{\partial g}{\partial T_{{\rm mb},i}} = \frac{\partial}{\partial T_{{\rm mb},i}}\sum_{j=1}^{N}T_{{\rm mb},j} = 1 \tag{B.19}$$

Then, the second term in the square root of eq. (B.10) is described as

$$\begin{aligned}
\sum_{i=1}^{N}\left(\frac{\partial\sigma}{\partial T_{\mathrm{mb},i}}\right)^2(\Delta T_{\mathrm{mb},i})^2 &= \sum_{i=1}^{N}\left(\frac{\Delta v_{\mathrm{ch}}}{2\sigma I}(v_j-v_{\mathrm{1st}})^2-\frac{\sigma\Delta v_{\mathrm{ch}}}{2I}\right)^2(\Delta T_{\mathrm{mb},i})^2 \\
&= \sum_{i=1}^{N}\left(\frac{\Delta v_{\mathrm{ch}}}{2\sigma I}\left((v_j-v_{\mathrm{1st}})^2-\sigma^2\right)\right)^2(\Delta T_{\mathrm{mb},i})^2 \\
&= \frac{\Delta v_{\mathrm{ch}}^2}{4\sigma^2 I^2}\sum_{i=1}^{N}\left((v_j-v_{\mathrm{1st}})^2-\sigma^2\right)^2(\Delta T_{\mathrm{mb},i})^2 \qquad \text{(B.20)}
\end{aligned}$$

Therefore, the error of the intensity-weighted velocity dispersion (eq. B.10) is described as

$$\begin{aligned}
\Delta\sigma &= \sqrt{\frac{\Delta v_{\mathrm{res}}^2\Delta v_{\mathrm{ch}}^2}{\sigma^2 I^2}\sum_{i=1}^{N}(T_{\mathrm{mb},i}(v_i-v_{\mathrm{1st}}))^2+\frac{\Delta v_{\mathrm{ch}}^2}{4\sigma^2 I^2}\sum_{i=1}^{N}\left((v_j-v_{\mathrm{1st}})^2-\sigma^2\right)^2(\Delta T_{\mathrm{mb},i})^2} \\
&= \frac{\Delta v_{\mathrm{ch}}}{\sigma I}\sqrt{\Delta v_{\mathrm{res}}^2\sum_{i=1}^{N}(T_{\mathrm{mb},i}(v_i-v_{\mathrm{1st}}))^2+\frac{1}{4}\sum_{i=1}^{N}\left((v_j-v_{\mathrm{1st}})^2-\sigma^2\right)^2(\Delta T_{\mathrm{mb},i})^2} \\
&= \frac{\Delta v_{\mathrm{ch}}}{\sigma I}\sqrt{\left(\frac{\Delta v_{\mathrm{ch}}}{\sqrt{8\ln 2}}\right)^2\sum_{i=1}^{N}(T_{\mathrm{mb},i}(v_i-v_{\mathrm{1st}}))^2+\frac{1}{4}\sum_{i=1}^{N}\left((v_j-v_{\mathrm{1st}})^2-\sigma^2\right)^2(\Delta T_{\mathrm{mb},i})^2} \\
&= \frac{{\Delta v_{\mathrm{ch}}}^2}{\sigma I}\sqrt{\frac{1}{8\ln 2}\sum_{i=1}^{N}(T_{\mathrm{mb},i}(v_i-v_{\mathrm{1st}}))^2+\frac{1}{4}\sum_{i=1}^{N}\left(\frac{(v_j-v_{\mathrm{1st}})^2-\sigma^2}{\Delta v_{\mathrm{ch}}}\right)^2(\Delta T_{\mathrm{mb},i})^2}.
\end{aligned} \qquad \text{(B.21)}$$

When $\Delta T_{\mathrm{mb},i}=\Delta T_{\mathrm{mb}}$,

$$\begin{aligned}
\Delta\sigma &= \frac{\Delta T_{\mathrm{mb}}{\Delta v_{\mathrm{ch}}}^2}{\sigma I}\sqrt{\frac{1}{8\ln 2}\sum_{i=1}^{N}\left(\frac{T_{\mathrm{mb},i}(v_i-v_{\mathrm{1st}})}{\Delta T_{\mathrm{mb}}}\right)^2+\frac{1}{4}\sum_{i=1}^{N}\left(\frac{(v_j-v_{\mathrm{1st}})^2-\sigma^2}{\Delta v_{\mathrm{ch}}}\right)^2} \\
&= \frac{\Delta I\Delta v_{\mathrm{ch}}^2}{I\sigma}\sqrt{\frac{1}{8\ln 2}\sum_{i=1}^{N}\left(\frac{T_{\mathrm{mb},i}(v_i-v_{\mathrm{1st}})}{\Delta T_{\mathrm{mb}}\Delta v_{\mathrm{ch}}}\right)^2+\frac{1}{4}\sum_{i=1}^{N}\left(\frac{(v_j-v_{\mathrm{1st}})^2-\sigma^2}{\Delta v_{\mathrm{ch}}^2}\right)^2}.
\end{aligned} \qquad \text{(B.22)}$$

Appendix C

Channel maps of all data

In this section, I show the channel maps pf all data.

Channel map of ^{13}CO(J=1–0) in L1527

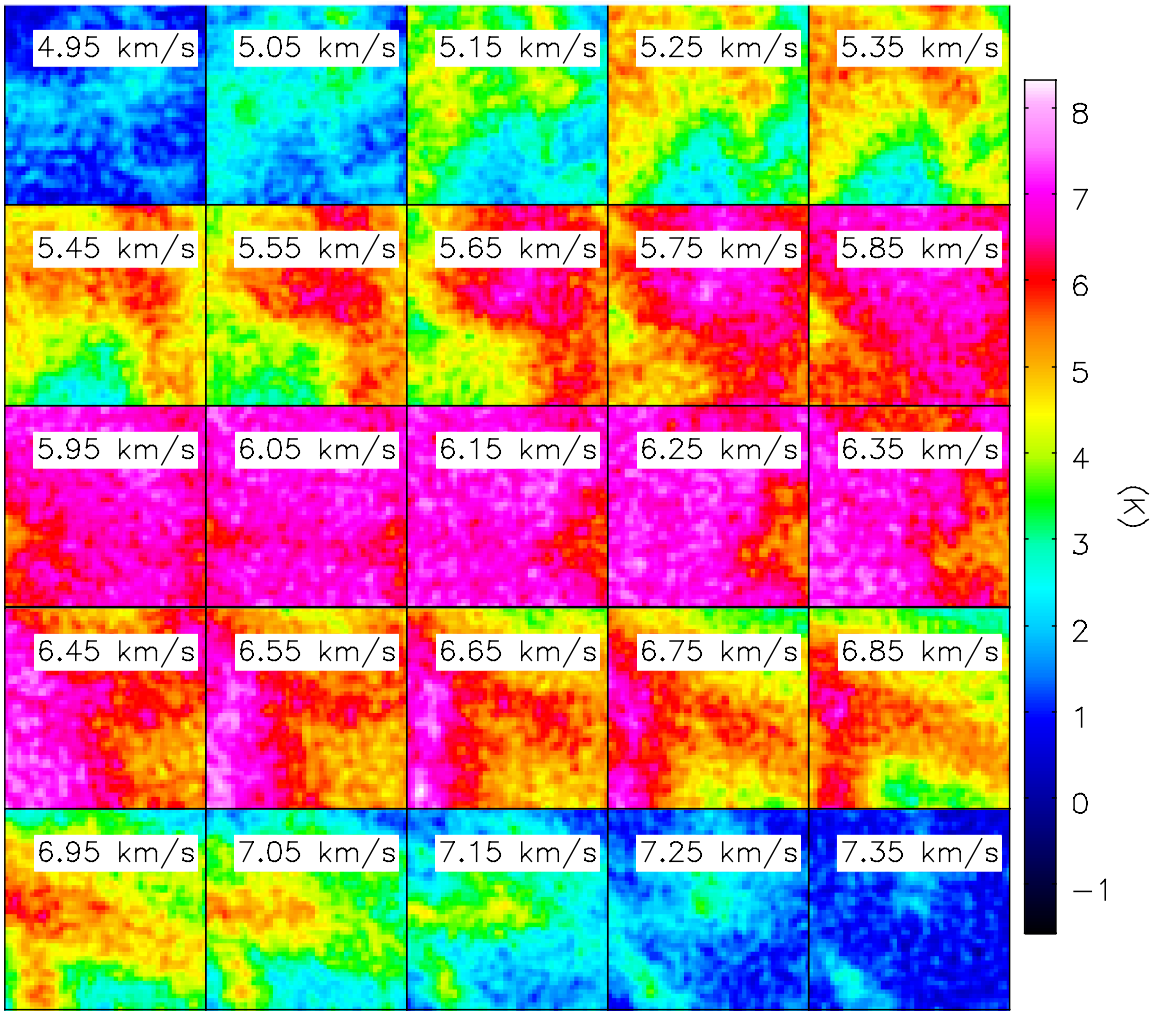

Figure C.1: Channel map of ^{13}CO(J=1–0) in L1527

Channel map of $C^{18}O$(J=1–0) in L1527

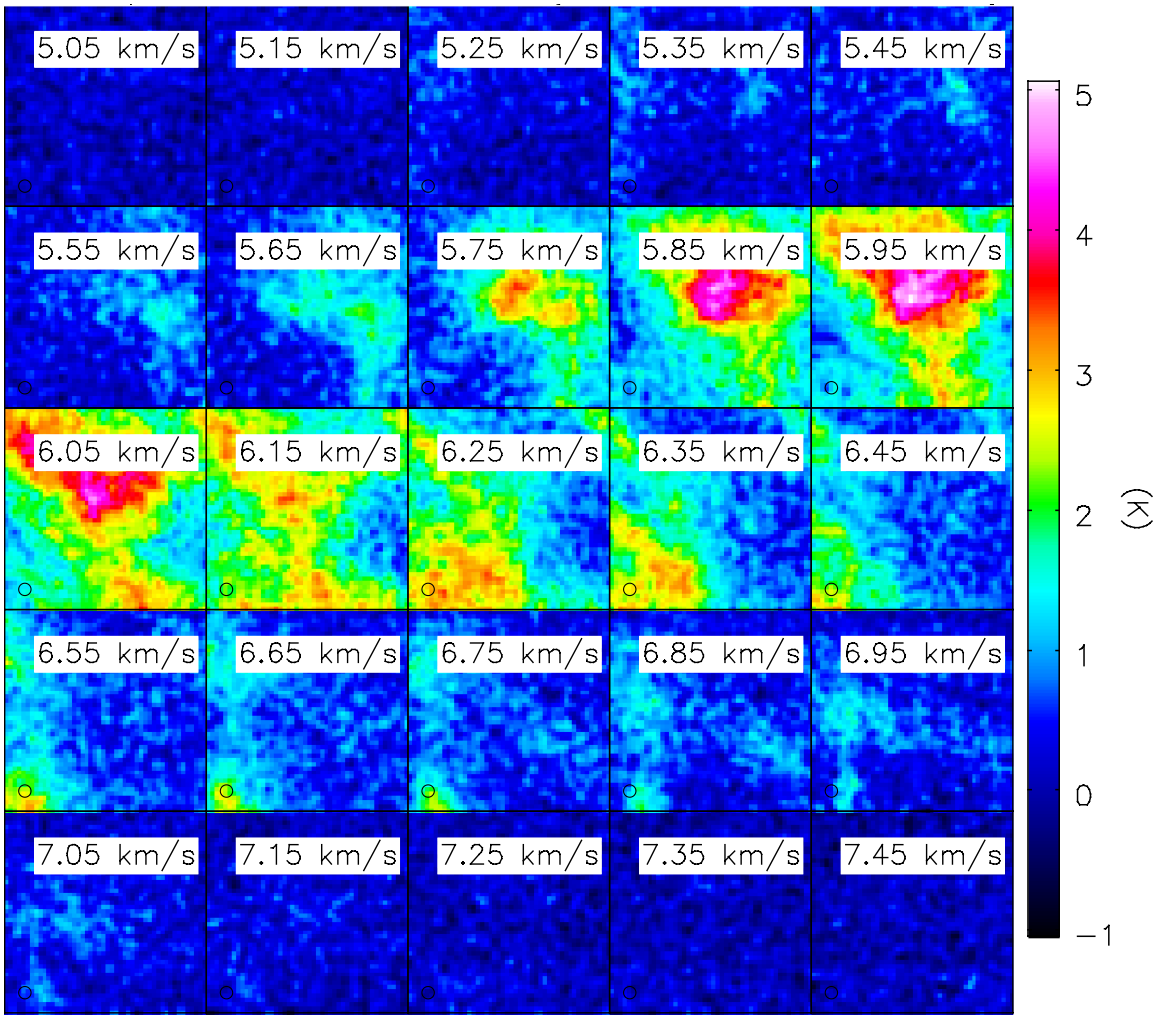

Figure C.2: Channel map of $C^{18}O$(J=1–0) in L1527

Channel map of N_2H^+(J=1–0) in L1527

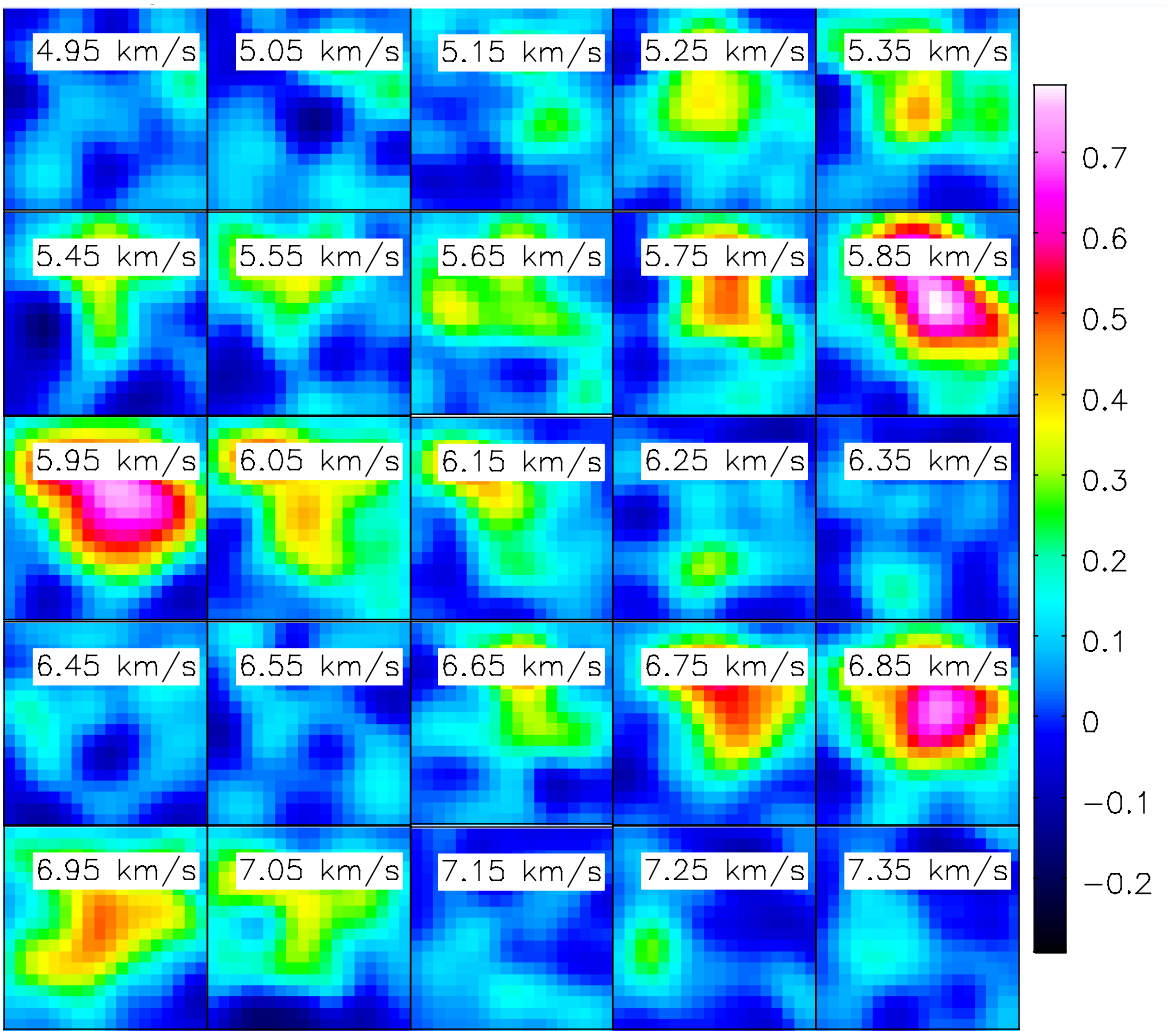

Figure C.3: Channel map of N_2H^+(J=1–0) in L1527

Channel map of HC_3N(J=10–9) in L1527

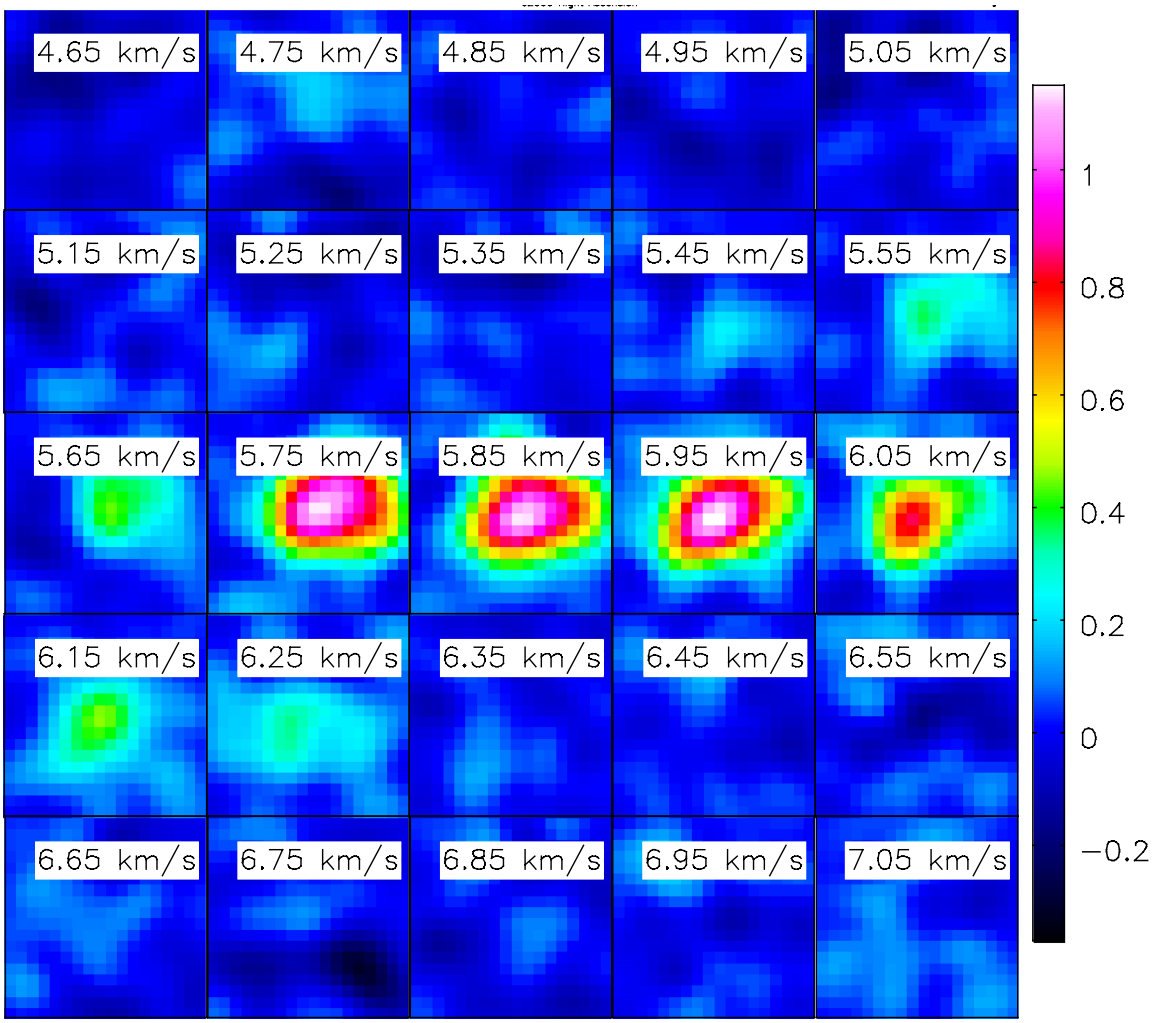

Figure C.4: Channel map of HC_3N(J=10–9) in L1527

Channel map of N_2H^+(J=1–0) in Miz 7

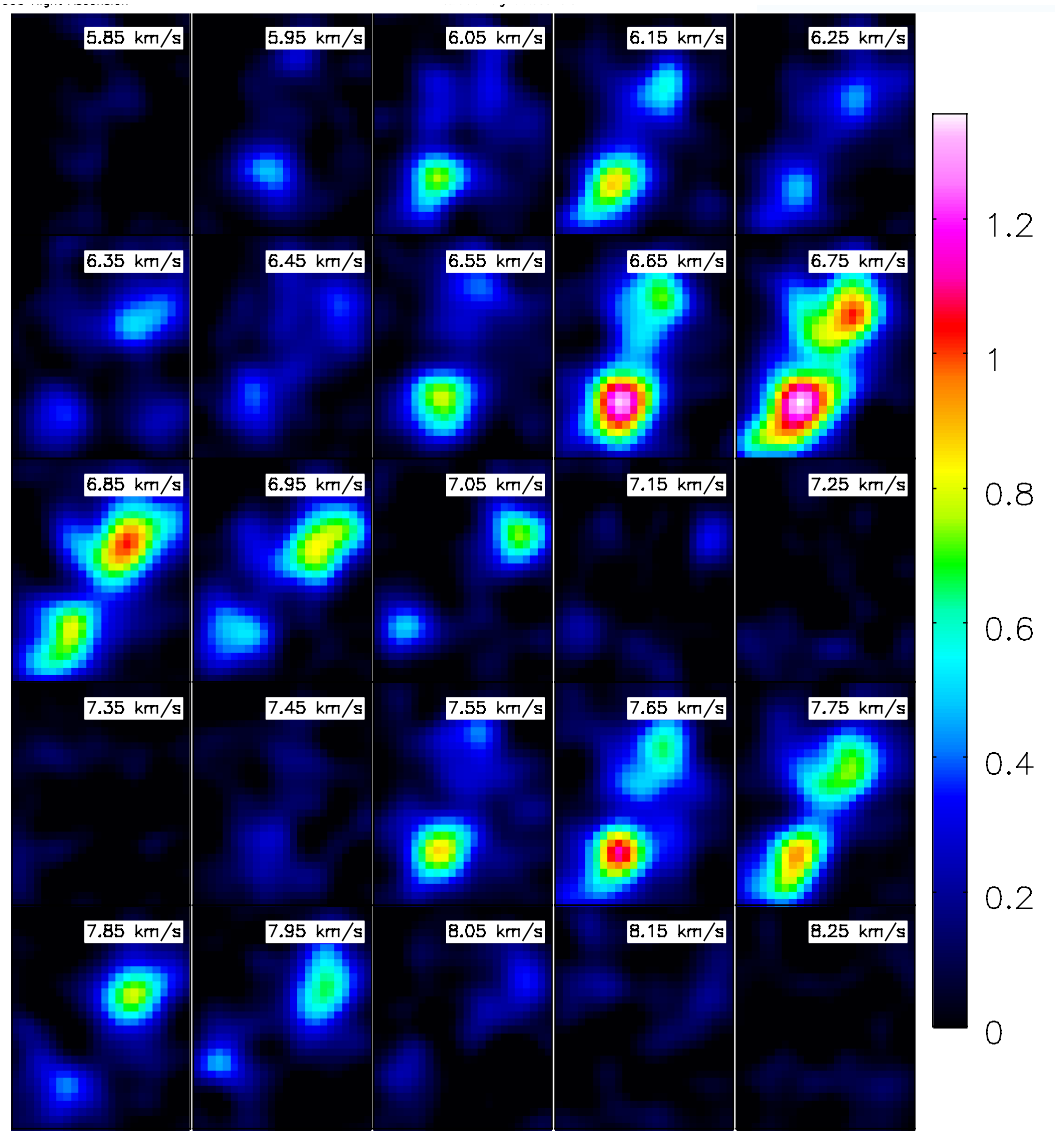

Figure C.5: Channel map of N_2H^+(J=1–0) in Miz 7

Channel map of HC_3N(J=10–9) in Miz 7

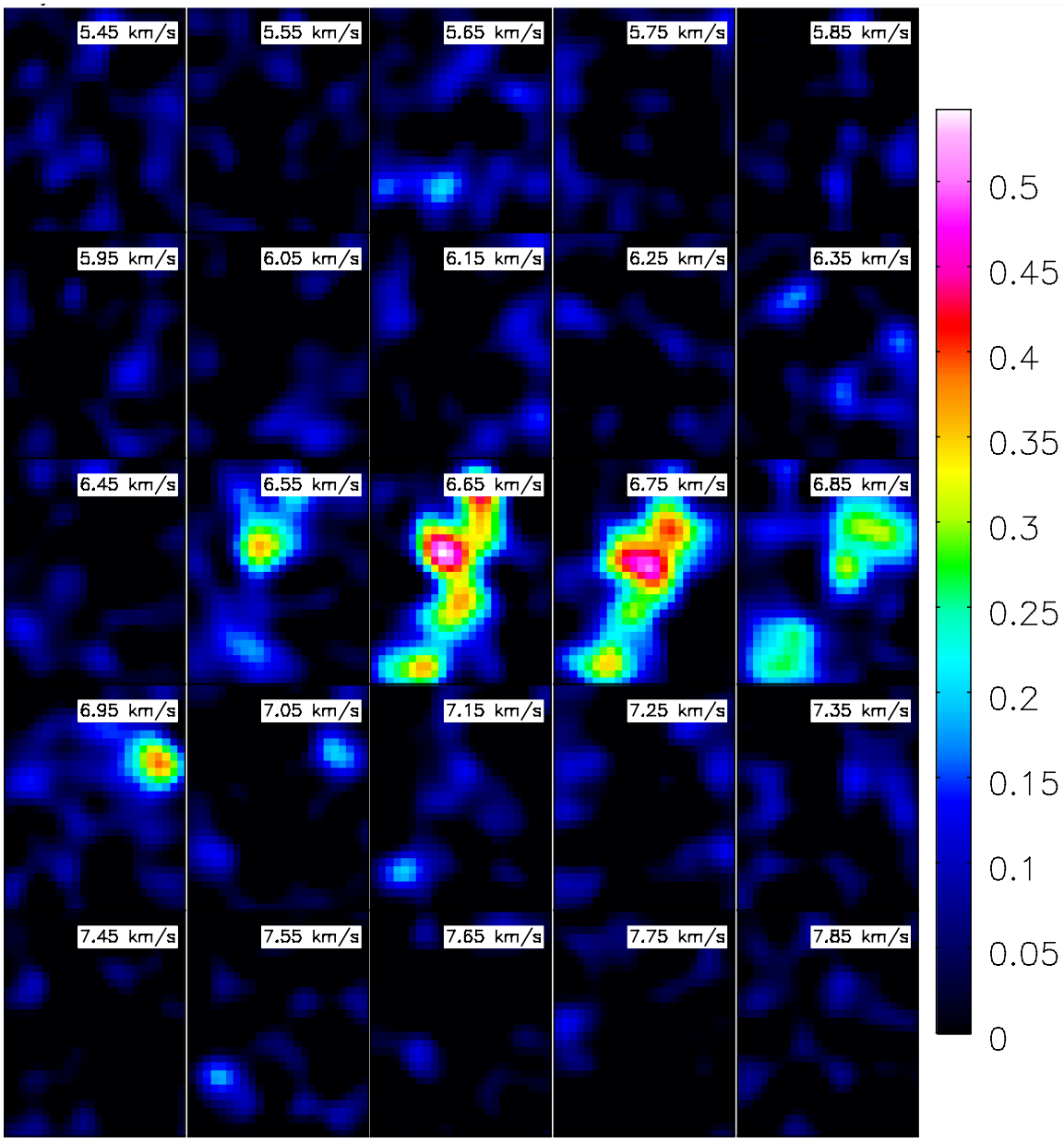

Figure C.6: Channel map of HC_3N(J=10–9) in Miz 7

Channel map of N_2H^+(J=1–0) in Miz1

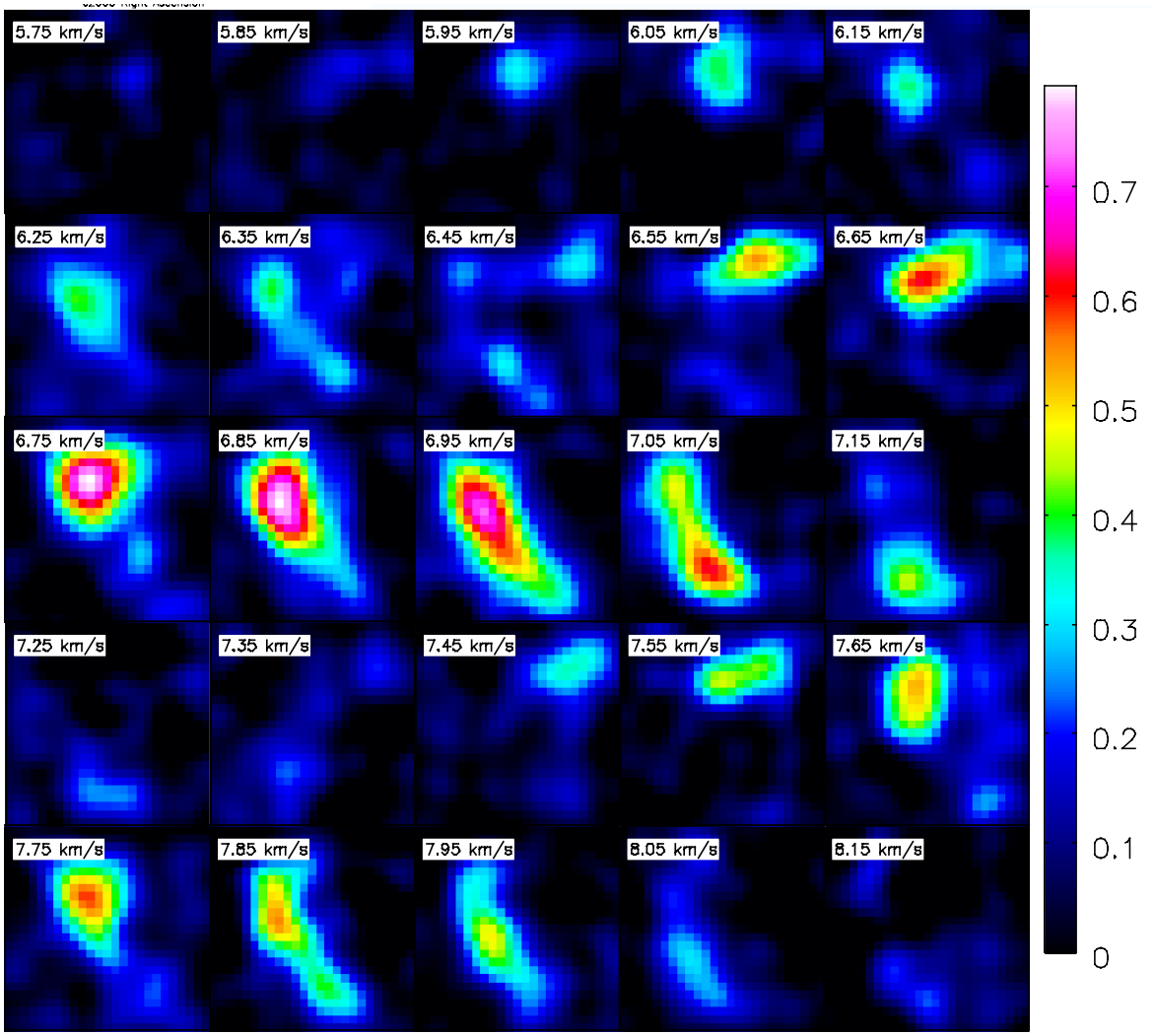

Figure C.7: Channel map of N_2H^+(J=1–0) in Miz1

Channel map of HC_3N(J=10–9) in Miz1

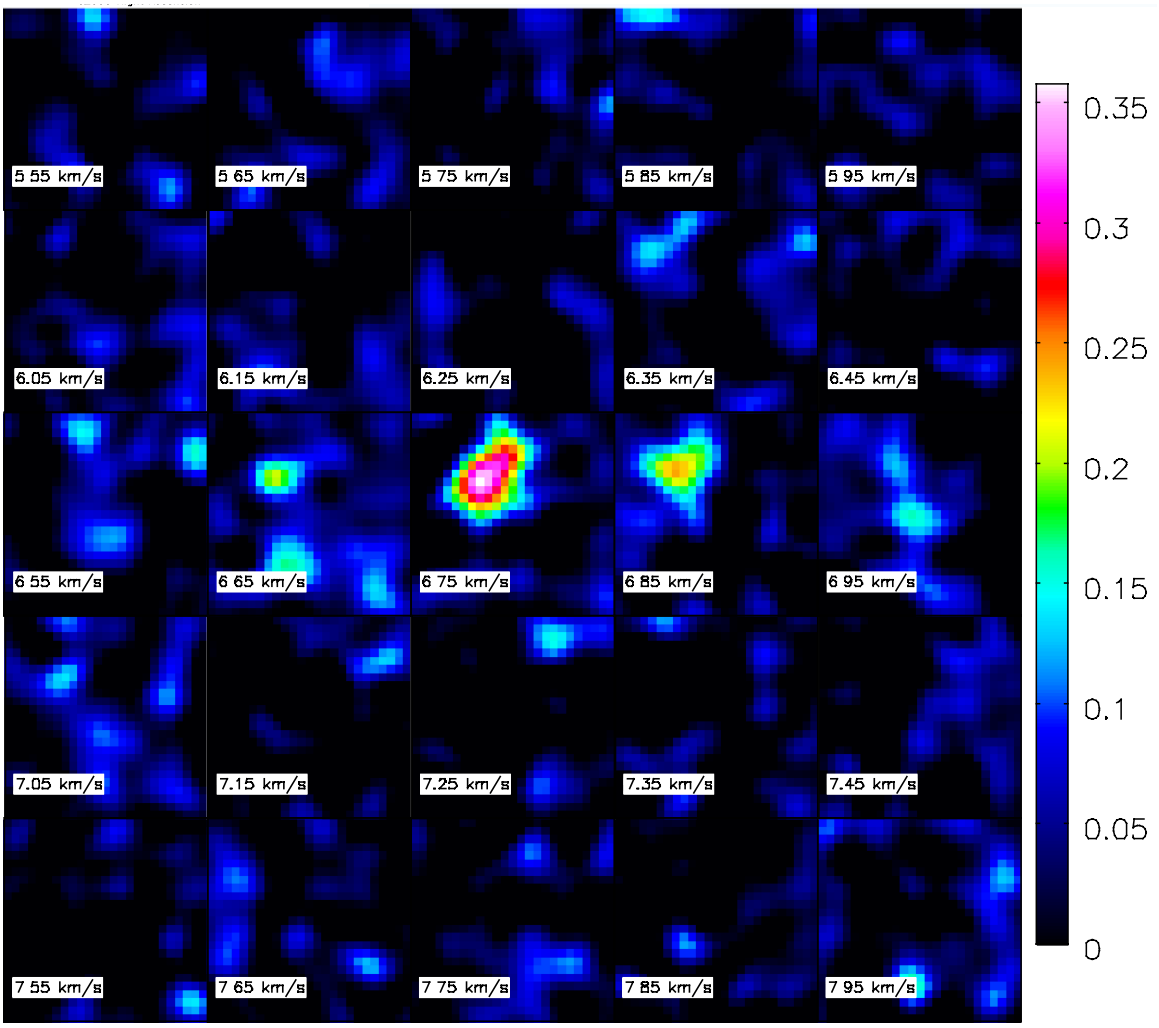

Figure C.8: Channel map of HC_3N(J=10–9) in Miz1

Channel map of $C^{18}O$(J=1–0) in Lup1 C1, C3, and C4

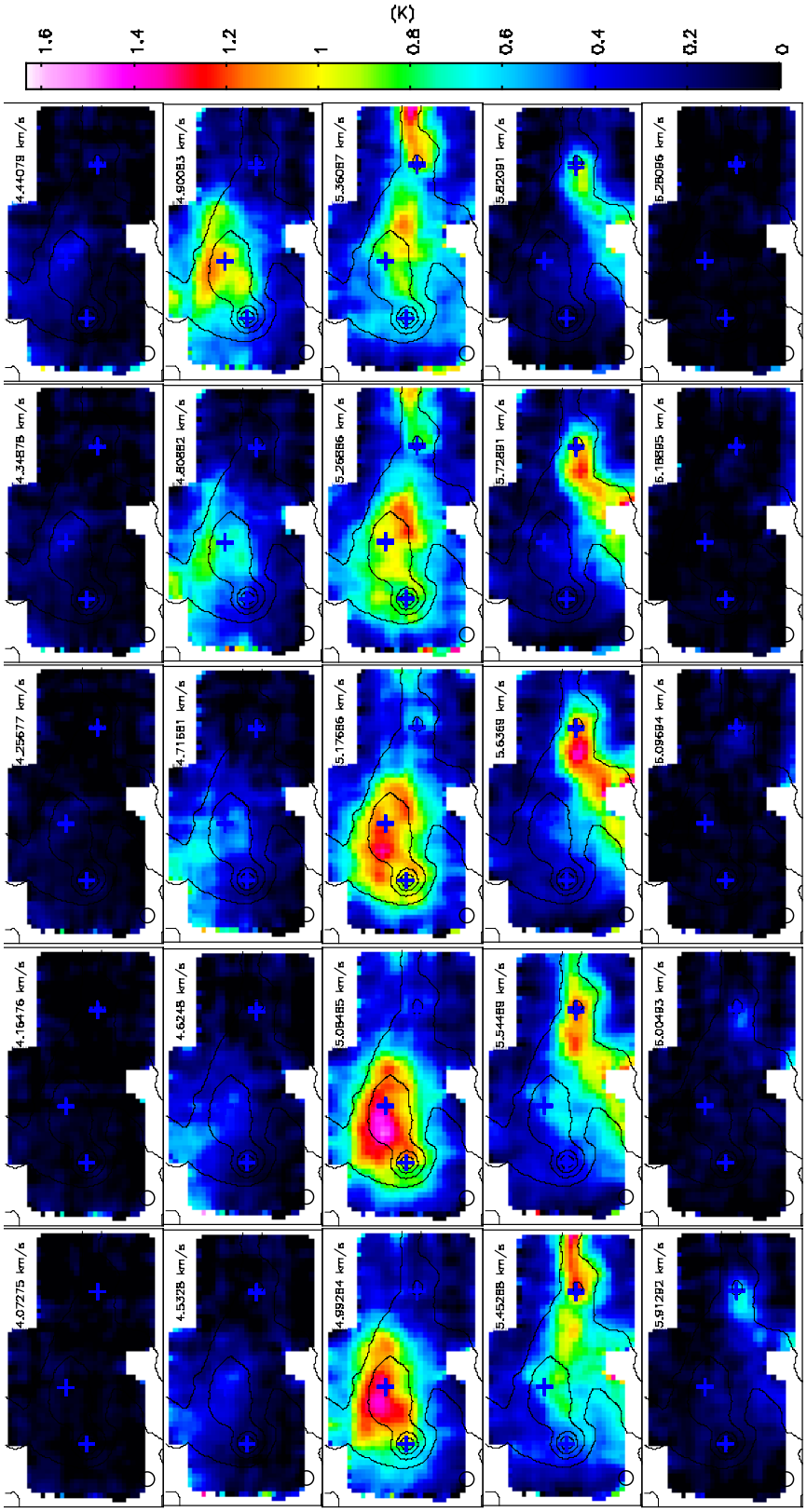

Figure C.9: Channel map of $C^{18}O$(J=1–0) in Lup1 C1, C3, and C4

Channel map of N_2H^+(J=1–0) in Lup1 C1, C3, and C4

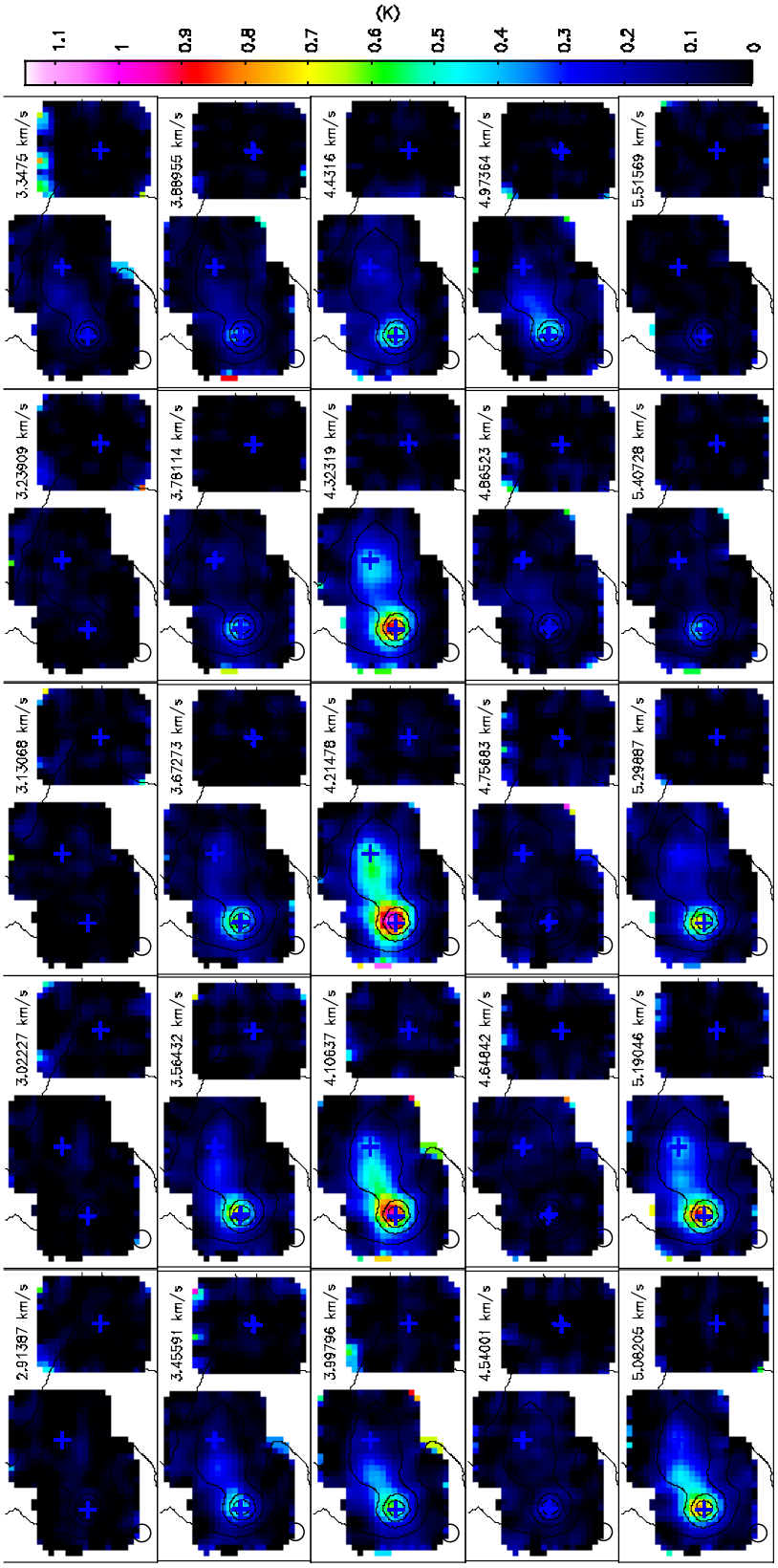

Figure C.10: Channel map of N_2H^+(J=1–0) in Lup1 C1, C3, and C4

Channel map of HC_3N(J=10–9) in Lup1 C1, C3, and C4

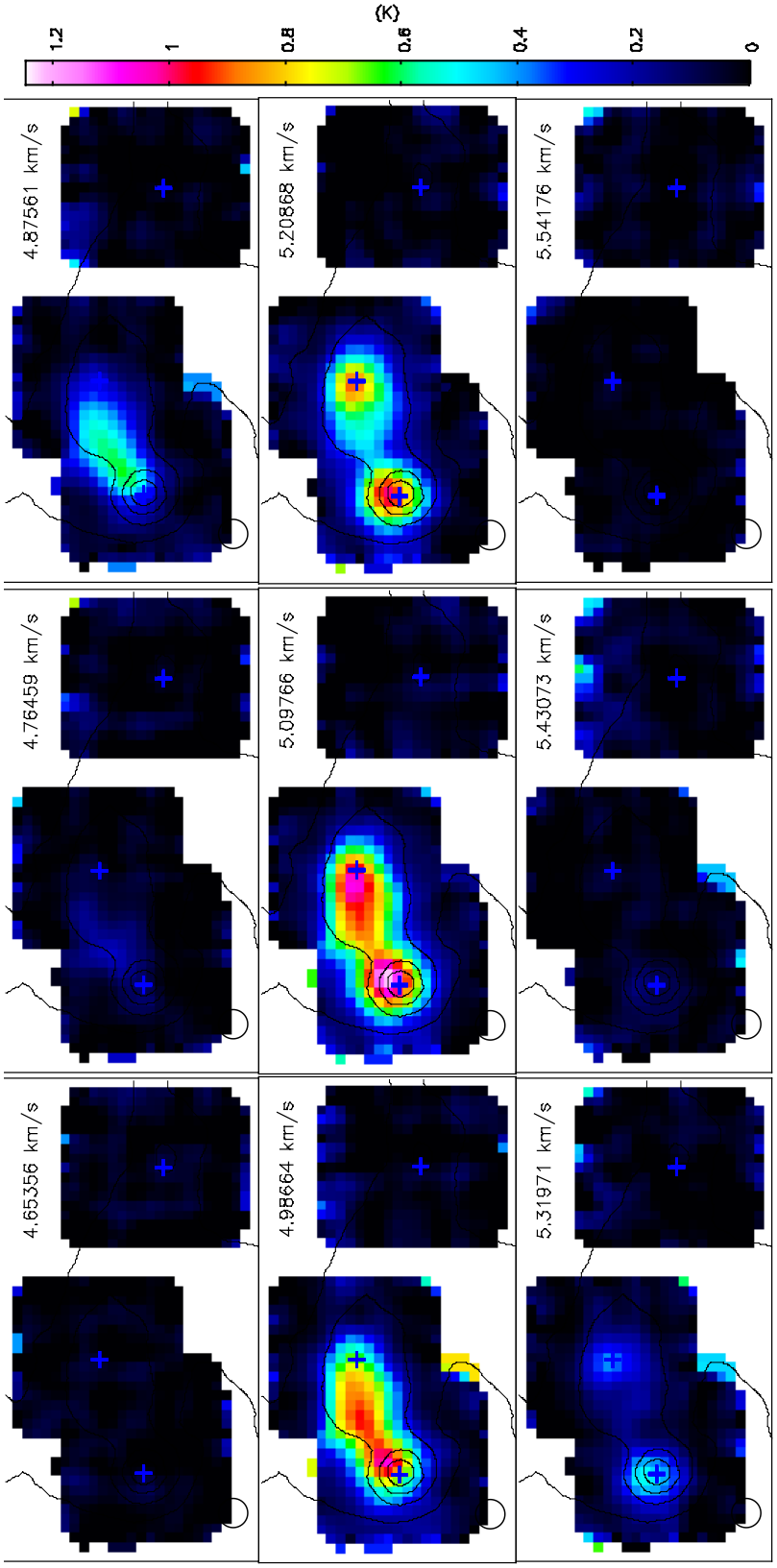

Figure C.11: Channel map of HC_3N(J=10–9) in Lup1 C1, C3, and C4

Channel map of $C^{18}O$(J=1–0) in Lup1 C2

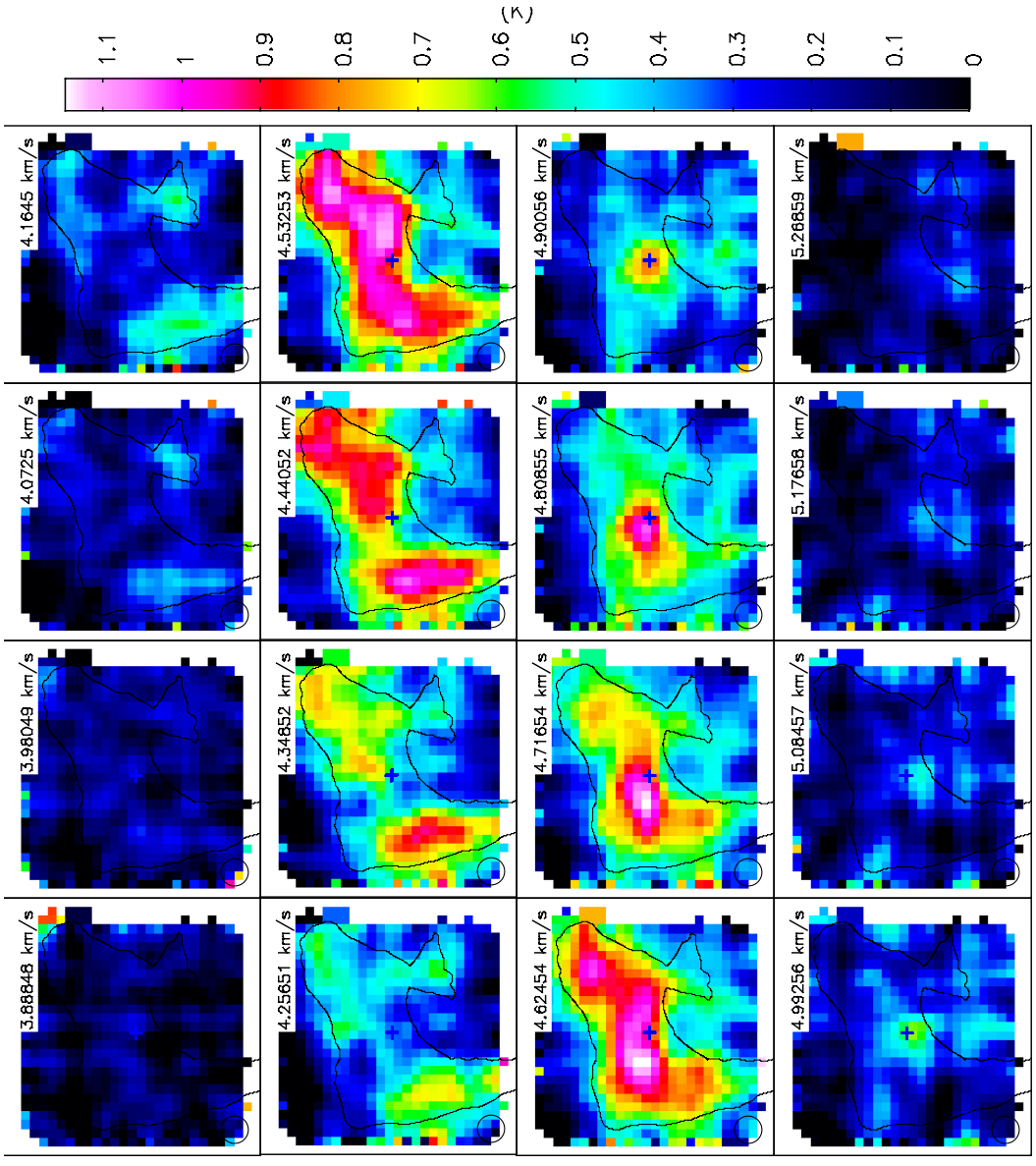

Figure C.12: Channel map of $C^{18}O$(J=1–0) in Lup1 C2

Channel map of $C^{18}O$(J=1–0) in Lup1 C5, C6, C7, and C8

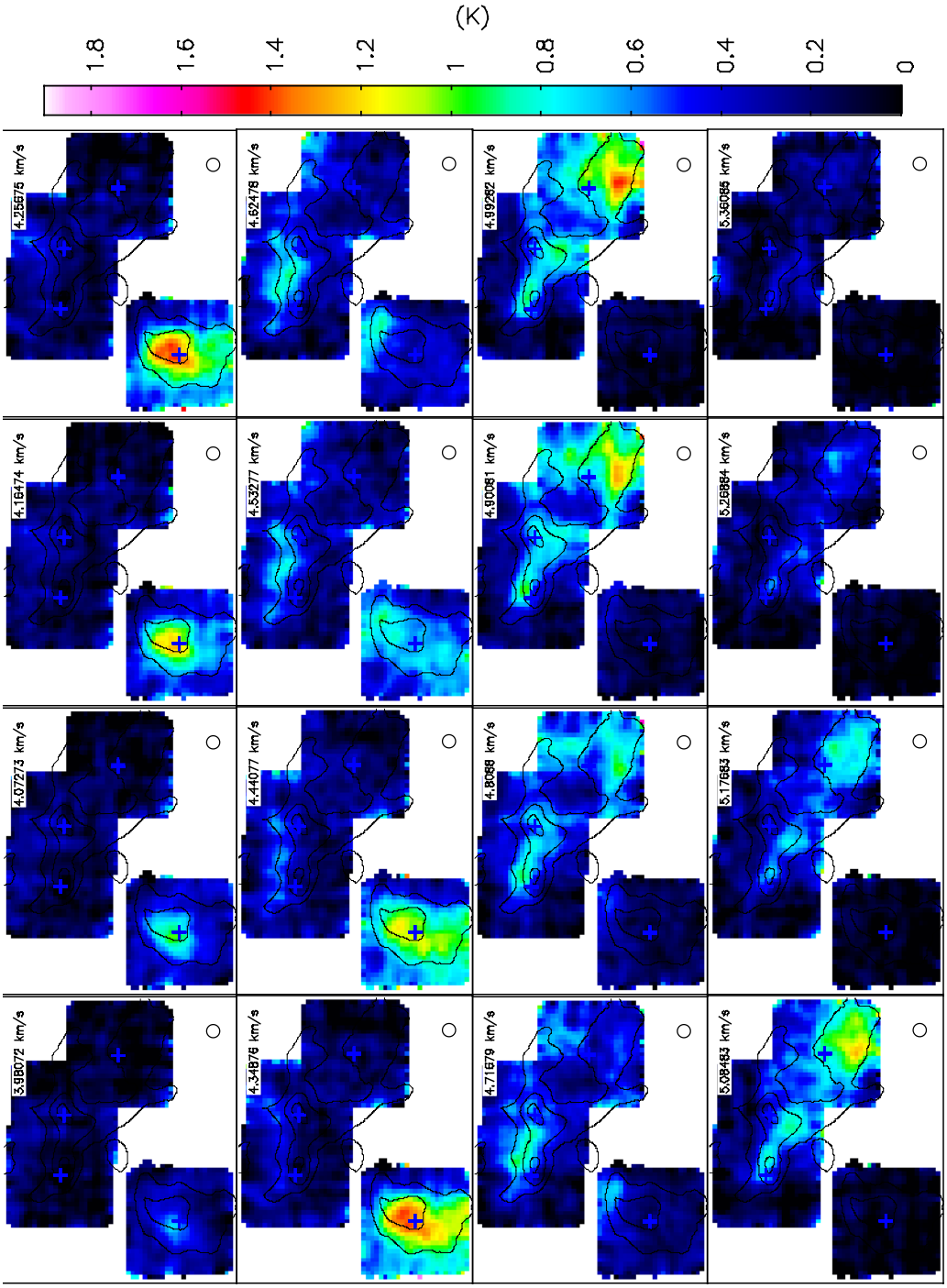

Figure C.13: Channel map of $C^{18}O$(J=1–0) in Lup1 C5, C6, C7, and C8

Channel map of N_2H^+(J=1–0) in Lup1 C5, C6, and C7

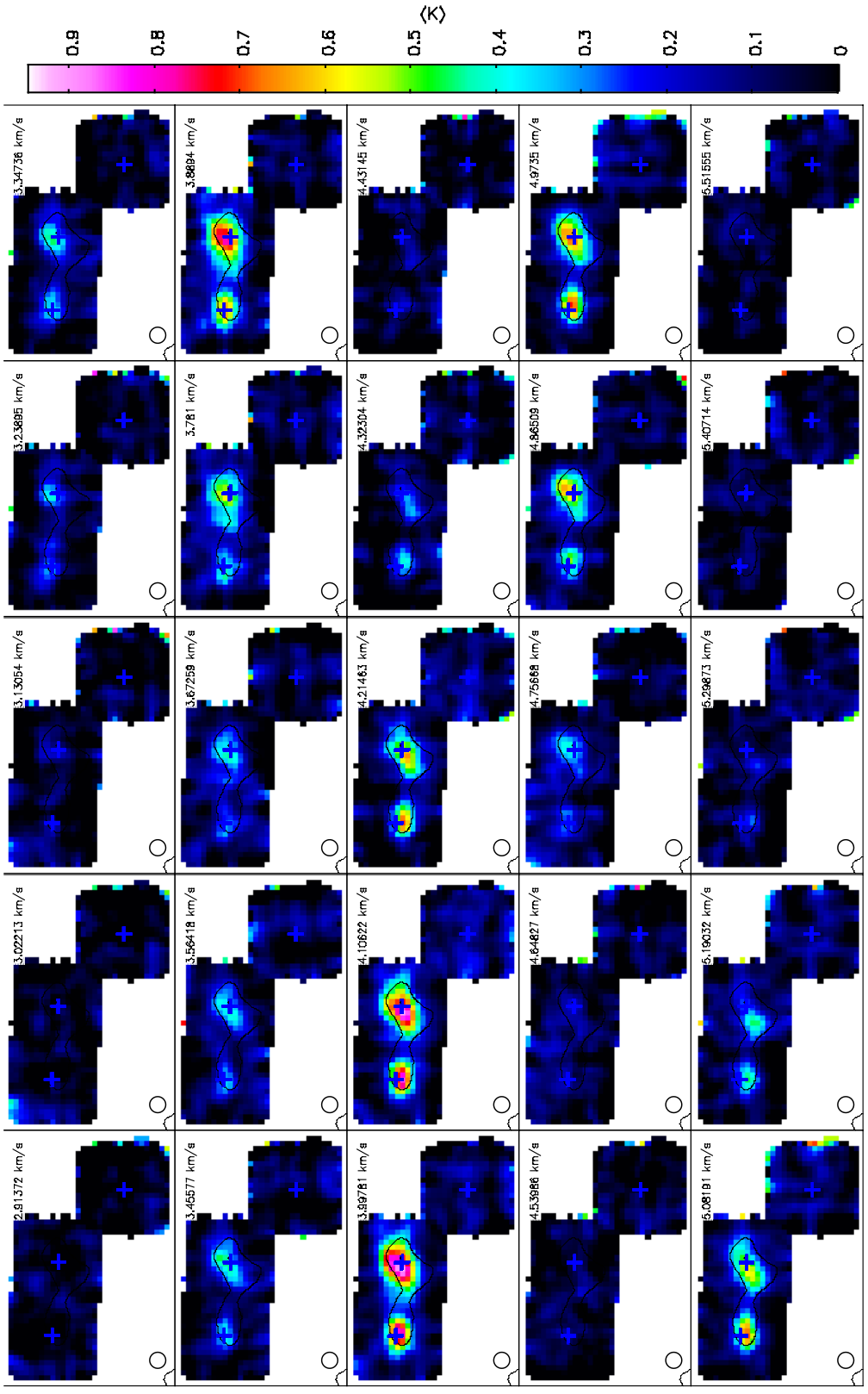

Figure C.14: Channel map of N_2H^+(J=1–0) in Lup1 C5, C6, and C7

Channel map of $HC_3N(J$=10–9) in Lup1 C5, C6, and C7

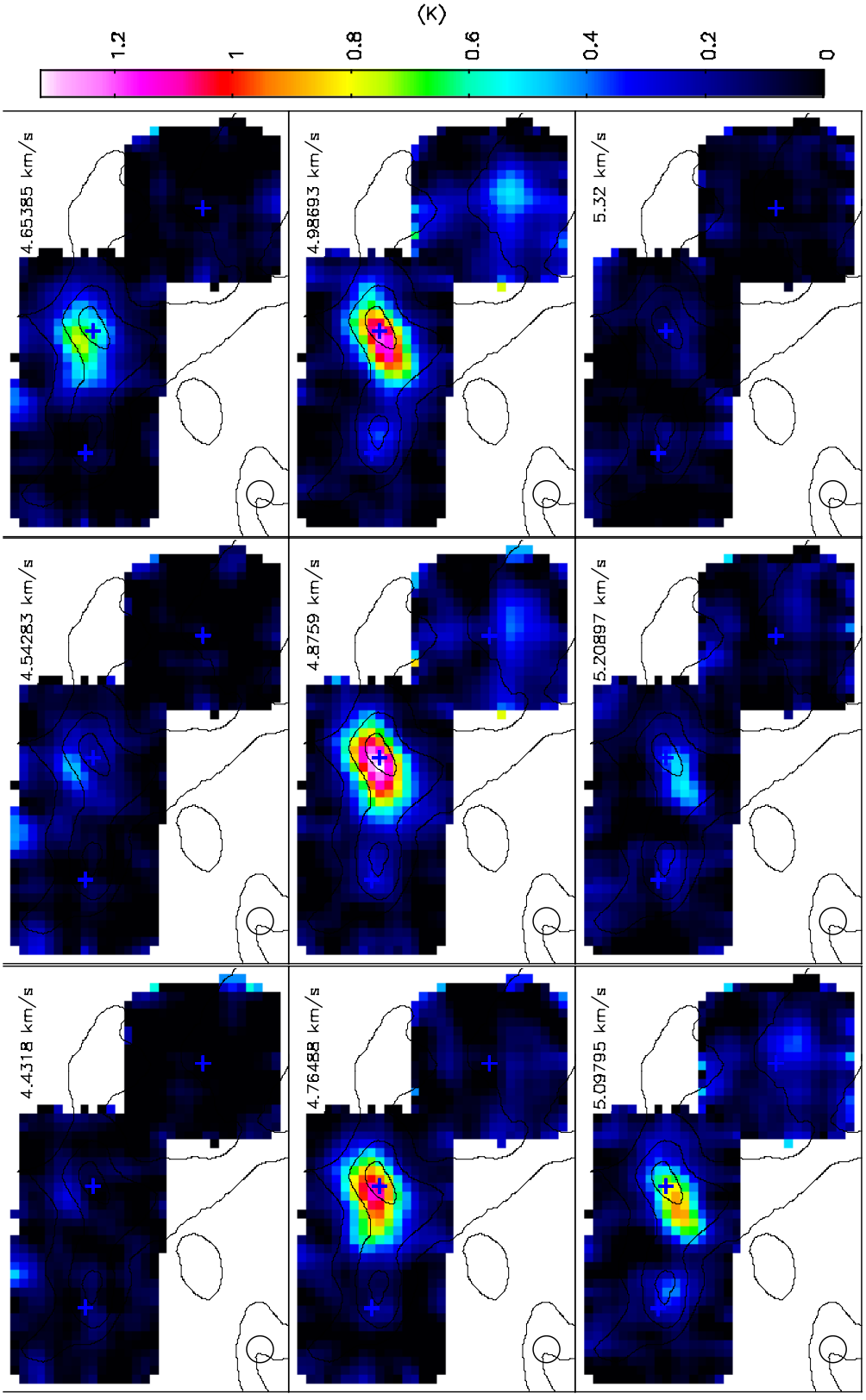

Figure C.15: Channel map of $HC_3N(J$=10–9) in Lup1 C5, C6, and C7

Channel map of $C^{18}O$(J=1–0) in Lup3 C1, C2, C3, C4, and C5

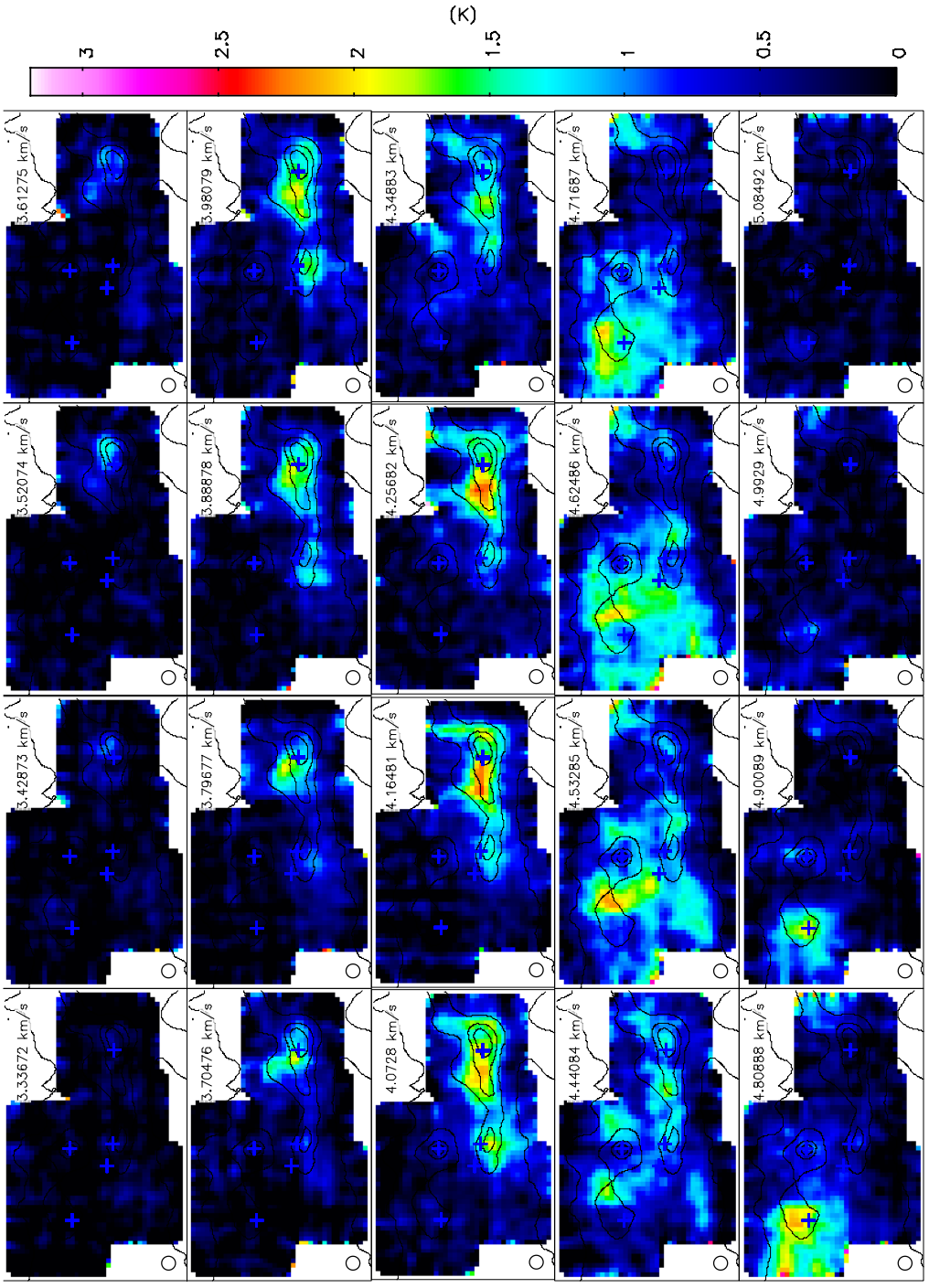

Figure C.16: Channel map of $C^{18}O$(J=1–0) in Lup3 C1, C2, C3, C4, and C5

Channel map of $N_2H^+(J$=1–0) in Lup3 C1, C2, C3, C4, and C5

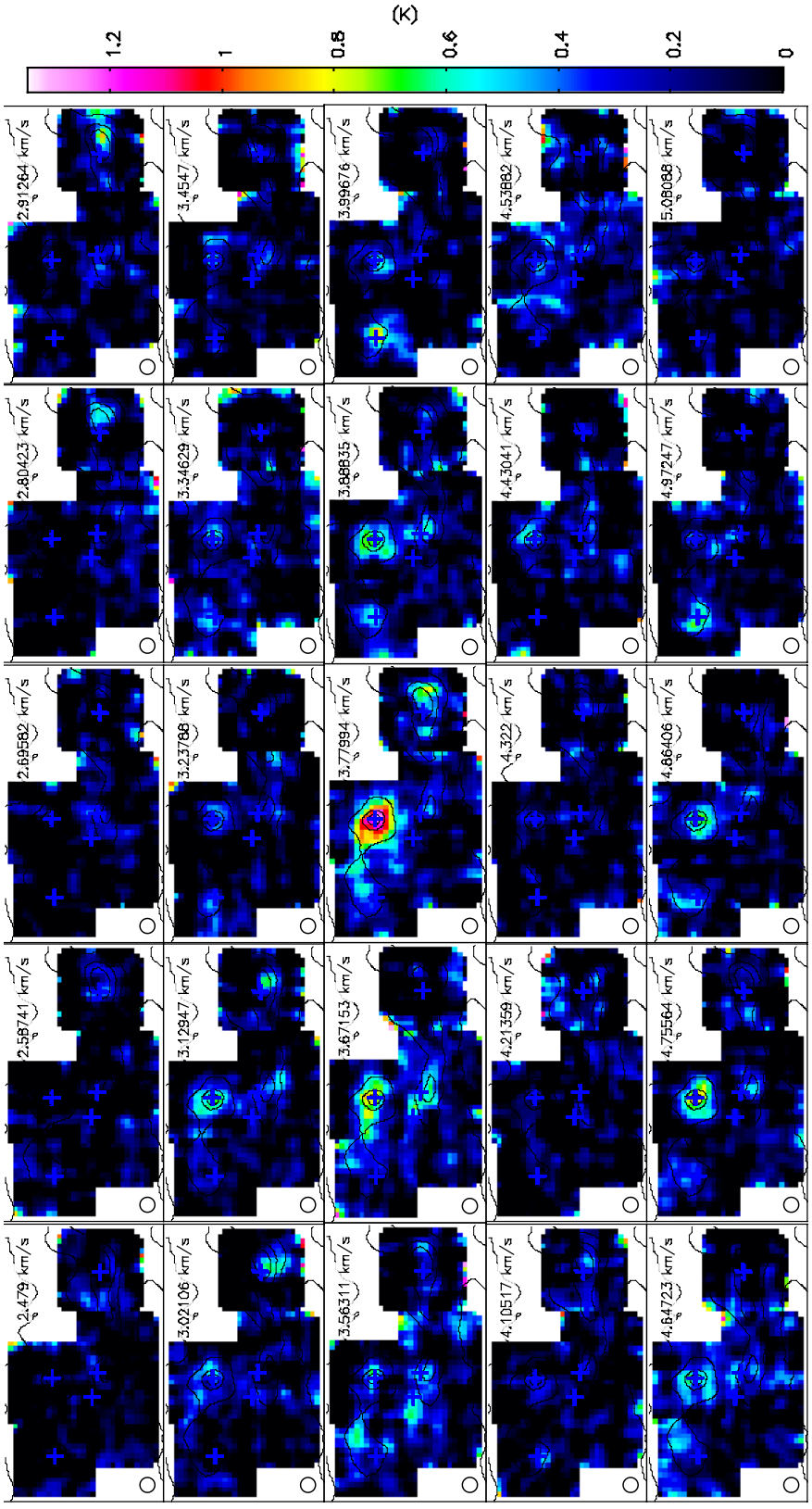

Figure C.17: Channel map of $N_2H^+(J$=1–0) in Lup3 C1, C2, C3, C4, and C5

Channel map of HC_3N(J=10–9) in Lup3 C1, C2, C3, C4, and C5

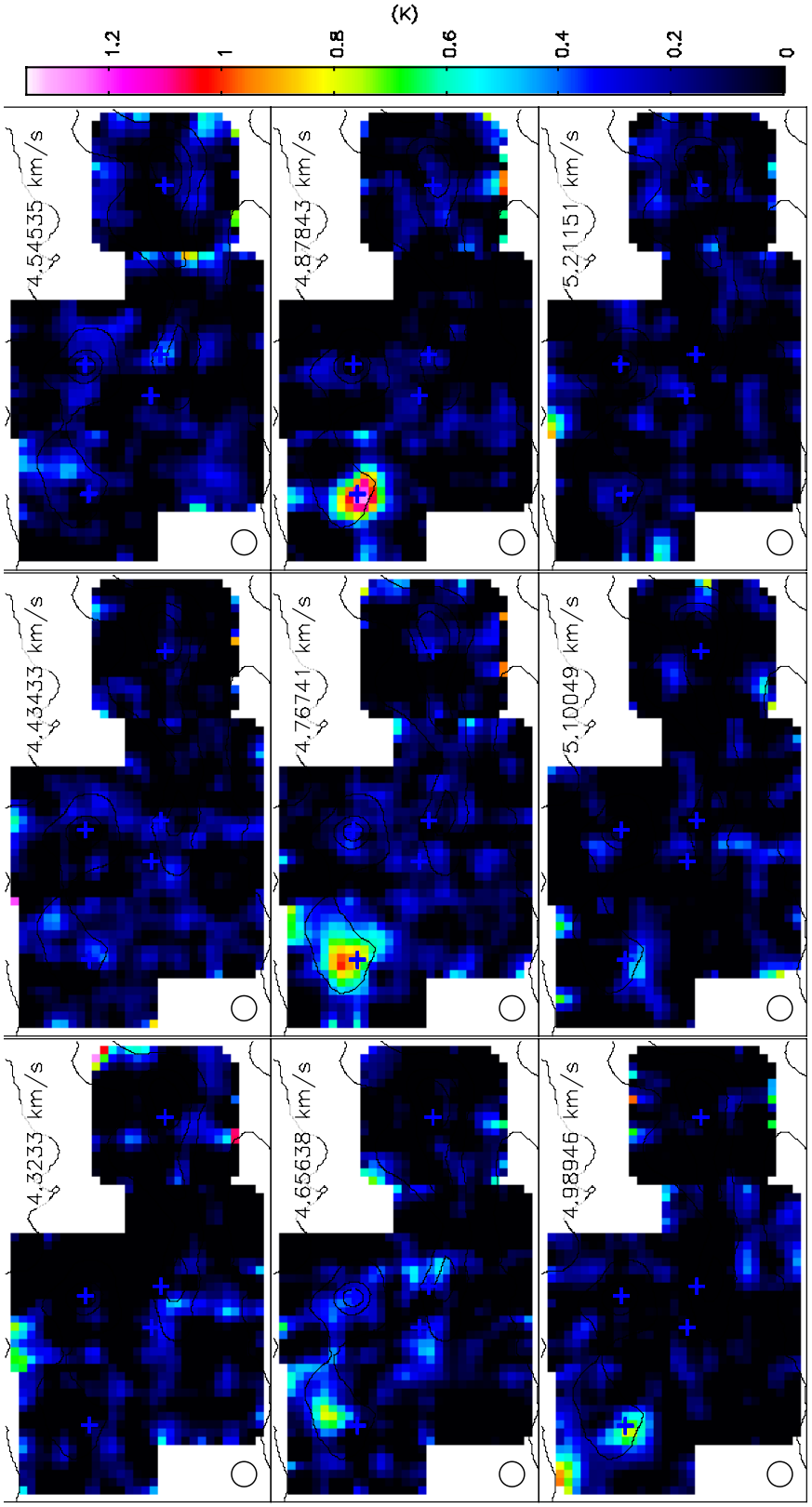

Figure C.18: Channel map of HC_3N(J=10–9) in Lup3 C1, C2, C3, C4, and C5

Bibliography

André, P., Di Francesco, J., Ward-Thompson, D., et al. 2014, Protostars and Planets VI, 27

André, P., Motte, F., & Neri, R. 2000, in Astronomical Society of the Pacific Conference Series, Vol. 217, Imaging at Radio through Submillimeter Wavelengths, ed. J. G. Mangum & S. J. E. Radford, 152

Andre, P., Ward-Thompson, D., & Barsony, M. 1993, ApJ, 406, 122

André, P., Men'shchikov, A., Bontemps, S., et al. 2010, A&A, 518, L102

Barranco, J. A., & Goodman, A. A. 1998, ApJ, 504, 207

Belloche, A. 2013, in EAS Publications Series, Vol. 62, EAS Publications Series, ed. P. Hennebelle & C. Charbonnel, 25–66

Belloche, A., & André, P. 2004, A&A, 419, L35

Belloche, A., André, P., Despois, D., & Blinder, S. 2002, A&A, 393, 927

Benedettini, M., Pezzuto, S., Burton, M. G., et al. 2012, MNRAS, 419, 238

Bontemps, S., Andre, P., Terebey, S., & Cabrit, S. 1996, A&A, 311, 858

Caselli, P., Benson, P. J., Myers, P. C., & Tafalla, M. 2002a, ApJ, 572, 238

Caselli, P., Walmsley, C. M., Zucconi, A., et al. 2002b, ApJ, 565, 344

Chen, X., Launhardt, R., & Henning, T. 2007, ApJ, 669, 1058

Comerón, F. 2008, The Lupus Clouds, ed. B. Reipurth, 295

Dunham, M. M., Arce, H. G., Mardones, D., et al. 2014, ApJ, 783, 29

Elias, J. H. 1978, ApJ, 224, 857

Emerson, D. T., & Graeve, R. 1988, A&A, 190, 353

Ford, A. B., & Shirley, Y. L. 2011, ApJ, 728, 144

Frerking, M. A., Langer, W. D., & Wilson, R. W. 1982, ApJ, 262, 590

Fuller, G. A., & Ladd, E. F. 2002, ApJ, 573, 699

Furuya, R. S., Kitamura, Y., & Shinnaga, H. 2006, ApJ, 653, 1369

—. 2014, ApJ, 793, 94

Goldsmith, P. F., Heyer, M., Narayanan, G., et al. 2008, ApJ, 680, 428

Goodman, A. A., Barranco, J. A., Wilner, D. J., & Heyer, M. H. 1998, ApJ, 504, 223

Goodman, A. A., Benson, P. J., Fuller, G. A., & Myers, P. C. 1993, ApJ, 406, 528

Hacar, A., & Tafalla, M. 2011, A&A, 533, A34

Hacar, A., Tafalla, M., Kauffmann, J., & Kovács, A. 2013, A&A, 554, A55

Hara, A., Tachihara, K., Mizuno, A., et al. 1999, PASJ, 51, 895

Hayashi, M., Hasegawa, T., Ohashi, N., & Sunada, K. 1994, ApJ, 426, 234

Hogerheijde, M. R., van Dishoeck, E. F., Blake, G. A., & van Langevelde, H. J. 1998, ApJ, 502, 315

Hughes, J., Hartigan, P., & Clampitt, L. 1993, AJ, 105, 571

Kirk, H., Myers, P. C., Bourke, T. L., et al. 2013, ApJ, 766, 115

Kurono, Y., Saito, M., Kamazaki, T., Morita, K.-I., & Kawabe, R. 2013, ApJ, 765, 85

Lada, C. J. 1987, in IAU Symposium, Vol. 115, Star Forming Regions, ed. M. Peimbert & J. Jugaku, 1–17

Larson, R. B. 1985, MNRAS, 214, 379

Loinard, L., Torres, R. M., Mioduszewski, A. J., et al. 2007, ApJ, 671, 546

Mangum, J. G., & Shirley, Y. L. 2015, PASP, 127, 266

Matsumoto, T., & Tomisaka, K. 2004, ApJ, 616, 266

Matthews, T. G., Ade, P. A. R., Angilè, F. E., et al. 2014, ApJ, 784, 116

Mizuno, A., Onishi, T., Hayashi, M., et al. 1994, Nature, 368, 719

Myers, P. C., Linke, R. A., & Benson, P. J. 1983, ApJ, 264, 517

Nakajima, T., Sakai, T., Asayama, S., et al. 2008, PASJ, 60, 435

Nakano, T., Hasegawa, T., & Norman, C. 1995, ApJ, 450, 183

Narayanan, G., Heyer, M. H., Brunt, C., et al. 2008, ApJS, 177, 341

Narayanan, G., Snell, R., & Bemis, A. 2012, MNRAS, 425, 2641

Ohashi, N., Hayashi, M., Ho, P. T. P., & Momose, M. 1997a, ApJ, 475, 211

Ohashi, N., Hayashi, M., Ho, P. T. P., et al. 1997b, ApJ, 488, 317

Ohashi, N., Saigo, K., Aso, Y., et al. 2014, ApJ, 796, 131

Onishi, T., Mizuno, A., Kawamura, A., Ogawa, H., & Fukui, Y. 1996, ApJ, 465, 815

—. 1998, ApJ, 502, 296

Onishi, T., Mizuno, A., Kawamura, A., Tachihara, K., & Fukui, Y. 2002, ApJ, 575, 950

Oya, Y., Sakai, N., Lefloch, B., et al. 2015, ApJ, 812, 59

Palmeirim, P., André, P., Kirk, J., et al. 2013, A&A, 550, A38

Panopoulou, G. V., Tassis, K., Goldsmith, P. F., & Heyer, M. H. 2014, MNRAS, 444, 2507

Poidevin, F., Ade, P. A. R., Angile, F. E., et al. 2014, ApJ, 791, 43

Rygl, K. L. J., Brunthaler, A., Sanna, A., et al. 2012, A&A, 539, A79

Saito, M., Kawabe, R., Kitamura, Y., & Sunada, K. 2001, ApJ, 547, 840

Saito, M., Sunada, K., Kawabe, R., Kitamura, Y., & Hirano, N. 1999, ApJ, 518, 334

Sanhueza, P., Jackson, J. M., Foster, J. B., et al. 2012, ApJ, 756, 60

Santiago-García, J., Tafalla, M., Johnstone, D., & Bachiller, R. 2009, A&A, 495, 169

Sawada, T., Ikeda, N., Sunada, K., et al. 2008, PASJ, 60, 445

Shirley, Y. L., Evans, II, N. J., Rawlings, J. M. C., & Gregersen, E. M. 2000, ApJS, 131, 249

Shu, F. H., Adams, F. C., & Lizano, S. 1987, ARA&A, 25, 23

Tachihara, K., Dobashi, K., Mizuno, A., Ogawa, H., & Fukui, Y. 1996, PASJ, 48, 489

Tachihara, K., Mizuno, A., & Fukui, Y. 2000, ApJ, 528, 817

Tachihara, K., Toyoda, S., Onishi, T., et al. 2001, PASJ, 53, 1081

Tachihara, K., Rengel, M., Nakajima, Y., et al. 2007, ApJ, 659, 1382

Tafalla, M., Santiago, J., Johnstone, D., & Bachiller, R. 2004, A&A, 423, L21

Tamura, M., Ohashi, N., Hirano, N., Itoh, Y., & Moriarty-Schieven, G. H. 1996, AJ, 112, 2076

Tatematsu, K., Umemoto, T., Kandori, R., & Sekimoto, Y. 2004, ApJ, 606, 333

Teixeira, P. S., McCoey, C., Fich, M., & Lada, C. J. 2008, Mon. Not. R. Astron. Soc., 384, 71

Terebey, S., Shu, F. H., & Cassen, P. 1984, ApJ, 286, 529

Tiné, S., Roueff, E., Falgarone, E., Gerin, M., & Pineau des Forêts, G. 2000, A&A, 356, 1039

Tobin, J. J., Hartmann, L., Calvet, N., & D'Alessio, P. 2008, ApJ, 679, 1364

Tobin, J. J., Hartmann, L., Chiang, H.-F., et al. 2012, Nature, 492, 83

Tobin, J. J., Hartmann, L., & Loinard, L. 2010, ApJ, 722, L12

Tobin, J. J., Hartmann, L., Chiang, H.-F., et al. 2011, ApJ, 740, 45

Yen, H.-W., Takakuwa, S., Ohashi, N., & Ho, P. T. P. 2013, ApJ, 772, 22

Acknowledgments

I would like to express my thanks to all persons who support and encourage me to research. I am deeply grateful to Norikazu Mizuno, my supervisor in doctor's course, for providing an opportunity of studying astronomy. I especially would like to express my deepest appreciation to Masao Saito for a lot of discussion and comments in my study. I am also grateful to Sachiko Okumura and Hiroshi Shibai, my supervisor in master's course and bachelor's course, respectively, for guiding me to the astronomical research field. I am deeply grateful to Koh-Ichiro Morita who gave me knowledge about a radio interferometric system when I was a master's course student. That knowledge and experience studied with him are still invaluable and base of my thinking way of research. I am thankful to Kazuya Saigo, Shigehisa Takakuwa, and Yasutaka Kurono for valuable discussion and comments on my study. I wish to express my warm thanks for constructive comments and discussion on my study to Ryohei Kawabe, Munetake Momose, Fumitaka Nakamura, Takashi Tsukagoshi, and Yoshito Shimajiri. I would like to thank Chang Won Lee. I carried out some observations with him and had interesting experiences and discussion. The wonderful academic experiences in the international collaboration with SOLA research consortium have hugely developed myself. I am thankful to SOLA members, in particular, Kengo Tachihara, Satoko Takahashi, Javier Radón, Paulo Cortes, Eiji Akiyama, Aya Higuchi, and Itziar de Gregorio-Monsalvo. I am very grateful to all ALMA-J and NRO staffs, especially Ken Tatematsu, Satoru Iguchi, Masaaki Hiramatsu, and Misato Fukagawa for continuing interest and encouragements. Finally, I want to thank my family, ALMA-J graduate students, my classmates and friends for encouraging me.